Gelation Landscape Engineering using a Multi-Reaction Supramolecular Hydrogelator System

Jamie S. Foster,[a] Justyna M. Żurek,[a] Nuno M. S. Almeida,[a] Wouter E. Hendriksen,[b] Vincent A. A. le Sage,[b] Vasudevan Lakshminarayanan,[b] Amber L. Thompson[c] Rahul Banerjee,[d] Rienk Eelkema,[b] Helen Mulvana,[e] Martin J. Paterson,[a] Jan H. van Esch[b] and Gareth O. Lloyd*[a]

[a] J. S. Foster, Dr. J. M. Żurek, N. M. S. Almeida, Prof. M. J. Paterson and Dr. G. O. Lloyd; Institute of Chemical Sciences, School of Engineering and Physical Sciences, Heriot-Watt University William Perkin Building, Edinburgh, Scotland, United Kingdom, EH14 4AS E-mail:g.o.lloyd@hw.ac.uk

[b] W. E. Hendriksen, V. le Sage, V. Lakshminarayanan, dr. R.Eelkema, Prof. dr. J. H. van Esch; Advanced Soft Matter Group, Department of Chemical Engineering, Delft University of Technology, Julianalaan 136, 2628 BL, Delft, the Netherlands

[c] Chemical Crystallography, Oxford University, Chemistry Research Laboratory, 12 Mansfield Road, Oxford, United Kingdom, OX1 3TA

[d] Dr. R. Banerjee; Polymers and Advanced Materials Laboratory, National Chemical Laboratory, Dr. Homi Bhabha Road, Pune 411008, India

[e] Dr. H. Mulvana; School of Engineering, James Watt South Building, University of Glasgow, Glasgow, Scotland, United Kingdom, G12 8QQ

Table of Contents

1.0 Technical details

1.1 Chemical list:

Chemicals were purchased from the following chemical companies and used without further purification:

Trifluoroacetic acid - Fluorochem

Hexamethylenetetramine – Alfa Aesar

Phloroglucinol – Aldrich

Isonicotinc acid hydrazide (***II***) – Alfa Aesar

Glucono delta-lactone (**GdL**) – Alfa Aesar

All solvents – Fisher

1.2 Powder X-Ray Diffraction:

PXRD patterns were collected at room temperature using a Bruker D8 Advance powder diffractometer in reflectance mode. Lynxeye super speed detector was used with the radiation being monochromated Cu Kα1, with a characteristic wavelength of 1.541 Å. 30 minute scans over the range $5° \leq 2\theta \leq 60°$ (stepsize = 0.014481°/counting time = 0.5 s/steps).

1.3 NMR:

NMR spectra were recorded on a Bruker AV 400 operating at 400.1 MHz for ^{1}H and 100.6 MHz for ^{13}C experiments. All spectra were recorded using 10 -15 mg of sample in 0.6 ml of solvent. Spectra recorded in D_2O also feature the addition of NaOH (approximately 5 mg) to dissolve the sample unless otherwise stated.

1.4 TEM:

TEM images were produced using a JEOL JEM-1400 microscope with an acceleration voltage of 120 kV. The samples were prepared on a copper grid with carbon film and dried for 24 hours before imaging. The images were produced using the Gatan Micrograph software.

1.5 SEM:

SEM images were produced using a Philips XL30 LaB6 ESEM equipped with an Oxford Instrument X-max 80 EDX detector.

1.6 IR:

IR spectra were recorded on a Nicolet is5 instrument using 24 scans at a resolution of 1 cm^{-1} and data spacing of 0.964 cm^{-1}.

1.7 Rheology:

Rheological experiments were performed on a Bohlin nano II rheometer. A 40 mm aluminium cone at 4^o was used with an operating gap of 300 μm gap and a solvent trap. For all gels 5 ml of the solution was prepared and added to the plate with a syringe in the operating gap so the gel could form in contact with the cone.

1.7.1 Time sweep experiments were commenced immediately upon addition of the solutions. All samples were recorded over 15 h at 20 ^{o}C with a torque of 100 μNm and a frequency of 10 Hz, data was taken every 30 s for a sample time of 3 s.

1.7.2 Frequency sweep experiments were performed immediately after the time sweep at 20 ^{o}C. The torque was kept constant at 100 μNm.

1.7.3 Stress sweep experiments were recorded after frequency sweep experiments. All samples were recorded at 20 ^{o}C and at a frequency of 1 Hz.

1.8 pH meter:

The pH meter used was a Mettler Toledo FiveEasy, a two point calibration was performed each morning.

1.9 Mass Spectrometery:

Mass spectrometry data were recorded using electrospray ionization (ESI) in negative mode using a Bruker micrOTOF instrument. High resolution mass spectrometry was used to confirm purity of the compounds produced as elemental analysis would not produce the expect results due to the poor combustion properties of these molecules. This is something that is confirmed in the literature with similar series of compounds.[1]

2.0 Synthetic Details

2.1 Synthesis of 1,3,5-triformylphoroglucinol (***I**_e*):

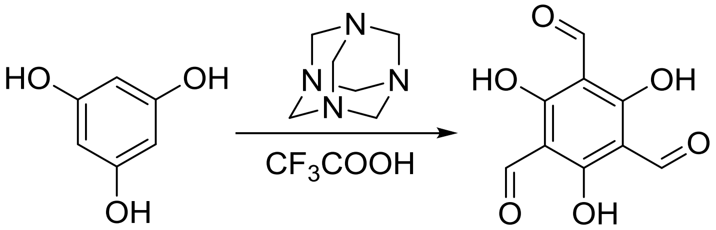

Figure S1. Reaction overview for the synthesis of 1,3,5-triformylphloroglucinol ($\boldsymbol{I_e}$) using hexamethylenetetramine.

To a mixture of hexamethylenetetramine (22.2 g, 157.5 mmol, 2.2 equiv.) and phloroglucinol (9 g, 71.4 mmol, 1 equiv) trifluoroacetic acid (135 ml) was added, the solution was then heated to 100 ^{o}C and stirred under nitrogen for 2.5 h. To the reaction mixture 3 M HCl (300 ml) was slowly added with continued heating at 100 ^{o}C and stirred for 1 h. After being allowed to cool to room temperature the reaction mixture was filtered and the filtrate obtained was extracted with dichloromethane (5 × 100 ml) before being dried with $MgSO_4$. Once dry the dichloromethane was removed by rotary evaporation yielding an orange solid. This solid was washed with hot ethanol (3 × 100 ml) to yield a pale yellow free flowing powder. This powder was dried in the oven overnight to yield the final product $\boldsymbol{I_e}$. The synthesis is a scaled up version of the synthesis presented by Chong *et .al* [1a].

2.1.1 Yield: 19%, 2.96 g (210.14 gmol^{-1}).

2.1.2 ^{1}H NMR(d6-DMSO, J/Hz, δ/ppm): 14.15 (S, 3H, Ar-OH), 10.82 (s, 3H, CHO).

2.1.3 ^{13}C NMR ($CDCl_3$, δ/ppm): 189.07 (-CHO), 178.43 (C-OH), 105.23 (C-aldehyde).

2.1.4 Elemental analysis: Calculated %C = 51.44, %H = 2.88 Found %C = 51.17, %H = 2.92.

2.1.5 Melting point: 198-199 ^{o}C (literature mp: 198 – 200 ^{o}C).[1a]

3.0 Gel preparation method descriptions organised by type of gel produced:

3.2 Gel C_k preparation method 1:

A typical example of setting gel $\mathbf{C_k}$ by method 1 at 2 wt% is described. $\mathbf{\mathit{I_e}}$ (67.2 mg, 0.32 mmol) was mixed with water (5 ml) to create a suspension. To this suspension NaOH (10 mg, 0.26 mmol) was added and the solution was well shaken until $\mathbf{\mathit{I_e}}$ had completely dissolved creating a solution at approximately pH 8. To a separate portion of water (5 ml) ***II*** (131.65 mg, 0.96 mmol) was added and then shaken until it had completely dissolved. These two solutions were then mixed together and shaken; the pH of the resulting solution was raised to between 9.5 and 12 with the addition of NaOH before being allowed to stand overnight producing a yellow gel. Gelation will occur over the optimum pH range 9.5-12.
Minimum gel concentration 0.5 wt%.

3.5 Gel C_e preparation method 2:

A typical example of setting gel $\mathbf{C_e}$ by method 2 at 1 wt% is described. $\mathbf{\mathit{I_e}}$ (33.6 mg, 0.16 mmol) was mixed with water (5 ml) to create a suspension. To this suspension NaOH (3 mg, 0.08 mmol) was added and the solution was well shaken until $\mathbf{\mathit{I_e}}$ had completely dissolved. To a separate portion of water (5 ml) ***II*** (65.83 mg, 0.48 mmol) was added and the mixture shaken until it had completely dissolved. These two solutions were then mixed together and shaken. This produced a dull yellow solution after 6 hours (ideally overnight to ensure complete formation of $\mathbf{C_e}$). To this solution **GdL** (42.76 mg, 0.24 mmol) was added and allowed to dissolve, this resulted in the formation of a red gel after 2 hours. Gelation will occur over the optimum pH range 4-5. Apparent pK_a is 6.8 (+/- 0.1).
Minimum gel concentration 0.2 wt%.

3.6 Gel B_e preparation method 3:

A typical example of setting gel $\mathbf{B_e}$ by method 3 at 1 wt% is described. $\mathbf{\mathit{I_e}}$ (33.6 mg, 0.16 mmol) was mixed with water (5 ml) to create a suspension. To this suspension NaOH (3 mg, 0.08 mmol) was added and the solution was well shaken until $\mathbf{\mathit{I_e}}$ had completely dissolved. To a separate portion of water (5 ml) ***II*** (43.89 mg, 0.32 mmol) was added and the mixture shaken until it had completely dissolved. These two solutions were then mixed together, shaken and immediately **GdL** (42.76 mg, 0.24 mmol) was added and allowed to dissolve, this resulted in the formation of an orange gel after 15 minutes. Gelation will occur over the optimum pH range 4-5. Apparent pK_a is 6.6 (+/- 0.1).
Minimum gel concentration 0.3 wt%.

N.B. The quantities of ***II*** quoted in the above methods used to prepare gels $\mathbf{C_k}$, $\mathbf{C_e}$ and $\mathbf{B_e}$ are guidelines only and the same gels can be obtained using any number of equivalents of ***II***. Variation in weight percentage of the formed gels is determined by the quantity of $\mathbf{\mathit{I_e}}$, or limiting reactant if ***II*** and the result 100% conversion to products (whatever the limiting reactant is).

All three gels, $\mathbf{C_e}$, $\mathbf{C_k}$ and $\mathbf{B_e}$, can be made by ex situ methods instead of the in situ methods described above. Details of experiments and their analyses can be found at the end of this document in section 14. In each case the corresponding isolated compounds, $\mathbf{C_e}$, $\mathbf{C_k}$ or $\mathbf{B_e}$, are dissolved at a pH of 8 and above. Subsequent gelation is accomplished by adjusting the pH to the setting value utilising **GdL** or base.

4.0 Rheology Results

4.1 Gel C_k method 1:

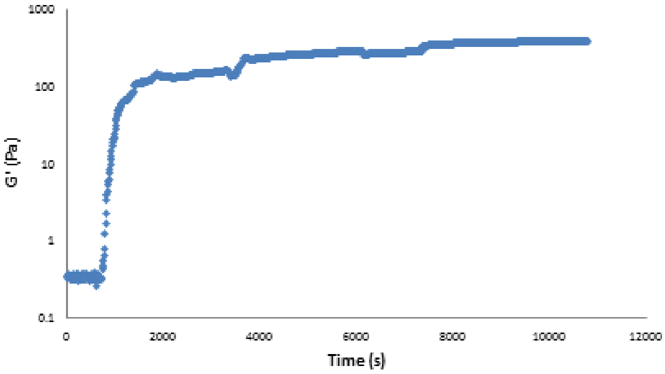

Figure S2. Time sweep rheometry of gel $\mathbf{C_k}$ prepared by method 1. Storage modulus *G'* (Pa) (y-axis) plotted (log scale) against time (s) (x-axis).

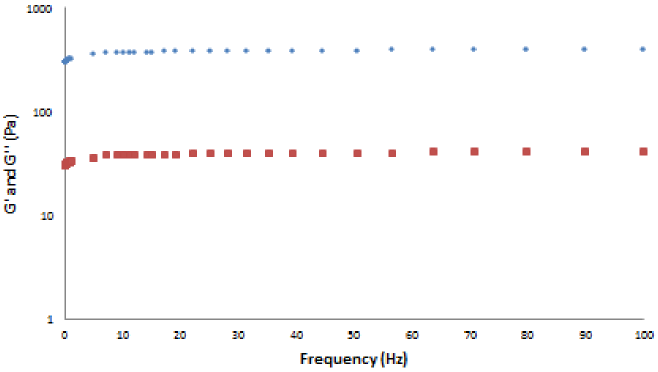

Figure S3. Frequency sweep rheometry of gel $\mathbf{C_k}$ prepared by method 1. The storage modulus *G'* (Pa) (blue) and the loss modulus *G"* (Pa) (red) are shown as a log scale (y-axis) against the frequency (Hz) (x-axis).

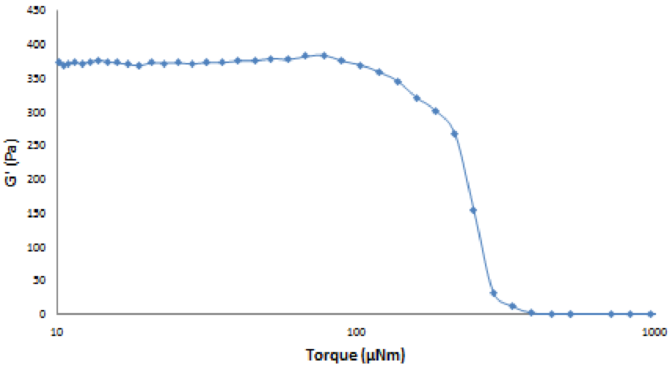

Figure S4. Amplitude sweep rheometry of gel $\mathbf{C_k}$ prepared by method 1. The storage modulus *G'* (Pa) (y-axis) plotted against torque (µNm) (x-axis) shown in a log scale. A line between data points added to guide the eye.

4.2 Gel C_e method 2:

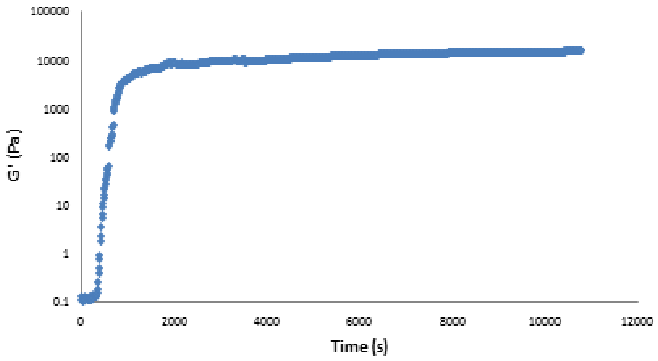

Figure S5. Time sweep rheometry of gel $\mathbf{C_e}$ prepared by method 2. Storage modulus *G'* (Pa) (y-axis) plotted (log scale) against time (s) (x-axis).

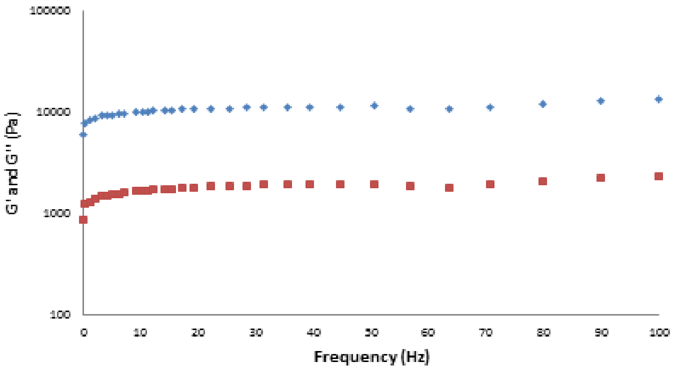

Figure S6. Frequency sweep rheometry of gel $\mathbf{C_e}$ prepared by method 2. The storage modulus *G'* (Pa) (blue) and the loss modulus *G"* (Pa) (red) are shown as a log scale (y-axis) against the frequency (Hz) (x-axis).

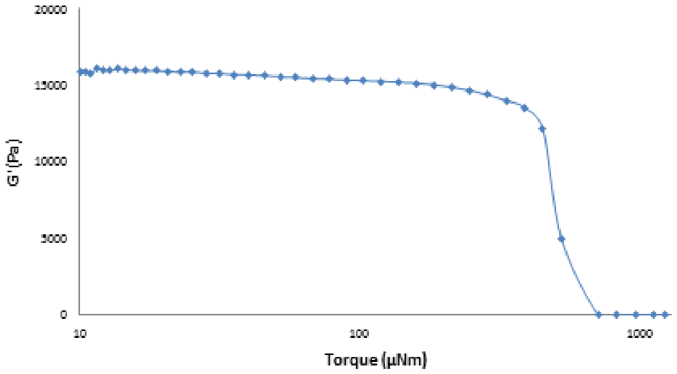

Figure S7. Amplitude sweep rheometry of gel $\mathbf{C_e}$ prepared by method 2. The storage modulus *G'* (Pa) (y-axis) plotted against torque (μNm) (x-axis) shown in a log scale. A line between data points added to guide the eye.

4.6 Gel B_e method 3:

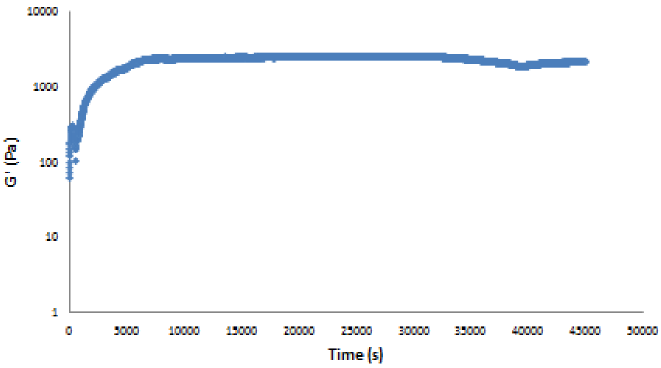

Figure S8. Time sweep rheometry of gel $\mathbf{B_e}$ prepared by method 3. Storage modulus *G'* (Pa) (y-axis) plotted (log scale) against time (s) (x-axis).

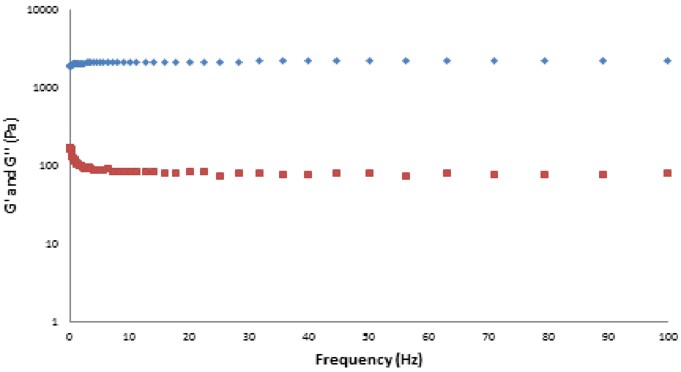

Figure S9. Frequency sweep rheometry of gel $\mathbf{B_e}$ prepared by method 3. The storage modulus *G'* (Pa) (blue) and the loss modulus *G''* (Pa) (red) are shown as a log scale (y-axis) against the frequency (Hz) (x-axis).

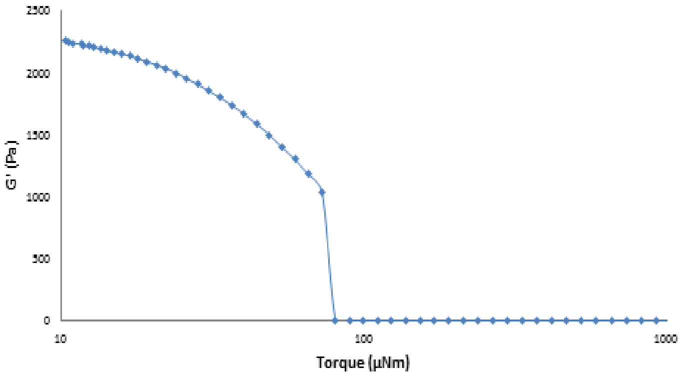

Figure S10. Amplitude sweep rheometry of gel $\mathbf{B_e}$ prepared by method 3. The storage modulus *G'* (Pa) (y-axis) plotted against torque (µNm) (x-axis) shown in a log scale. A line between data points added to guide the eye.

5.0 Gel fibre images

5.1 TEM images of gel C_k:

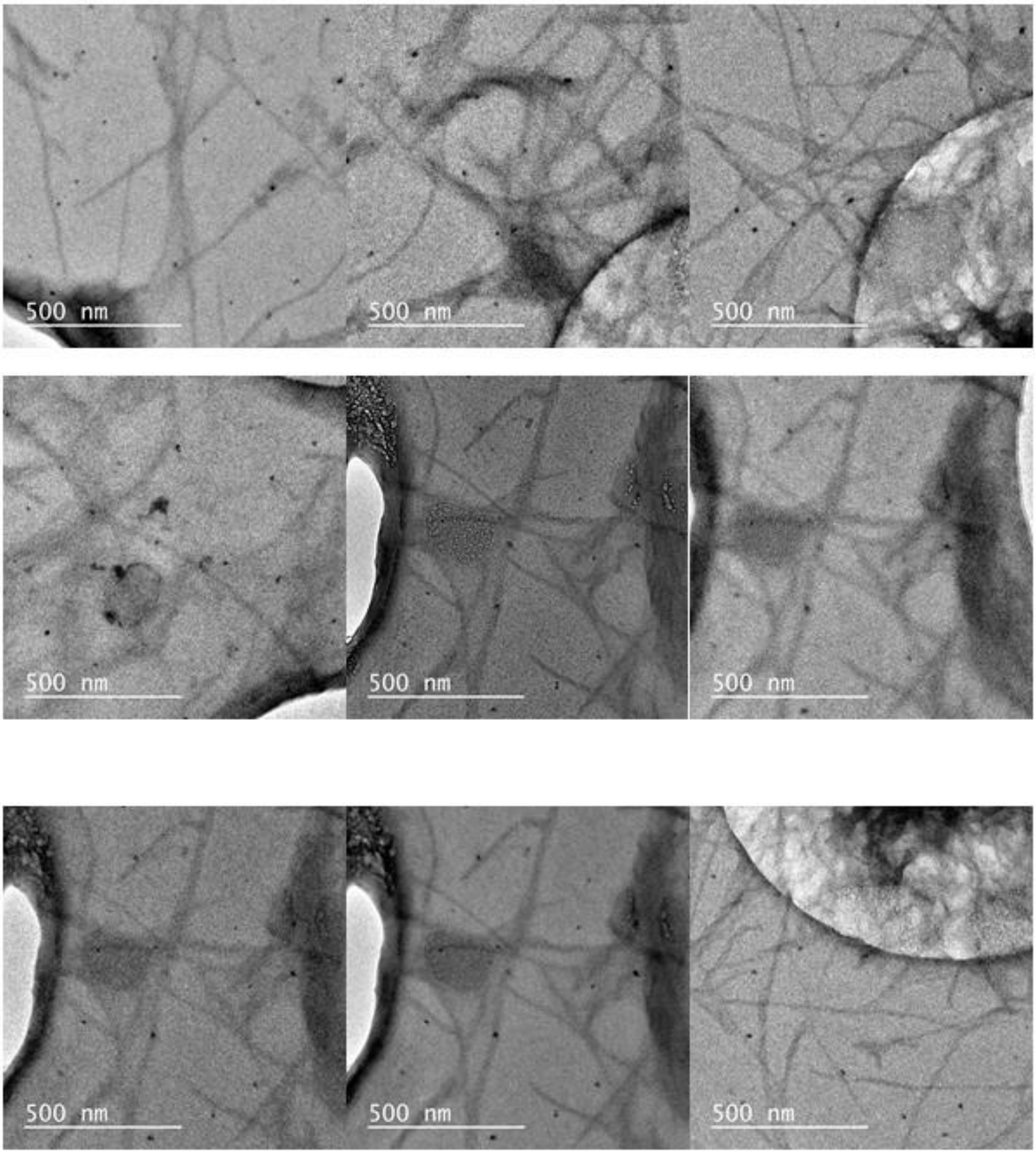

Figure S11. TEM images showing the fibrous nature of the gel $\mathbf{C_k}$ prepared by method 1.

5.2 SEM images of gel C_k:

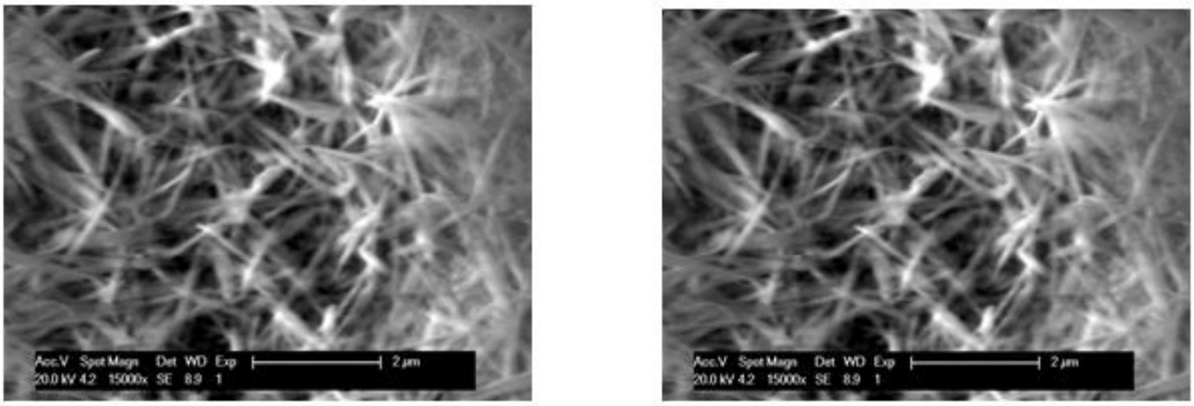

Figure S12. SEM images showing the fibrous nature of the gel $\mathbf{C_k}$ prepared by method 1.

5.3 TEM images of C_e gel:

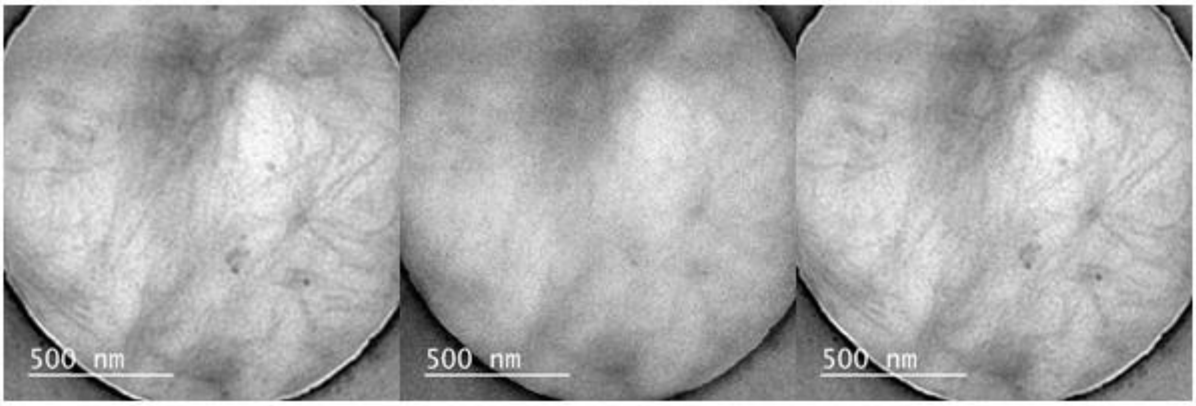

Figure S13. TEM images showing the fibrous nature of the gel $\mathbf{C_e}$ prepared by method 2.

5.4 SEM images of C_e gel:

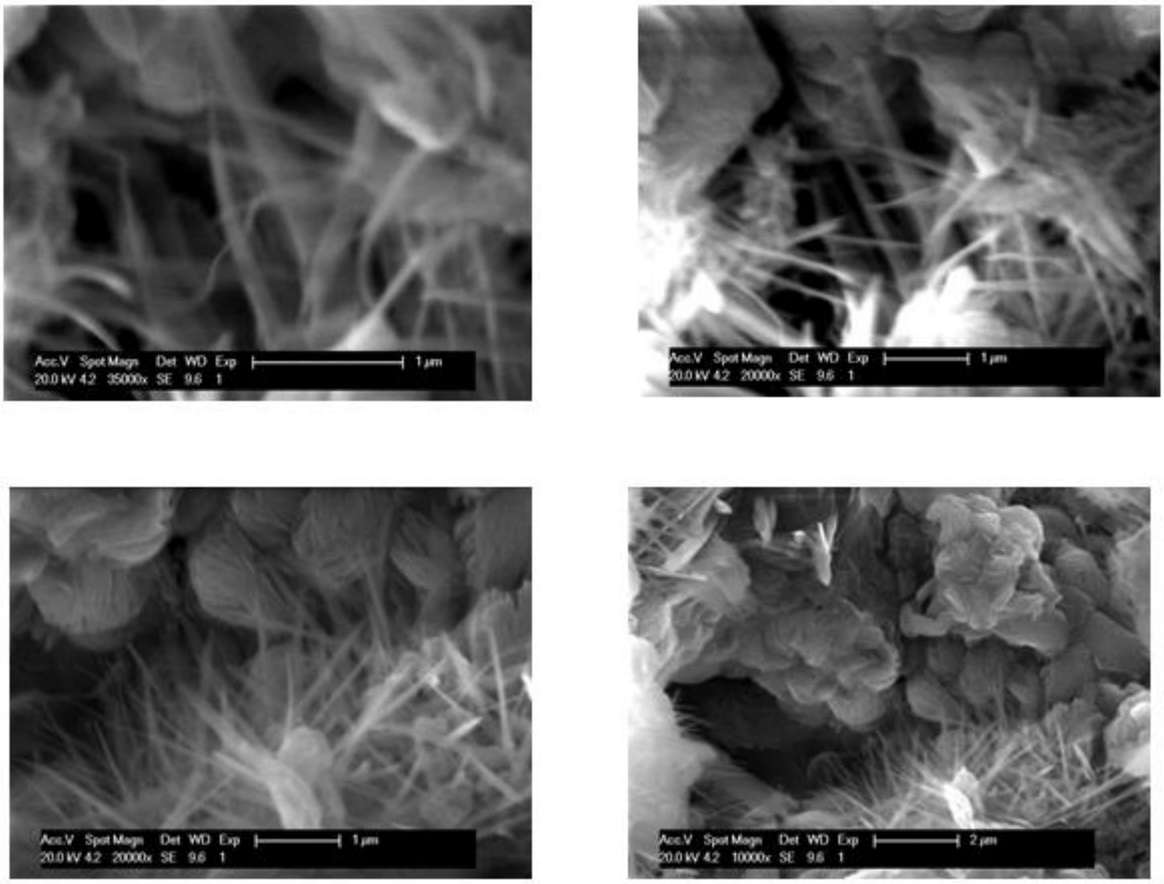

Figure S14. SEM images showing the fibrous nature of the gel $\mathbf{C_e}$ prepared by method 2, with crystallites that can be attributed to the gluconic acid and sodium salts.

5.5 SEM images of gel B_e:

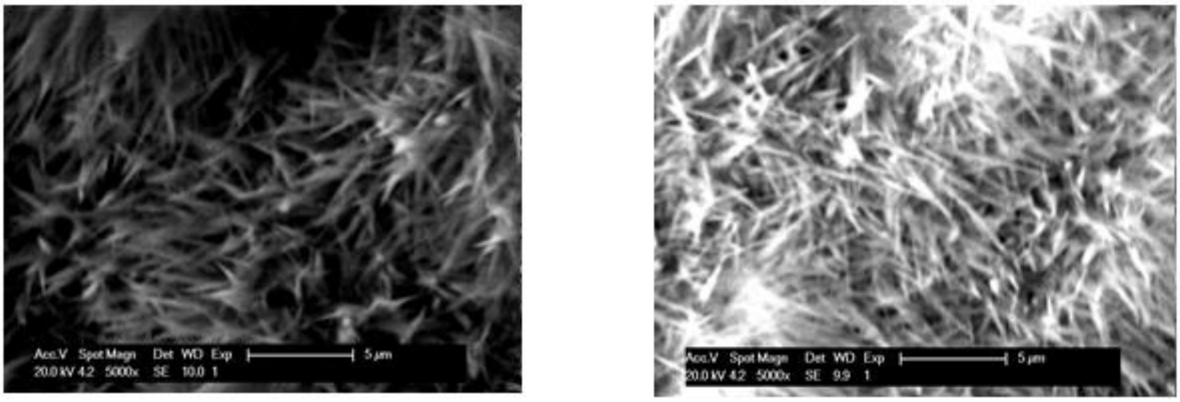

Figure S15. SEM images showing the fibrous nature of the gel $\mathbf{B_e}$ prepared by method 3.

6.0 Analysis of dried gels:

All gels prepared by all methods could be dried using vacuum filtration and thoroughly washed using water (10 x 100 ml) to ensure that all NaOH and gluconic acid from the gel setting process had been removed. The isolate was then dried in the oven at 80 °C overnight.

6.1 Analysis of dried gel C_k prepared by method 1:

6.1.1 ^1H NMR(d_6-DMSO, J/Hz, δ/ppm): 13.88 (dd, J = 12.99, 4.37, 3H, -CH-NH-NH-), 13.70 (t, J = 13.15, 3H, -CH-NH-NH-), 8.52 (s, 6H, Ar-H), 8.34 (dd, J = 13.00, 2.54, 3H, -CH-), 7.85 (m, 6H, Ar-H).

6.1.2 ^{13}C NMR (d_6-DMSO, δ/ppm): ^{13}C NMR (d_6-DMSO, δ/ppm): 183.43, 181.92, 181.92, 180.58 ((1)C=O); 162.52, 162.4, 162.35 ((2)C=O); 149.37 ((3) Ar-H); 147.21, 147.12 ((4) C=CH); 145.28, 144.79, 144.69, 144.2 ((5) =CH-NH-); 121.88 ((6) Ar-H); 102.52, 102.35, 102.33 ((7) Ar-CO-). For assignments see Fig. S31.

6.1.3 IR: 3167, 2162, 1622, 1587, 1505, 1440, 1376, 1276, 1148, 1058, 999, 879, 839, 750, 701, 685, 577.

6.1.4 Melting point**:** Decomposes upon heating (>300 °C).

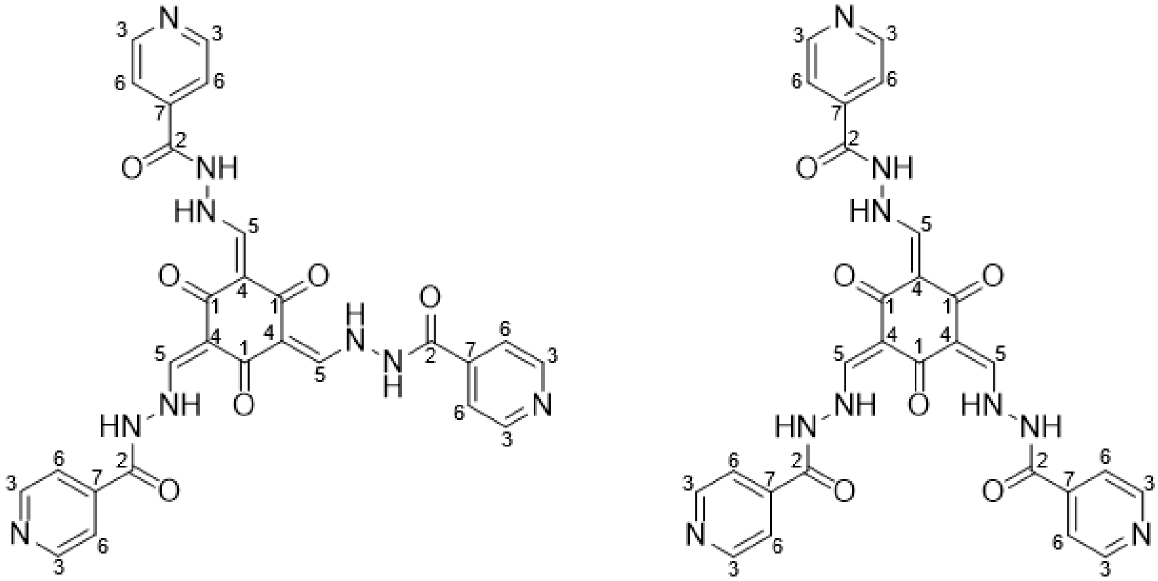

Figure S16. Chemical structure of dried product of gel **C_k** formed by method 1 (N'-[[2,4,6-trioxo-3,5-bis[[2-(pyridine-4-carbonyl)hydrazino]methylene]cyclohexylidene]methyl]pyridine-4-carbohydrazide) showing the two structural conformations it adopts C_3 (right) and C_s (left) with numerical labels relating the assignment of the ^{13}C NMR spectra.

6.2 Analysis of dried gel C_e prepared by method 2:

6.2.1 ^{1}H NMR (d$_6$-DMSO, J/Hz, δ/ppm): 13.83 (broad s, 3H, Ar-OH), 12.48 (broad s, 3H, -NH), 8.96 (s, 3H, -CHN), 8.81 (s, 6H, Ar-H), 7.86 (s, 6H, Ar-H)

6.2.2 ^{13}C NMR (d$_6$-DMSO, δ/ppm): 161.68 ((1) 3 × Ar-OH), 160.13 ((2) 3 × -NHCO-), 150.63 ((3) 6 × Ar-H), 146.32 ((4) 3 × -N=C-), 140.08 ((5) 3 × C, pyridyl), 121.37 ((6) 6 × Ar-H), 98.85 (3 × C, core)

6.2.3 IR: 2822, 1671, 1636, 1590, 1458, 1413, 1375, 1326, 1264, 1217, 1182, 1155, 1069, 989, 952, 898, 839, 788, 751, 551.

6.2.4 Melting point: Decomposes upon heating (> 300 ^{o}C)

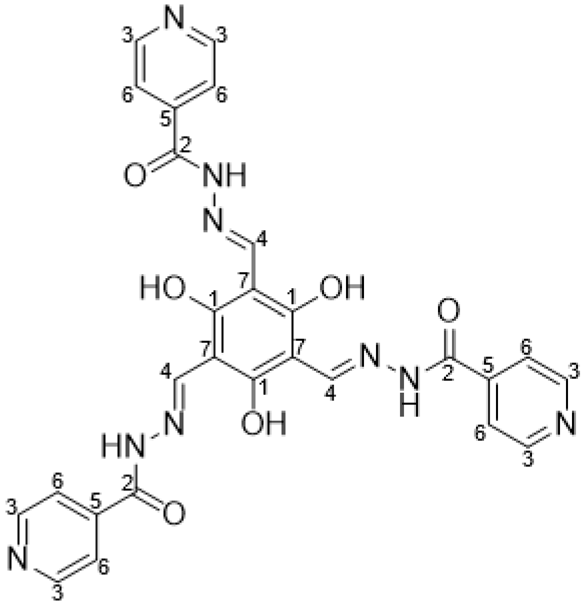

Figure S17. Chemical structure of dried product of gel $\mathbf{C_e}$ formed by method 2 (N-[(E)-[2,4,6-trihydroxy-3,5-bis[(E)-(pyridine-4-carbonylhydrazono)methyl]phenyl]methyleneamino]pyridine-4-carboxamide) with numerical labels relating the assignment of the ^{13}C NMR spectra.

6.3 Analysis of dried gel B_e prepared by method 3:

6.3.1 ^{1}H NMR (d$_6$-DMSO, J/Hz, δ/ppm): 13.75 (broad s, 3H, Ar-OH), 12.45 (broad s, 2H, -NH), 10.12 (s, 1H, -CHO), 8.85 (s, 2H, -CHN), 8.80 (d, 4H, Ar-H), 7.84 (d, 4H, Ar-H)

6.3.2 ^{13}C NMR (d$_6$-DMSO, δ/ppm): 192.25 ((1)-CHO), 167.77 ((2)Ar-OH), 166.80 ((3)2 × Ar-OH), 160.84 ((4) –NH-C=O), ((5) 150.66 (4 × Ar-H), 145.74 ((6) -N=C-), 139.65 ((7) C, pyridyl), 121.68 ((8)4 × Ar-H), 99.71 ((9) core C, imine) 99.05 ((10) core C, aldehyde)

6.3.3 IR: 3675, 2988, 2901, 1549, 1451, 1407, 1394, 1382, 1250, 1056, 1028, 892, 839, 748, 681, 597

6.3.4 HRMS (ESI$^-$) calculated for [M-H]$^-$ 447.1059, $C_{21}H_{15}N_6O_6$ found: 447.1079

6.3.5 Melting point: Decomposes upon heating (>300 ^{o}C)

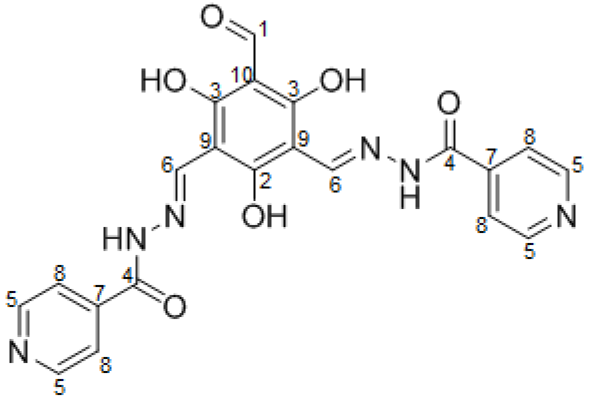

Figure S18. Chemical structure of dried product of gel **B$_e$** formed by method 3 (N-[(E)-[3-formyl-2,4,6-trihydroxy-5-[(E)-(pyridine-4-carbonylhydrazono)methyl]phenyl]methyleneamino]pyridine-4-carboxamide) with numerical labels relating the assignment of the ^{13}C NMR spectra.

7.0 Mass spectrometry analysis of the reaction kinetics:

7.1 Method description

HPLC-MS could be used to monitor the reaction progress. The MS abundance of each of the reaction products, i.e. mono-substituted (**A_e**), di-substituted (**B_e**) and tri-substituted species (**C_e** or **C_k**), was utilised to determine the relative product yield/concentration. All compounds were assumed to be equally capable of flight and ionisation in the MS experiments and in detection (no variance was noted in experiments). Concentrations were estimated by utilising peak abundance of detected compounds with the summation of all observations equal to the concentration of the initial limiting reagent, which in this case is ***I_e***. The calculated concentrations are then normalised to show percentage conversion across a number of different reaction conditions and experimental protocols (e.g. for easy comparison with UV-Vis experiments). Calibration curves were not utilised in the MS data. Experimentally the MS data matched exactly the results obtained from other analytical techniques without the need for calibration curves. The HPLC tuning and separation was inconsistent due to the long retention times and an inability to quench the reaction. Therefore direct injection was utilised.

MS data showing transition of products over time for the 1.5% 'gel or solution' (0.07804 M) prepared with 6 equivalents of ***II*** relative to ***I_e***. 1.5 % solutions were prepared at pH 8 and pH 6. MS data was collecting by sampling the solutions by taking 20 µL of gel into 1mL of MeOH resulting in full dissolution of unset gel (red) to clear solution (yellow). MS experiments were by direct injection using MeOH as carrier phase. Data was normalised in the following manner were ***I_e***, ***A_e***, ***B_e*** and ***C_e*** or ***C_k*** represent the raw abundancy data values and ***I_e'***, ***A_e'***, ***B_e'*** and ***C_e'*** or ***C_k'*** represent the normalised values (**C_X** = **C_e** or **C_k**):

$$\left(\frac{I_e}{I_e+A_e+B_e+C_x}\times 100 = I'_e\right)+\left(\frac{A_e}{I_e+A_e+B_e+C_x}\times 100 = A'_e\right)+\left(\frac{B_e}{I_e+A_e+B_e+C_x}\times 100 = B'_e\right)+\left(\frac{C_x}{I_e+A_e+B_e+C_x}\times 100 = C'_x\right) = I'_e + A'_e + B'_e + C'_x = 100\%$$

The conversion and therefore sum of the concentrations of **I_e**, **A_e**, **B**$_e$ and **C_e** or **C_k** should always add up to 100% as any increase or decrease in any species will correspond to an equivalent increase or decrease in other species. All systematic errors in the MS data do not appear to alter the interpretation of the experiments.

7.2 Raw pH 8 results table

Table S1 shows the MS abundance of products and reactants. Only the M-H anion peak is shown here, however, in the calculations M-2H anion peaks were also included as their relative abundance was high.

Table S1. MS abundance of products and reactants based on M-H anion peak abundance.

Time (minutes)	I_e	A_e	B_e	C_k
0	26.27	100	0	0
1	6.1	100	0	0
2	0.94	100	29.69	0
4	2.07	75.25	100	0.99
6	0	25.31	100	1.07
8	0	8.07	100	0.95
10	0	1.12	100	1.38
15	0	0	100	1.78
20	0	0	100	4.44
25	0	0	100	3.86
30	0	0	100	6.86
45	0	0	100	12.37
60	0	0	100	18.77
90	0	0	100	41.8
120	0	0	100	76.24
180	0	0	92.56	100
270	0	0	73.98	100
360	0	0	40.72	100
1200	0	0	10.99	100

7.3 pH 8 normalised results table

Table S2 shows the calculated percentage abundance. Calculation takes the assumption that all found species should result in a summed 100% concentration based on initial concentration of core of 0.07804 mM.

Table S2. Normalised MS abundance of products and reactants.

Time	I_e'	A_e'	B_e'	C_k'
0	20.8	79.2	0	0
1	5.7	94.3	0	0
2	0.72	76.6	22.7	0
4	1.1	42.2	56.1	0.6
6	0	20.0	79.1	0.9
8	0	7.4	91.7	0.9
10	0	1.1	97.6	1.3
15	0	0	98.3	1.7
20	0	0	95.7	4.3
25	0	0	96.3	3.7
30	0	0	93.6	6.4
45	0	0	89	11
60	0	0	84.2	15.8
90	0	0	70.5	29.5
120	0	0	56.7	43.3
180	0	0	48.1	51.9
360	0	0	28.9	71.1
1200	0	0	9.9	90.1

7.4 pH 8 plotted data

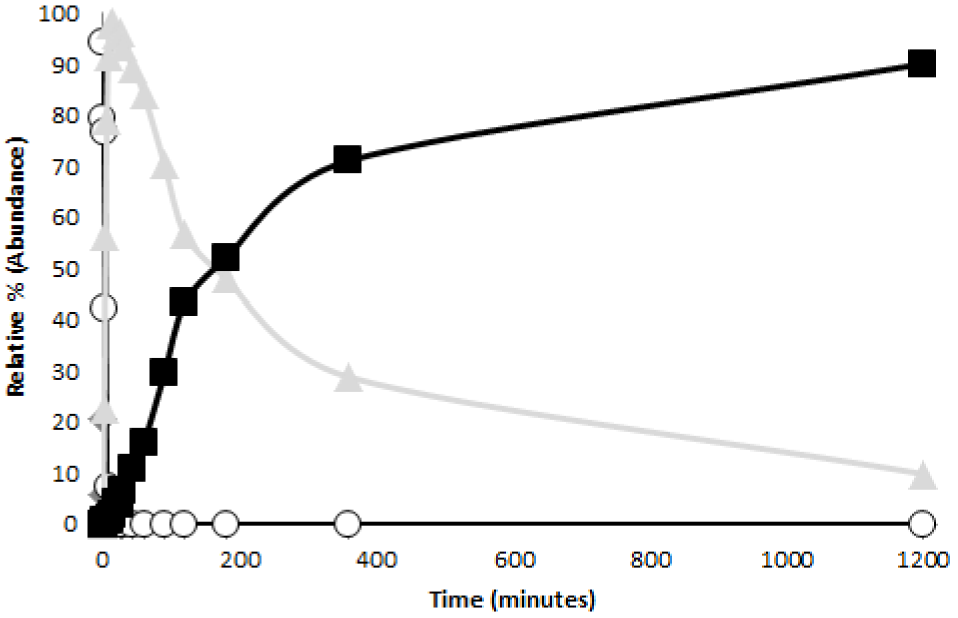

Figure S19. The kinetics diagram produced from the MS experiment conducted from a stock solution at pH 8. ***I_e*** (shown as **O**) and ***II*** (at a ratio of 1:6, respectively) to **C_k** (shown as ■) via intermediate **A_e** (shown as ◆, only two points at the bottom left of the graph) and **B_e** (shown as ▲).

7.5 Raw pH 6.5 results table

Table S3. MS abundance of products and reactants for M-H peak.

time	I_e	A_e	B_e	C_e
0	38.74	87.91	0	0
3	0	100	20.24	0
7	0	100	94.13	0
20	0	13.97	100	1.39
30	0	0	100	1.25
45	0	0	100	1.45
60	0	0	100	2.79
90	0	0	100	2.8
120	0	0	100	4.3
180	0	0	100	3.93
240	0	0	100	5.33
360	0	0	100	11.83
1440	0	0	59.76	100
5760	0	0	21.72	100

7.6 Normalised pH 6.5 results table

Table S4. Calculated percentage abundance. Calculation takes the assumption that all found species should result in a 100% concentration based on initial concentration of core of 0.07804 mM.

Table S4. Normalised MS abundance of products and reactants.

time	I_e'	A_e'	B_e'	C_e'
0	30.59	69.41	0	0
3	0	83.17	16.83	0
7	0	51.51	48.49	0
20	0	12.11	86.69	1.2
30	0	0	98.77	1.23
45	0	0	98.57	1.43
60	0	0	97.28	2.72
90	0	0	97.28	2.72
120	0	0	95.88	4.12
180	0	0	96.22	3.78
240	0	0	94.94	5.06
360	0	0	89.42	10.58
1440	0	0	37.41	62.59
5760	0	0	17.84	82.16

7.7 Plotted pH 6.5 data

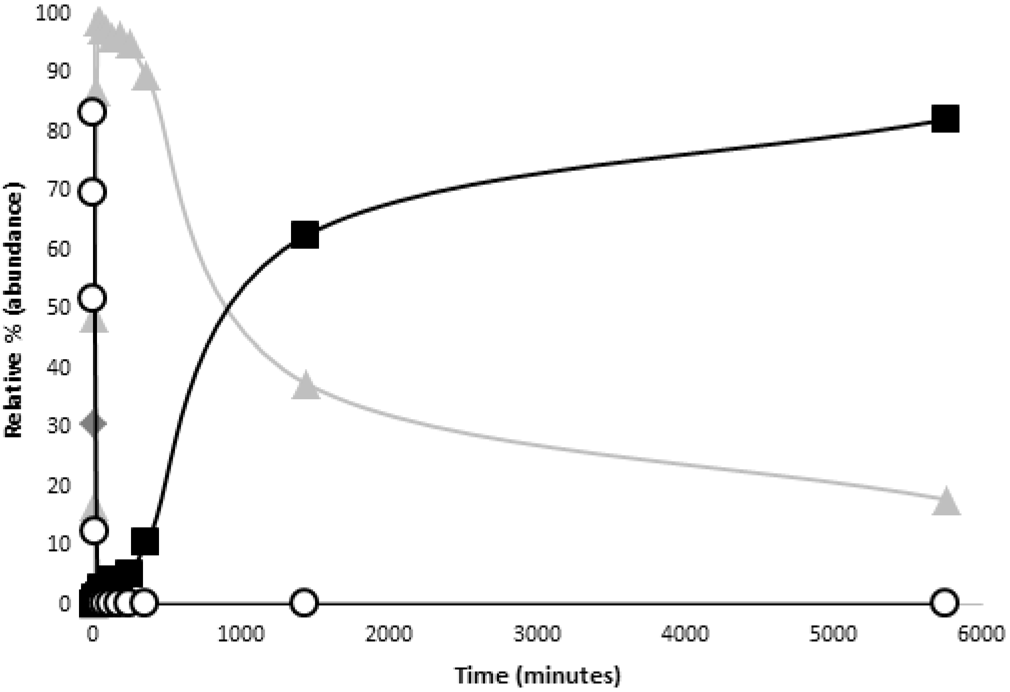

Figure S20. The kinetics diagram produced from the HPLC-MS experiment conducted from a stock solution at pH 6.5. ***I*$_e$** (shown as **O**) and ***II*** (at a ratio of 1:6, respectively) to **C$_e$** (shown as ■) via intermediate **A$_e$** (shown as ◆) and **B$_e$** (shown as ▲).

7.8 Presentation of some of the mass spectrometry results for reaction kinetics

The following MS data is presented to show the occurrence of the products and reactant in the ESI data which is collected in negative mode. The isoniazid did not show in negative mode but was always present in the positive mode. Data which was concurrently collect.

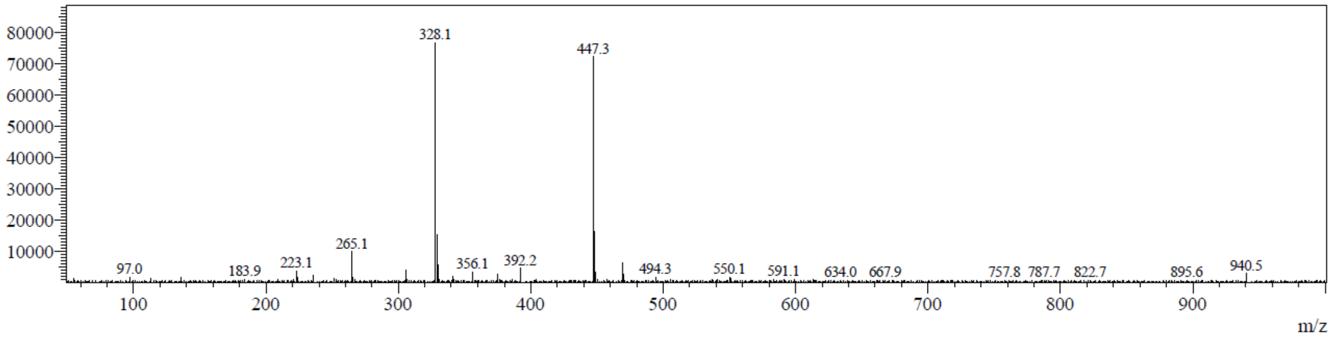

Figure S21. ESI-MS taken 1 minute after showing the presence of $\mathbf{A_e}$ at 328.1 m/z and $\mathbf{B_e}$ at 447.3 m/z.

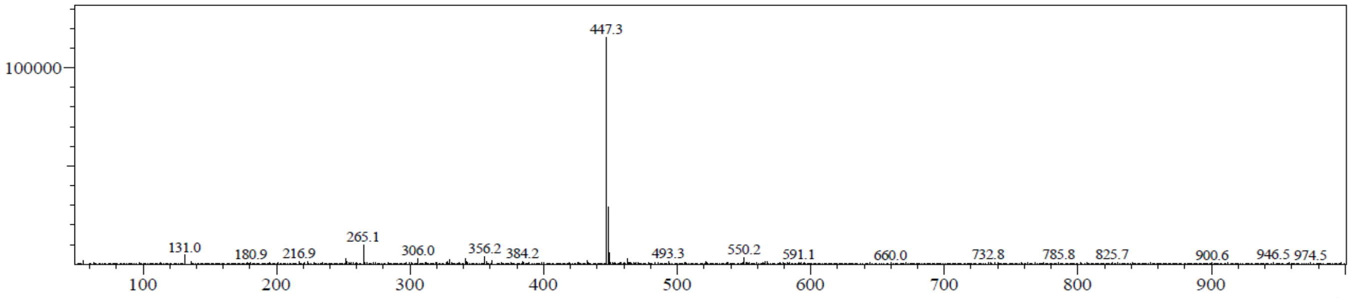

Figure S22. ESI-MS taken after 10 minutes showing the presence of $\mathbf{B_e}$ at 447.3 m/z.

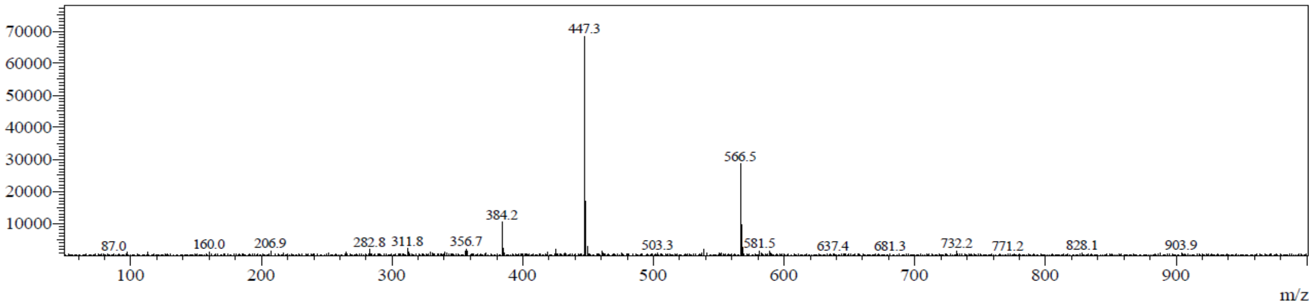

Figure S23. ESI-MS taken after 30 minutes showing the presence of $\mathbf{B_e}$ at 447.3 m/z and $\mathbf{C_e}$ at 566.5 m/z.

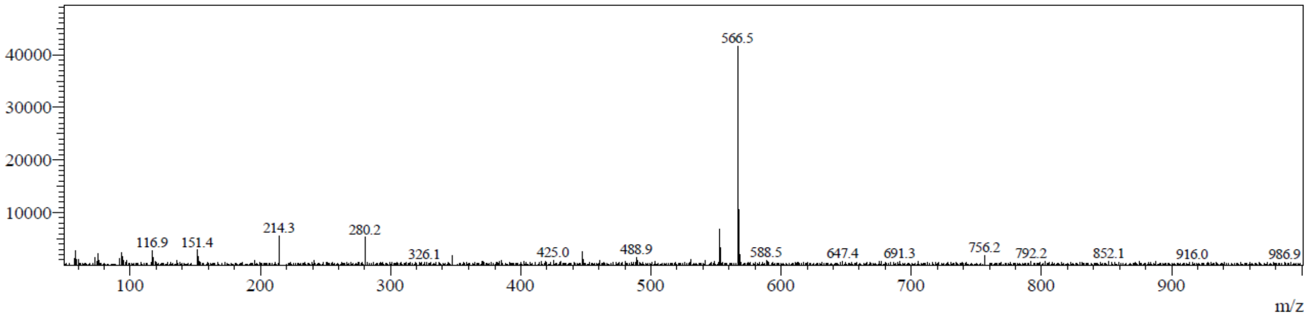

Figure S24. ESI-MS taken after 1.5 hours showing the of $\mathbf{C_e}$ at 566.5 m/z.

8.0 UV-Vis analysis of the reaction kinetics:

UV-Vis experiments could be used to monitor the kinetics of the conversion of ***I***$_e$ and ***II*** to **B**$_e$ and finally **C**$_e$ and determine the concentrations of the species. To do this a solution of ***I***$_e$ (2 µmolL^{-1}) and ***II*** (12.0 µmolL^{-1}) was prepared and **GdL** (12.0 µmolL^{-1}) was added. This reaction is well below the critical gelation concentration for **B**$_e$ and **C**$_e$. 10 minutes after the **GdL** addition a UV-Vis spectra was recorded and subsequently every 10 minutes up to a time of 110 minutes. Using this data with the Beer-Lambert law, concentrations of only **B**$_e$ and **C**$_e$ could be determined.

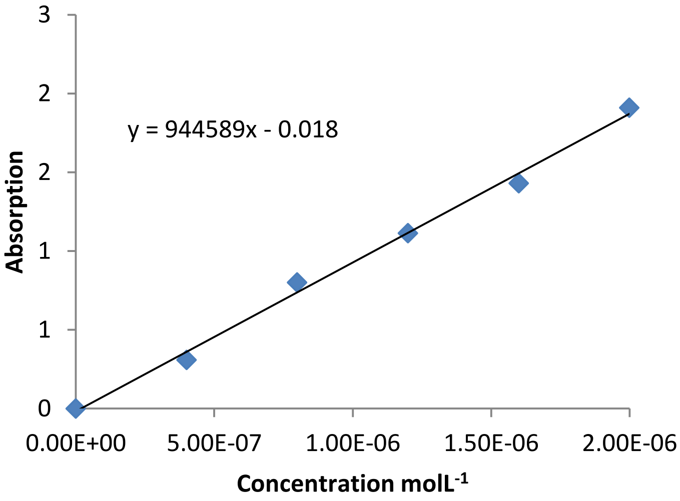

Figure S25. Determination of the molar absorption coefficient of **C**$_e$ at415 nm (ε_{C415}).

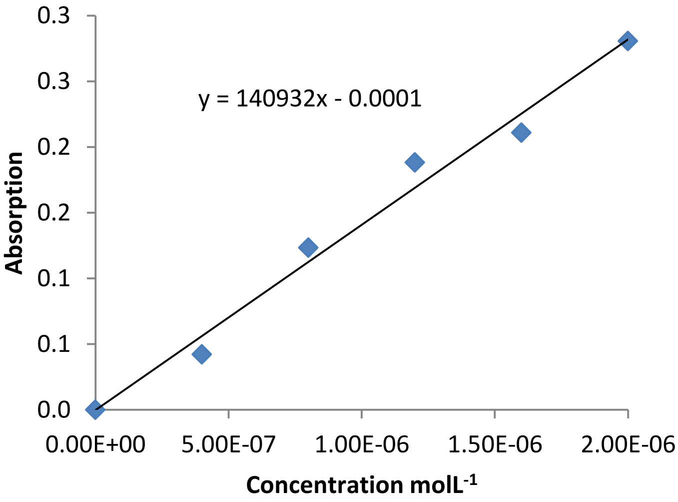

Figure S26. Determination of the molar absorption coefficient of **C**$_e$ at 300 nm (ε_{C300}).

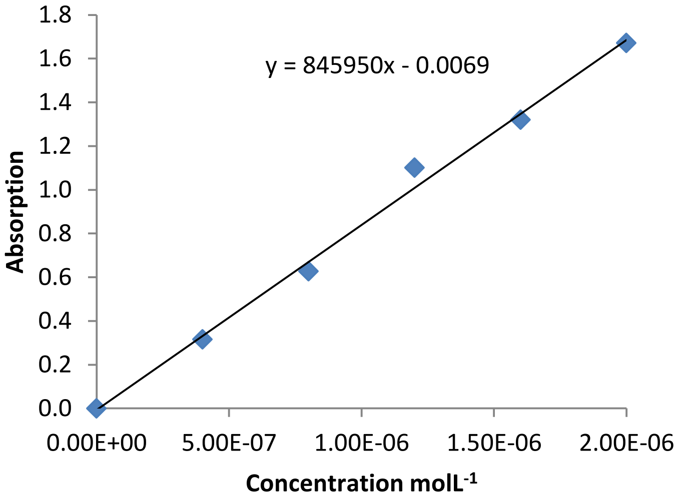

Figure S27. Determination of the molar absorption coefficient of **B$_e$** at 415 nm (ε_{B300}).

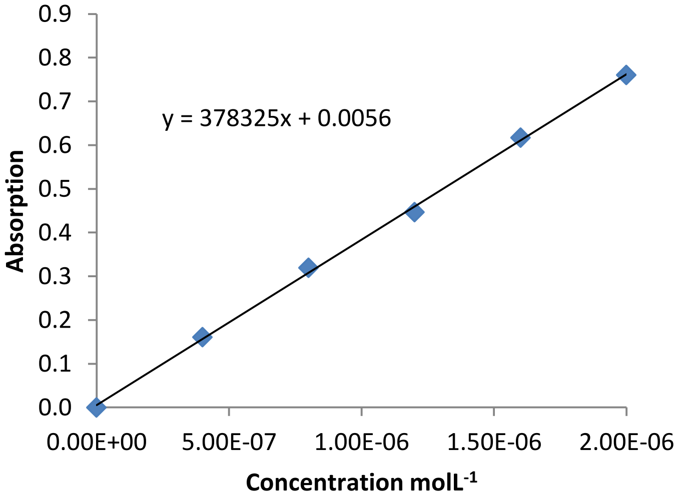

Figure S28. Determination of the molar absorption coefficient of **B$_e$** at 300 nm (ε_{B300}).

Concentration experiments were used of the pure compounds to determine ε at two wavelengths (300 and 415 nm) for **B$_e$** and **C$_e$**. A plot of concentration vs absorption will yield the molar absorption coefficient as the gradient of the straight line (Table S5).

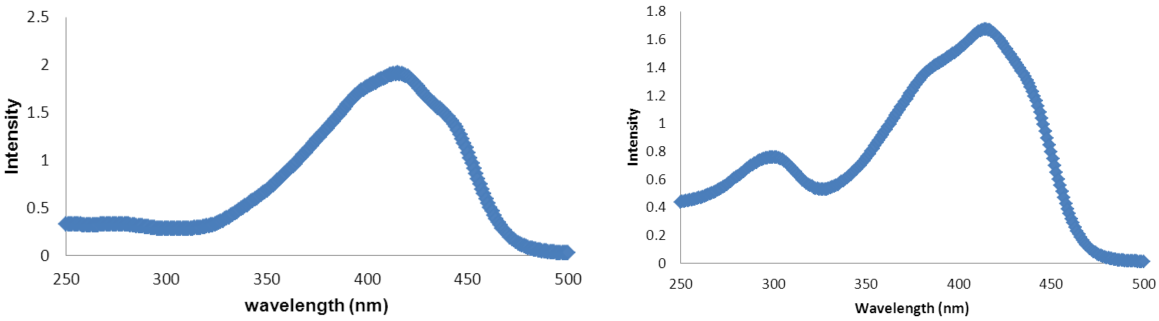

Figure S29. Figure showing the comparative spectral differences of **B$_e$** and **C$_e$** in water at the same concentration.

Table S5. Molar absorption coefficient.

Coefficient	Value
$\varepsilon_{\mathbf{Be}300}$	378000
$\varepsilon_{\mathbf{Be}415}$	846000
$\varepsilon_{\mathbf{Ce}300}$	141000
$\varepsilon_{\mathbf{Ce}415}$	945000

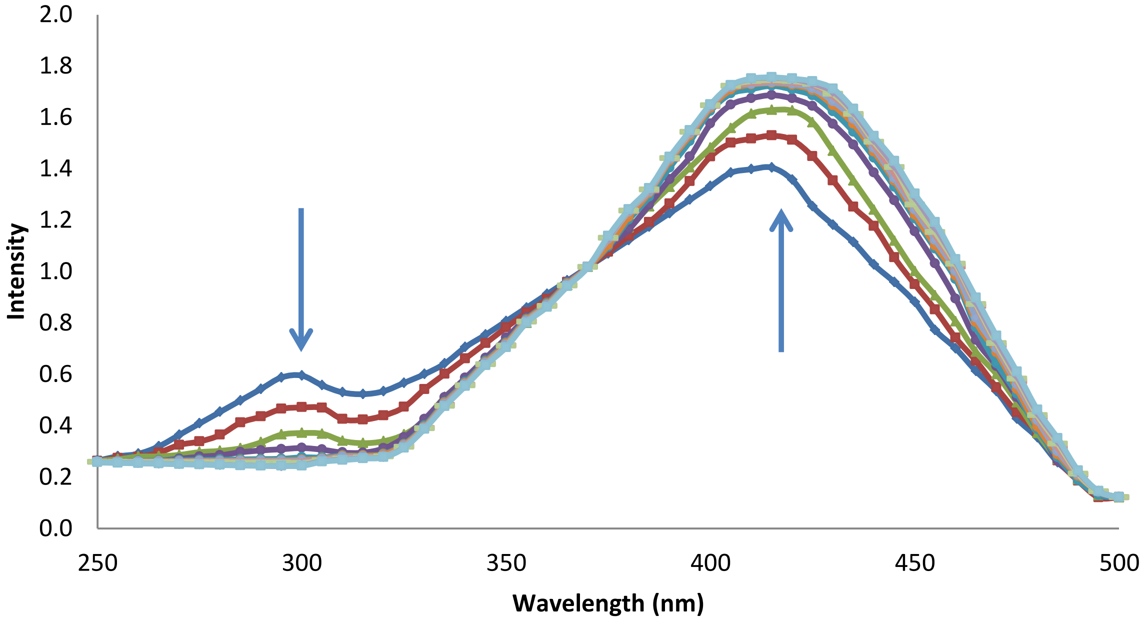

Figure S30. UV-Vis monitoring of the reaction $\mathbf{B_e}$ to $\mathbf{C_e}$ with **GdL** starting at 10 minutes after the addition of **GdL** recorded at 10 minute intervals. A line between data points has been added to guide the eye. Arrows indicate the change in adsorption with time.

Table S6. Concentrations of $\mathbf{B_e}$ and $\mathbf{C_e}$ at the specified times and the intensities of the UV-Vis spectra of the reaction solution at 300 and 415 nm.

Time	[B_e]	[C_e]	Intensity 415nm	Intensity 300 nm
10	1.18	0.129	1.4047	0.5953
20	0.76	0.754	1.5288	0.4712
30	0.121	1.30	1.6283	0.3717
40	0.157	1.57	1.6866	0.3134
50	0.175	1.75	1.7228	0.2772
60	0.181	1.80	1.7329	0.2671
70	0.182	1.82	1.7356	0.2644
80	0.184	1.83	1.7386	0.2614
90	0.187	1.87	1.745	0.255
100	0.191	1.91	1.7534	0.2466
110	0.193	1.92	1.7558	0.2442

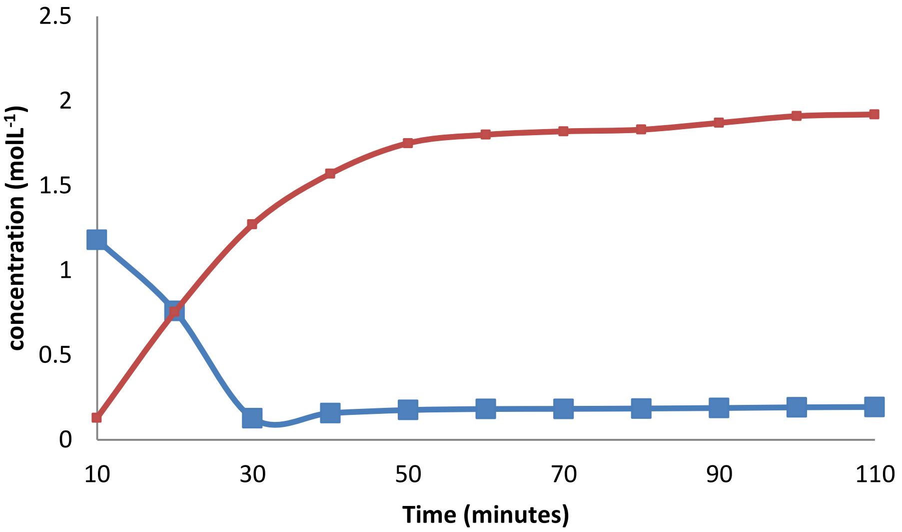

Figure S31. Plot of concentrations of **B_e** (blue) and **C_e** (red) against time **(**since **GdL** addition) showing the reaction kinetics. A line between data points has been added to guide the eye.

The kinetics data collected in the UV-Vis experiment clearly shows the concentration of **C_e** increasing at the expense of **B_e** which decreases. The total concentration of **B_e** + **C_e** should be equal to 2 µmolL^{-1} which is equal to the limiting reagent ***I_e***. The initial concentration of **B_e** + **C_e**, recorded at 10 minutes is noticeable lower than the expected 2 µmolL^{-1} which is indicative of the presence of **A_e**.

8. 2 Analysis of reaction kinetics by UV-Vis at pH 8

The previously described experiment was repeated, however instead of **GdL** the stock solution was adjusted to pH 8 with the addition of NaOH allowing for a secondary experimental data set of the reaction kinetics at pH 8 in water. The first set of data being the MS data.

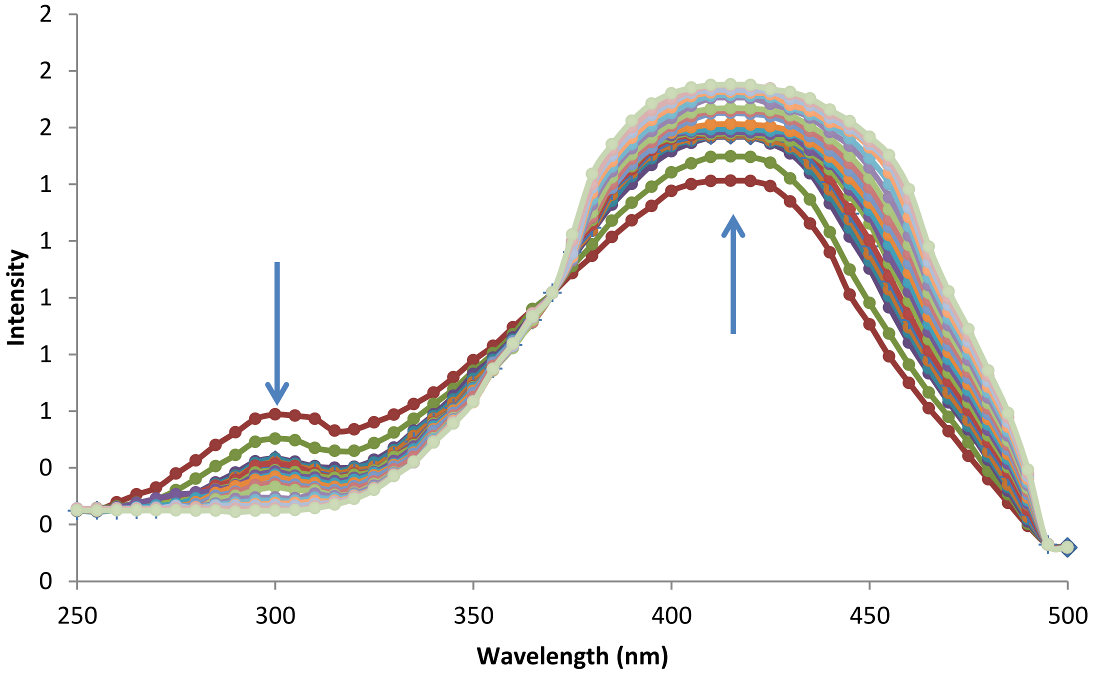

Figure S32. UV-Vis monitoring the reaction **B$_e$** to **C$_k$** with at pH 8. A line between data points has been added to guide the eye. Arrows indicate the change in absorption with time.

Table S7. Concentrations of **B**$_e$ and **C**$_k$ at the specified times calculated from the intensities of the UV-Vis spectra of the reaction solution at 300 and 415 nm.

Time	[B$_e$]	[C$_k$]	Intensity 415 nm	Intensity 300 nm
4	0.998	0.016	1.5759	0.4241
10	1.902	0.014	1.4124	0.5876
20	1.887	0.032	1.4976	0.5024
30	1.804	0.0251	1.5668	0.4332
40	1.769	0.286	1.5691	0.4309
50	1.712	0.311	1.5714	0.4286
60	1.666	0.344	1.5729	0.4271
70	1.475	0.444	1.5763	0.4237
80	1.422	0.513	1.579	0.4201
90	1.385	0.591	1.5843	0.4157
100	1.187	0.652	1.5953	0.4047
110	1.099	0.754	1.6124	0.3876
120	1.042	0.866	1.6509	0.3491
130	1.015	0.906	1.6581	0.3419
140	1.001	0.924	1.6684	0.3316
150	0.993	0.939	1.7056	0.2944
160	0.976	0.957	1.7145	0.2855
170	0.964	0.978	1.7256	0.2744
180	0.952	1.04	1.7324	0.2676
360	0.596	1.412	1.7485	0.2515
1200	0.158	1.918	1.7514	0.2486

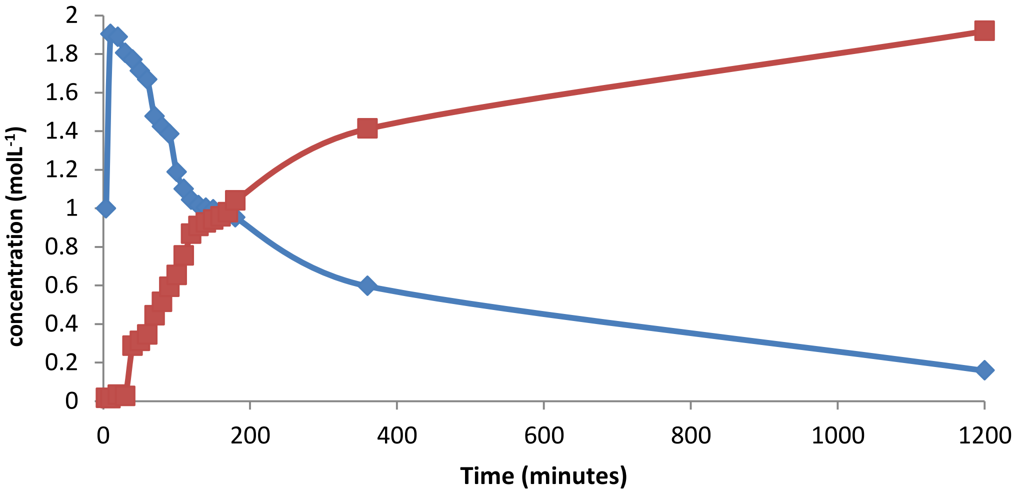

Figure S33 Plot of concentrations of **B**$_e$ (blue) and **C**$_k$ (red) against time (pH 8). A line between data points has been added to guide the eye. This data matches that of the MS kinetic data.

9.0 UV-Vis Spectra

9.1 Experimental description

Further characterisation of the in solution species could be done using UV-Vis spectroscopy. This was done by preparing solutions of gel $\mathbf{C_k}$, $\mathbf{C_e}$ and $\mathbf{B_e}$ isolates below their critical gel solutions to give a gelator concentration 2.0 μmolL^{-1}. The absorptions for the isolated $\mathbf{C_k}$ and $\mathbf{C_e}$ gelators were markedly different. The $\mathbf{C_k}$ gelator shows a maximum absorption at 350 nm meters (Fig. S52), in contrast the $\mathbf{C_e}$ gelator is noticeably red shifted with its maximum absorption at 420 nm (Fig. S53). Fig. 54 shows $\mathbf{B_e}$ to have a very similar spectrum to $\mathbf{C_e}$, however, with an addition secondary absorption peak at around 300nm.

9.2 UV-Vis absorption for C_k gelator

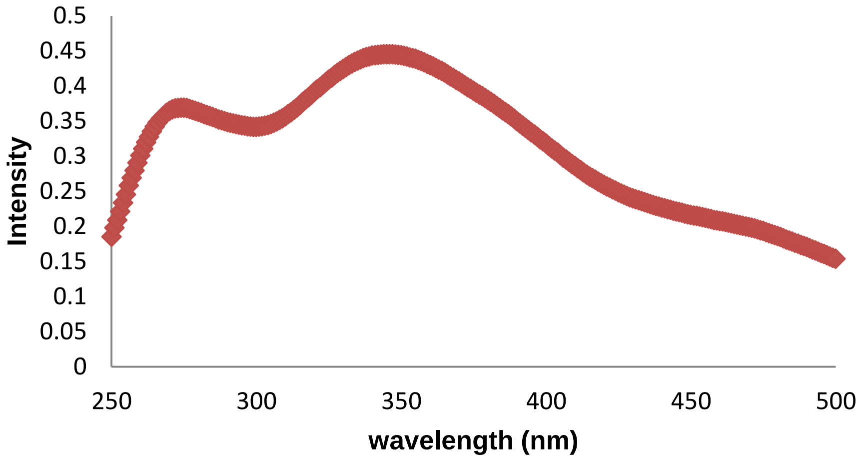

Figure S34. UV-Vis absorption spectra for solubilised $\mathbf{C_k}$ in slightly basic water.

9.3 UV-Vis absorption for C_e gelator

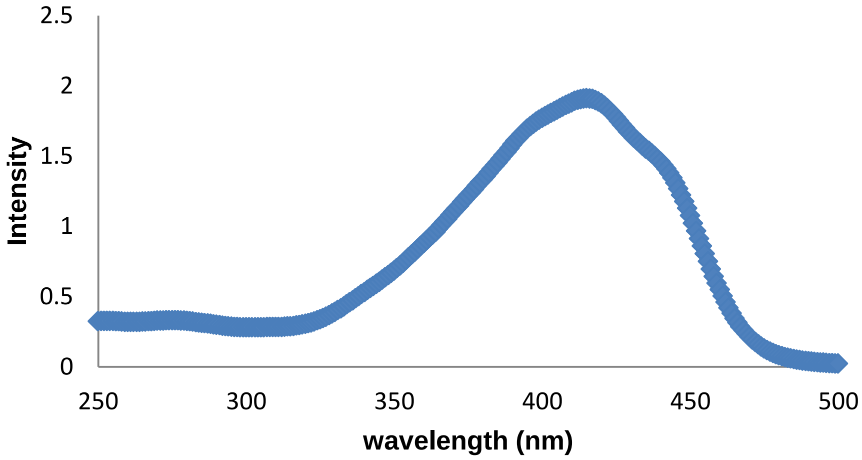

Figure S35. UV-Vis absorption spectra for solubilised $\mathbf{C_e}$ in slightly basic water.

9.4 UV-Vis absorption for B_e gelator

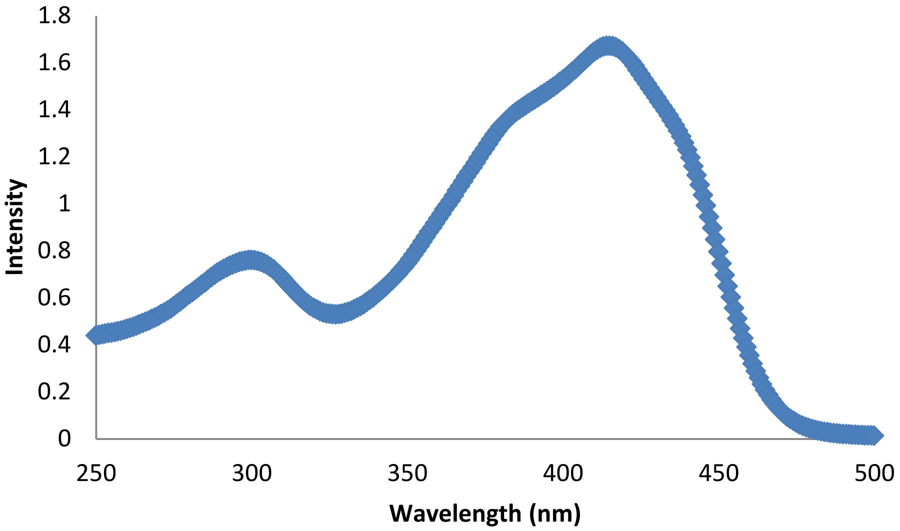

Figure S36. UV-Vis absorption spectra for solubilised $\mathbf{B_e}$ in slightly basic water.

10.0 Computational studies

As a means of species identification, computational studies of some of the potential species formed or deprotonated were performed. Predicted UV-Vis spectra allowed comparison between the experimental and theoretical absorptions resulting in compound identification both as isolated and dissolved species.

Computational details.

All the calculations were performed using Gaussian09d software[2]. Geometries of all conformers of keto (k) and enol (e) systems have been optimised using B3LYP density functional and 6-31G(d) basis set (presented in section 11.0 of SI). The influence of other available functionals on the structure has been studied and only minimal structural differences were observed thus B3LYP geometries have been chosen for further studies. TD-DFT has been used to study UV-Vis spectroscopy of given systems. Functional dependence on the spectroscopic properties has been examined. It was observed that the functional that produced results in closest agreement with experimental results is dispersion corrected B97D3 functional, thus it was used for further UV-Vis studies. Adding diffuse functions to the basis set shifts the spectra to the red of about 6 nm. The influence of solvation on the calculated spectra was recorded using universal continuum model SMD (Figure S38)[3]. Water and dimethylsulfoxide (DMSO) solvents were chosen for comparison with the experimental data.

Two types of spectra have been presented in the paper. First type contains spectral bands for only the lowest energy conformers of each tautomer (Figure S40, Figure S41). Second type of spectra contains spectral bands of ensemble spectra of all conformers of each tautomer obtained using Boltzman distribution, which gives a probability of finding a molecule in state of E_i energy:

$$P_i = \frac{e^{-\frac{E_i}{kT}}}{\sum_i e^{-\frac{E_i}{kT}}}$$

where k is a Boltzman constant and T is thermodynamic temperature (Figure S38).

Reaction pathway diagrams for $\mathbf{C_k}$, $\mathbf{C_e}$ and $\mathbf{B_e}$ are presented in section 11.1 of SI. These include tables with electronic energy differences between products of different steps of reactions as well as activation barriers calculated with B3LYP functional and 6-311G(d) basis set at 298K. To calculate the barrier size for each step of reaction we have performed a transition state search (location of stationary point with one imaginary frequency).

10.1 Experimental UV-Vis results for C_e and C_k isolates in DMSO

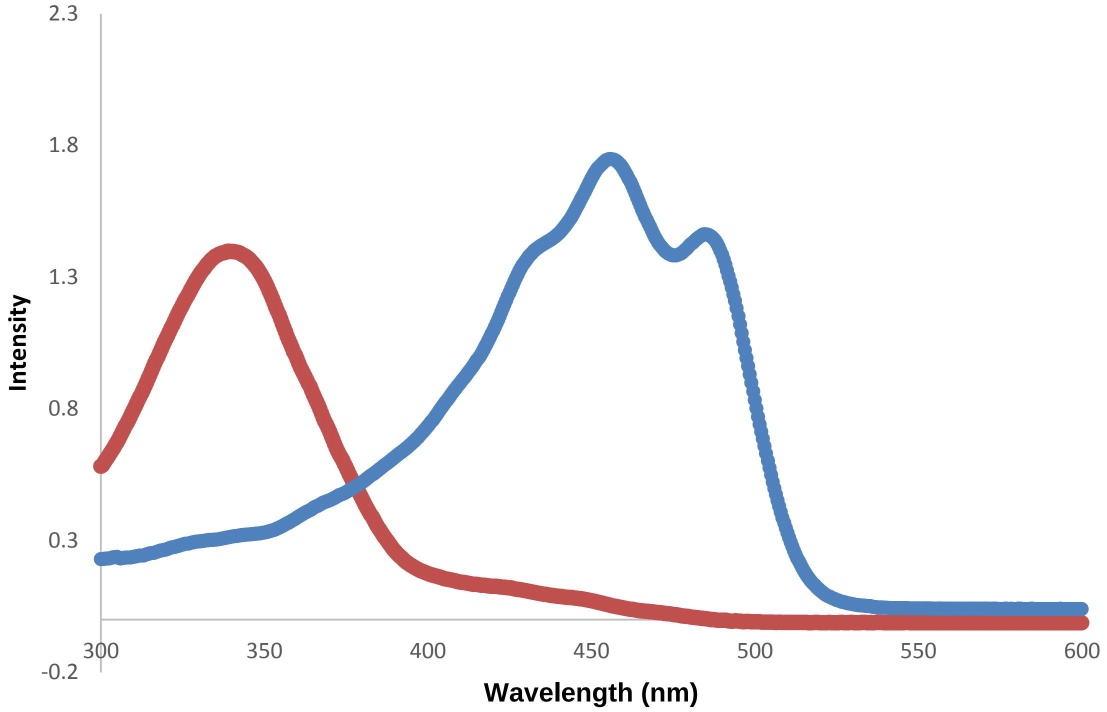

Figure S37. UV-Vis absorption spectra for isolated $\mathbf{C_e}$ (blue) and $\mathbf{C_k}$ (red) compounds dissolved in DMSO. Wavelength (nm) (x-axis) plotted against intensity (y-axis). Spectra produced with a gelator concentration 2.0 μmolL^{-1}.

UV-Vis spectra recorded in DMSO for the dried and washed isolate of the gels $\mathbf{C_e}$ and $\mathbf{C_k}$. The absorption pattern for the keto form (gel $\mathbf{C_k}$ isolate) shows a maximum at 340 nm. The maximum absorption of the enol form relative to the keto form (gel $\mathbf{C_e}$ isolate) is distinctly red shifted. The $\mathbf{C_e}$ maximum absorption appears at 460 nm. The NMR in *d*-DMSO and computational work confirm the identity of the species.

10.2 Calculated UV-Vis specta for C_e and C_k in DMSO

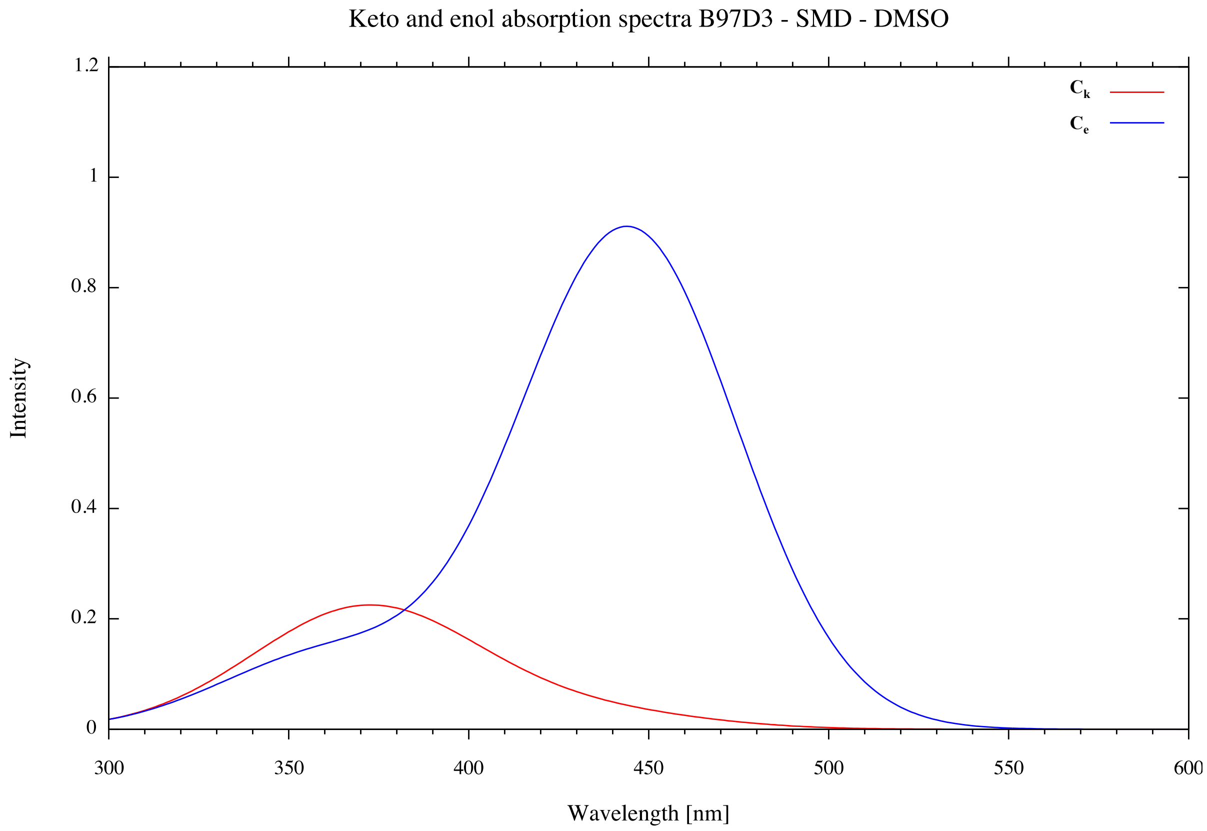

Figure S38. Calculated UV-Vis ensemble spectra for $\mathbf{C_e}$ (C_3 structure) and $\mathbf{C_k}$ (C_3 and C_s structures). Level of theory TD-B97D3/6-31G(d); first 6 bright states chosen for spectroscopic properties; 30nm Gaussian broadening chosen for both keto and enol forms; SMD solvation model with DMSO as a solvent. Wavelength [nm] (x-axis) against intensity (y-axis).

A good qualitative correlation can be observed by comparing the calculated theoretical UV-Vis spectra in DMSO for the $\mathbf{C_k}$ and $\mathbf{C_e}$ forms with the experimental data.

10.3 Experimental UV-Vis results for B anion recorded in water

The UV-Vis spectra for the dissolved anionic species $\mathbf{B_e}$ could also be recorded in water (Fig. S39) and compared to a calculated UV-Vis spectra of the mono-deprotonated $\mathbf{B_e}$ in water (Fig. S40). Again there is a good correlation between experimental and theoretical calculations. The experimental spectra shows two maximums, one at 300 nm and one at 410 nm compared to the theoretical spectra maximums at 300 nm and 400 nm.

10.3 Experimental UV-Vis results for B_e anion recorded in water

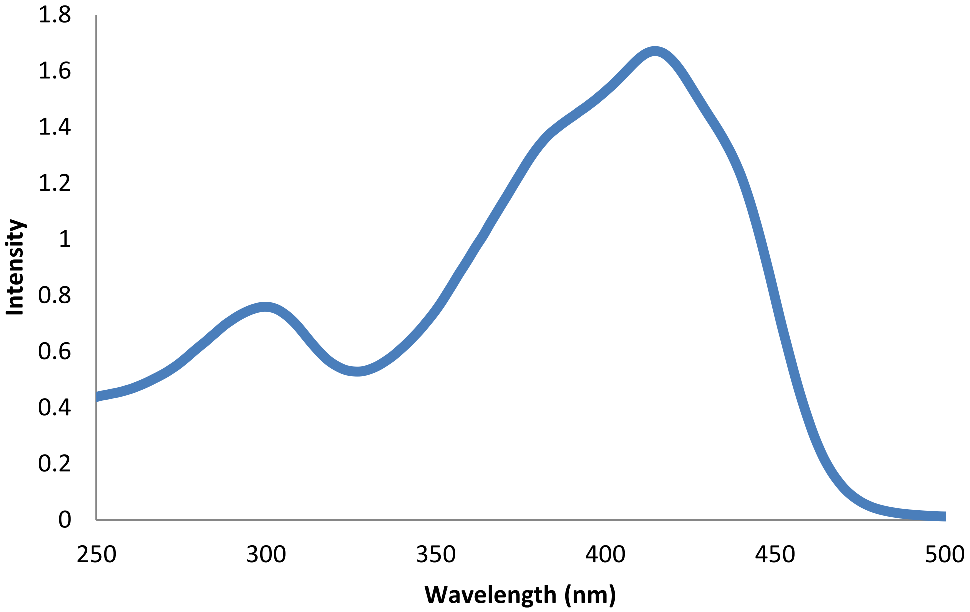

Figure S39. UV-Vis absorption spectra for $\mathbf{B_e}$ anion dissolved in slightly basic water.

10.4 Calculated UV-Vis specta for gel B_e in water

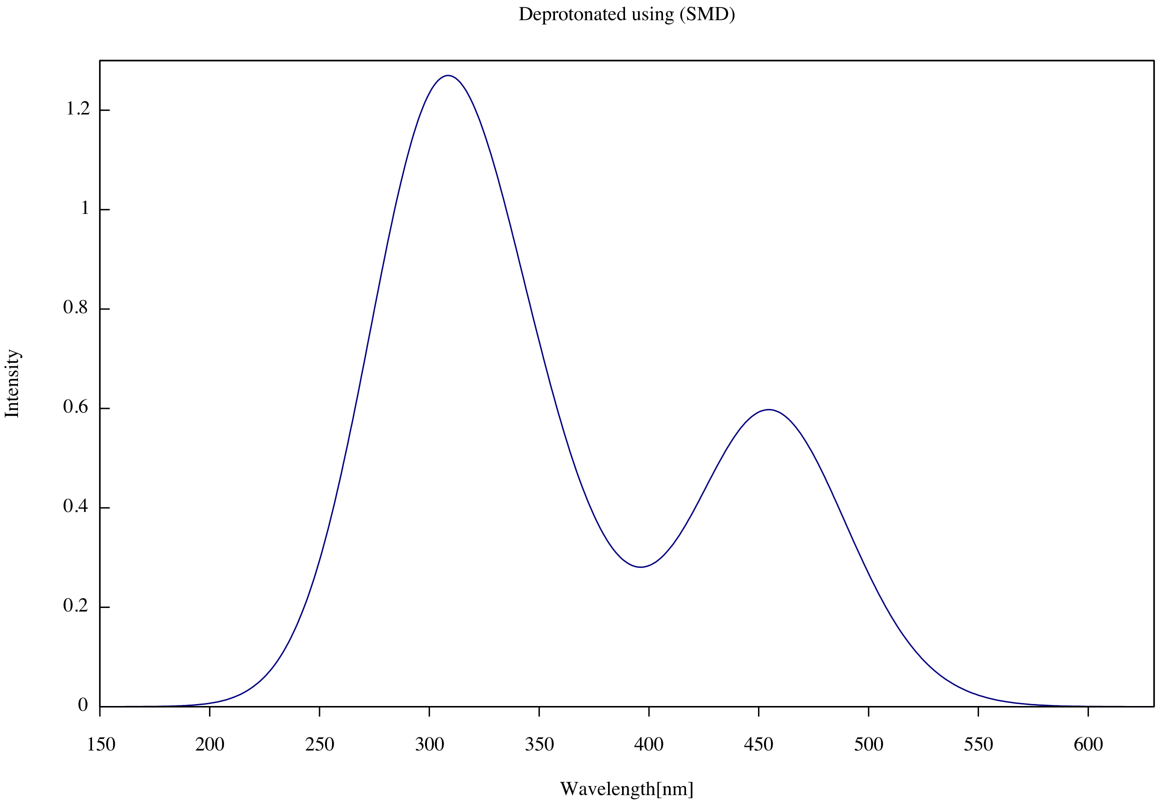

Figure S40. Deprotonated - TD-B97D3 – SMD with 6-31G(d) basis set with water as a solvent – 50 states included of mono-deprotonated $\mathbf{B_e}$ included with 30nm Gaussian broadening.

Similar calculations with **C$_k$** and **C$_e$** compounds as mono-deprotonated species confirmed that the dissolved state of the compounds as the deprotonated forms (Fig. S41).

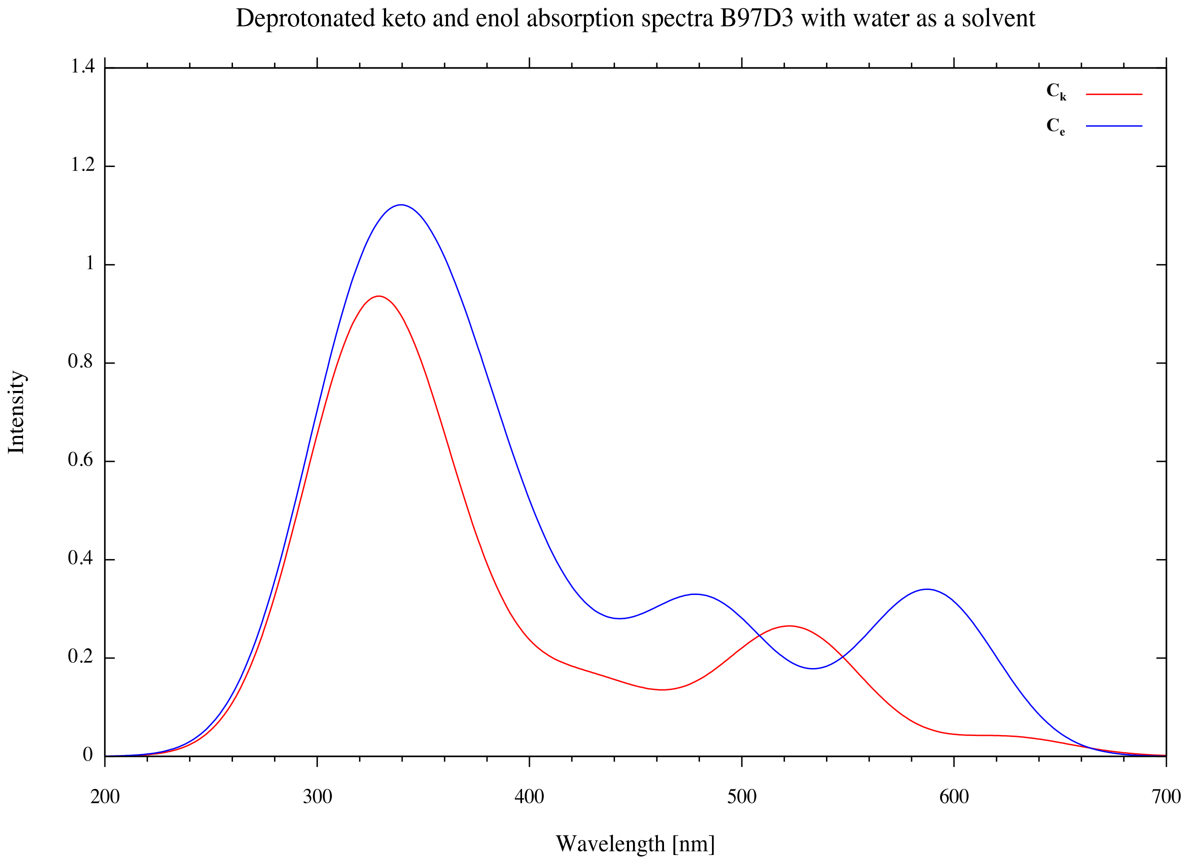

Figure S41. Deprotonated **C$_k$** and **C$_e$** species- TD-B97D3 – SMD with 6-31G(d) basis set and with water as a solvent – 50 states included with 30nm Gaussian broadening.

11.0 Computational elucidation of tautomerisation and C$_k$ conformers behaviour

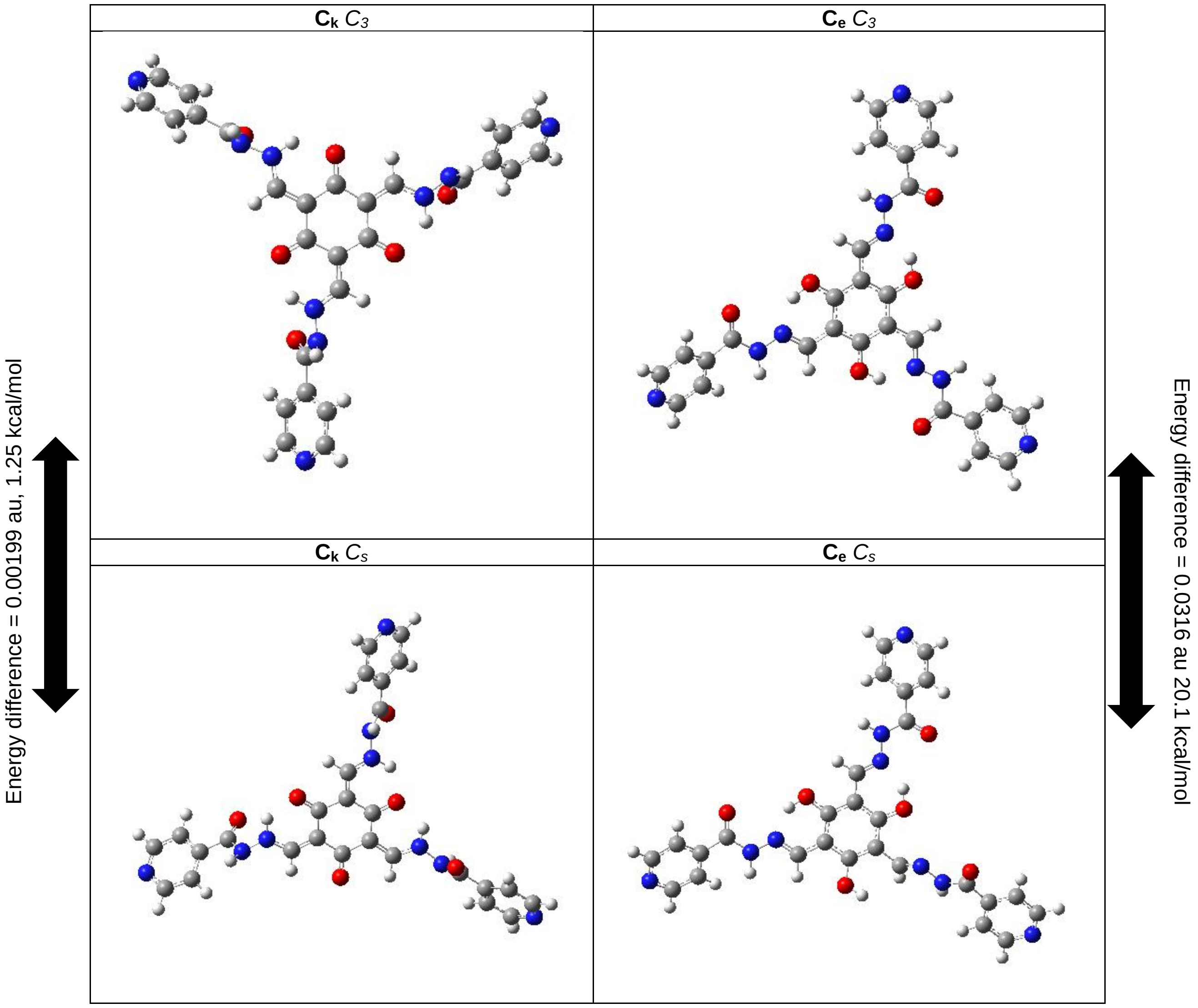

Figure S42. Calculated GS energetics for tripodal **C$_e$** and **C$_k$** species in both the ***C_s*** and ***C_3*** geometries calculated using B3LYP/6-31G(d).

From the calculated GS energetics (Fig. S42) it is possible to gain an understanding into both the tautomeric and geometric forms adopted by the **C$_e$** enol and **C$_k$** keto species. The tautomer compound adopts is initially dependent on the pH of the solution in which the species was formed/dissolved, with the **C$_e$** form being observed in low pH solutions (pH 8 and below) and **C$_k$** form in high pH solutions (pH 9.5-12). The tautomeric form adopted by the compound can be cycled between the **C$_k$** and **C$_e$** forms indefinitely by adjusting the pH using acidic and basic solutions. Similar 3 tripodal salicylideneanilines species are only reported in the keto tautomeric form.[4]

With the tripodal **C$_e$** species there is the potential for it to adopt a *C_3* or *C_s* geometric conformation. However the C_3 conformation is lower in energy compared to the *C_s* conformation by around 20.1 kcal/mol, which is significant enough to stop the molecule adopting a *C_s* conformation. This is confirmed by the NMR data, which shows the enol form in only in the *C_3* conformation.

The **C$_e$** form exists solely in the *C_3* form. This is in stark contrast to the tripodal keto **C$_k$** species. The *C_3* and *C_s* conformations of the molecule are effectively isoenergetic with an energy difference of only 1.25 kcal/mol.

This results in the molecule existing as a statistical 50/50 mixture of the C_3 and C_s forms as determined by NMR experiments.

11.1 Compound I_e - C_{3H} (I_e to I_k) reaction pathway

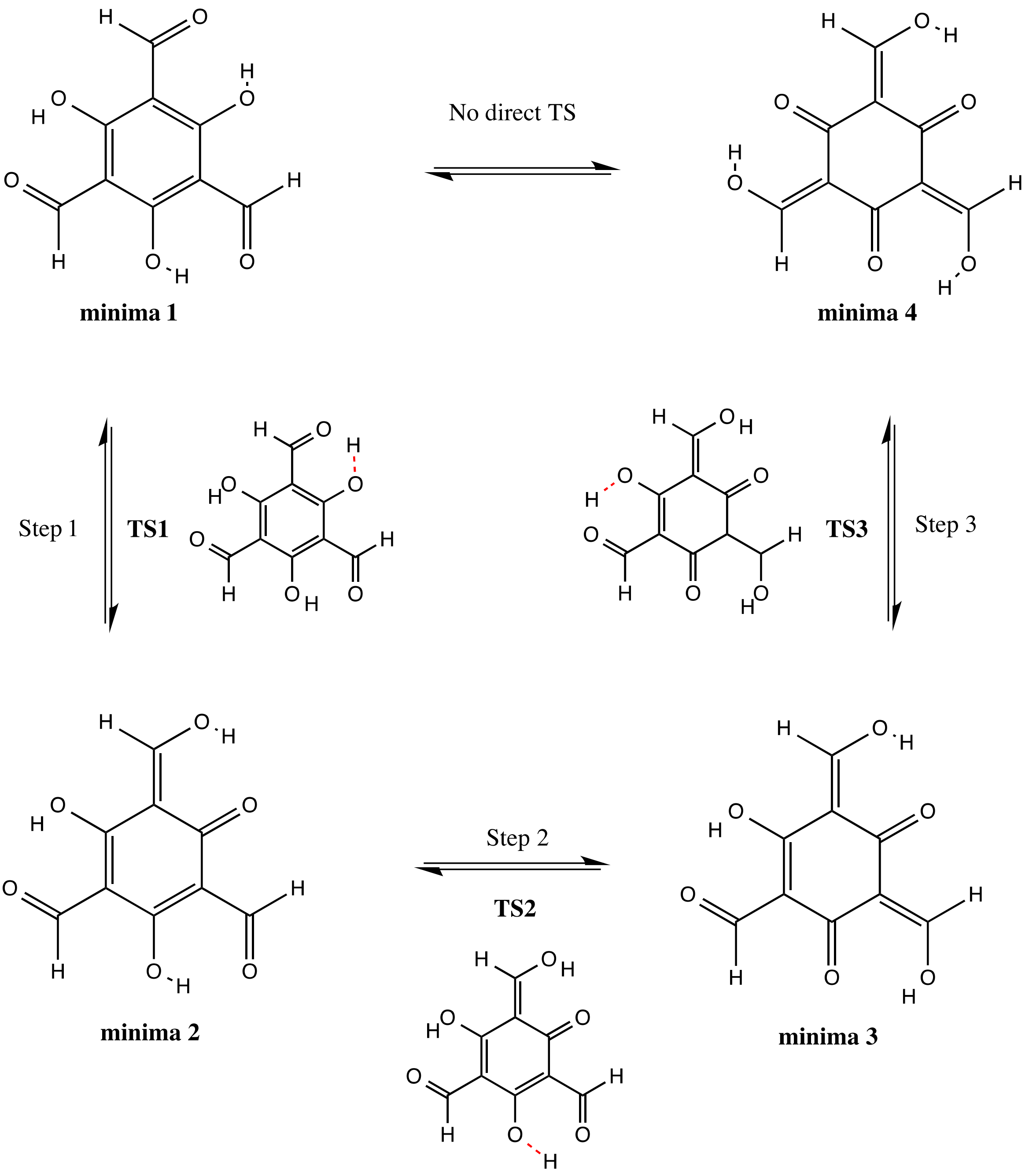

Figure S43. Reaction pathway diagram of the C_3 conformer of $\boldsymbol{I_e}$, I_e-I_k tautomerisation.

Table S8. Electronic energy differences for different paths of reaction. B3LYP with 6-311G(d) basis set at 298K.

Reaction	**$\Delta_r E_{electronic}$ (kcal/mole)**
Step 1	5.0
Step 2	1.6
Step 3	0.5

Table S9. Electronic energy barrier size for different paths of reaction. B3LYP with 6-311G(d) basis set at 298K.

Reaction	**$\Delta_{activ} E_{electronic}$ (kcal/mole)**
Step 1	6.3
Step 2	4.3
Step 3	3.9

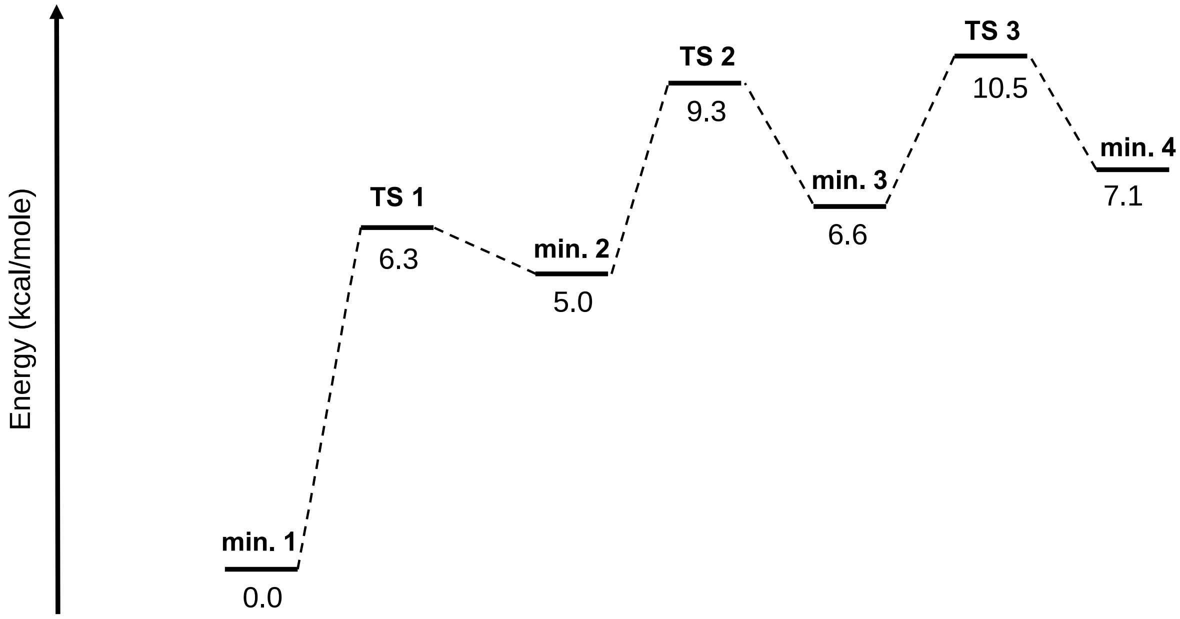

Figure S44. Reaction pathway diagram ***I***I_e (C_3) enol form to I_k (C_3) keto form showing energy differences between the tautomers and the barrier size between them. B3LYP with 6-311G(d) basis set at 298K; electronic energy in kcal/(mol).

11.2 Compound *A* – (A_e to A_k) reaction pathway – where arm is $NHCOC_5H_4N$

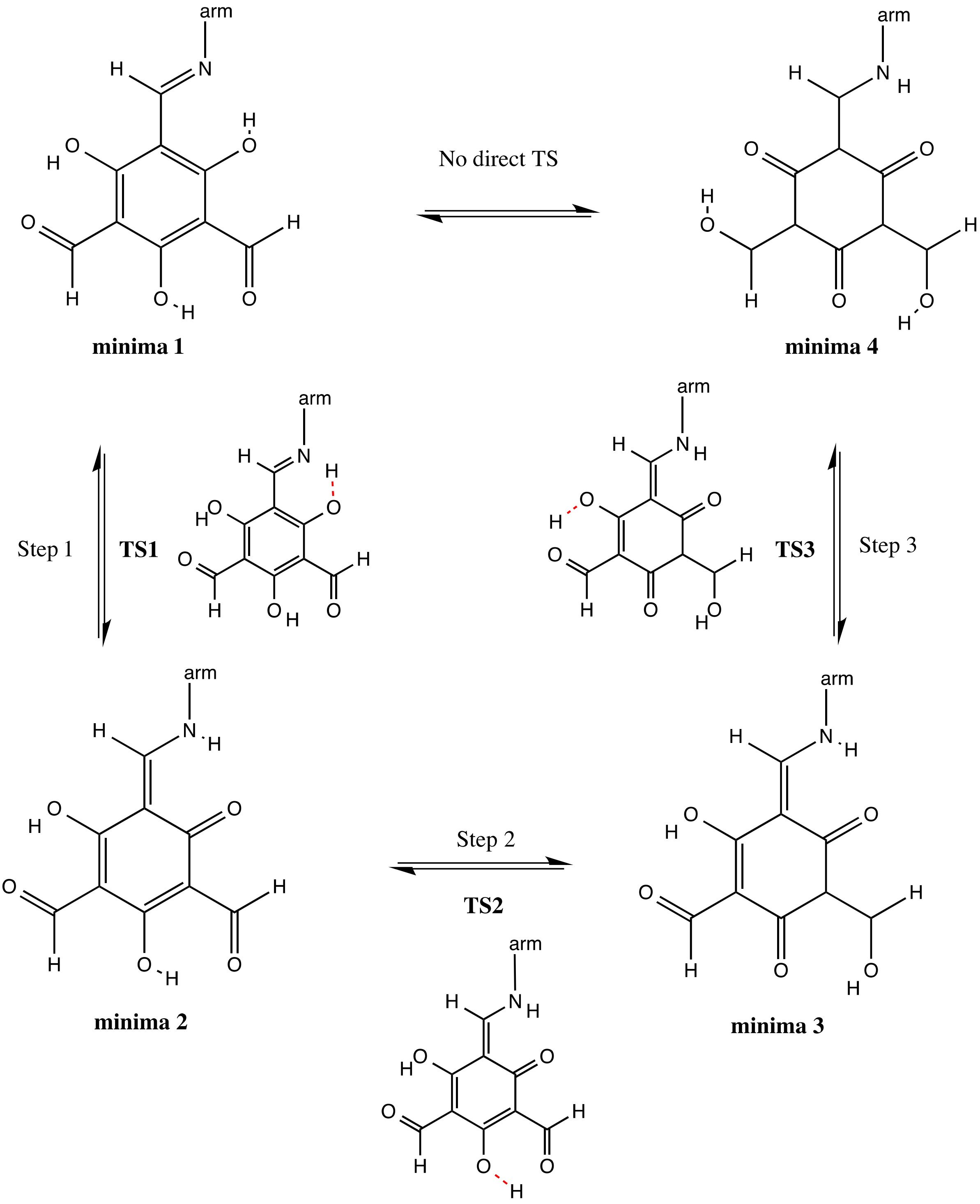

Figure S45. Reaction pathway diagram of the $\boldsymbol{A_e}$ to the $\boldsymbol{A_k}$ tautomerisation.

Reaction	$\Delta_r E_{electronic}$ (kcal/mole)
Step 1	1.8
Step 2	1.5
Step 3	1.1

Table S10. Electronic energy differences for different paths of reaction (where arm is $NHCOC_5H_4N$); B3LYP with 6-311G(d) basis set at 298K.

Reaction	$\Delta_{activ} E_{electronic}$ (kcal/mole)
Step 1	7.4
Step 2	4.3
Step 3	3.8

Table S11. Electronic energy barrier size for different paths of reaction (where arm is $NHCOC_5H_4N$). B3LYP with 6-311G(d) basis set at 298K.

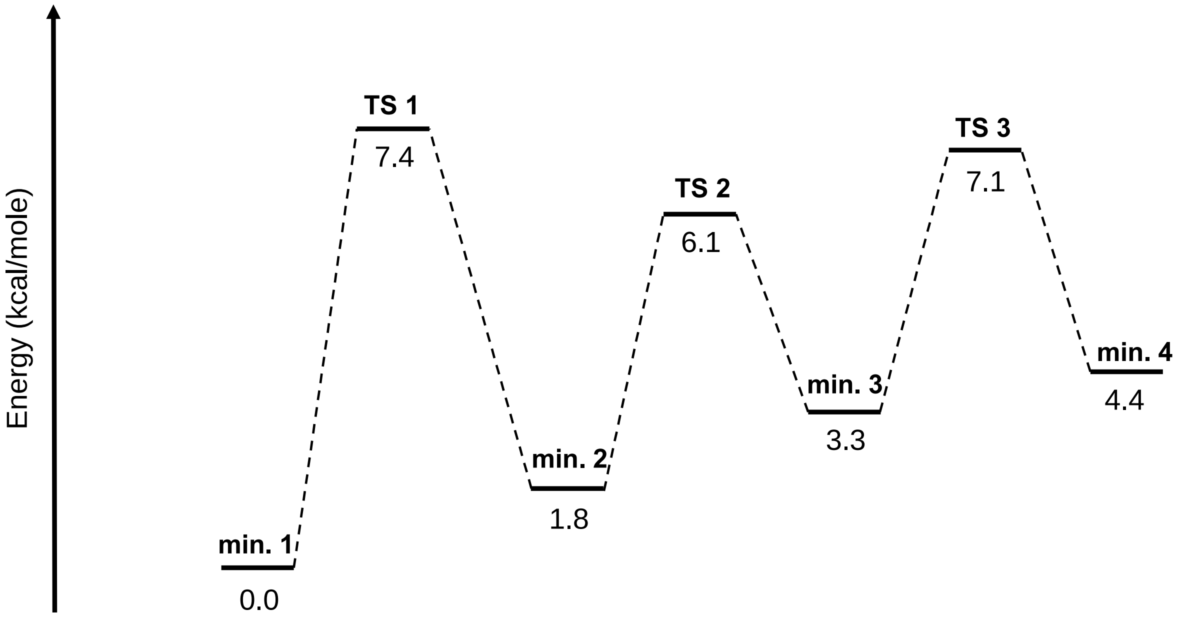

Figure S46. Reaction pathway diagram ***A***$_e$ form to A_k form showing energy differences between the tautomers and the barrier size between them. B3LYP with 6-311G(d) basis set at 298K; electronic energy in kcal/(mol).

11.3 Compound B – (B_e to B_k) reaction pathway

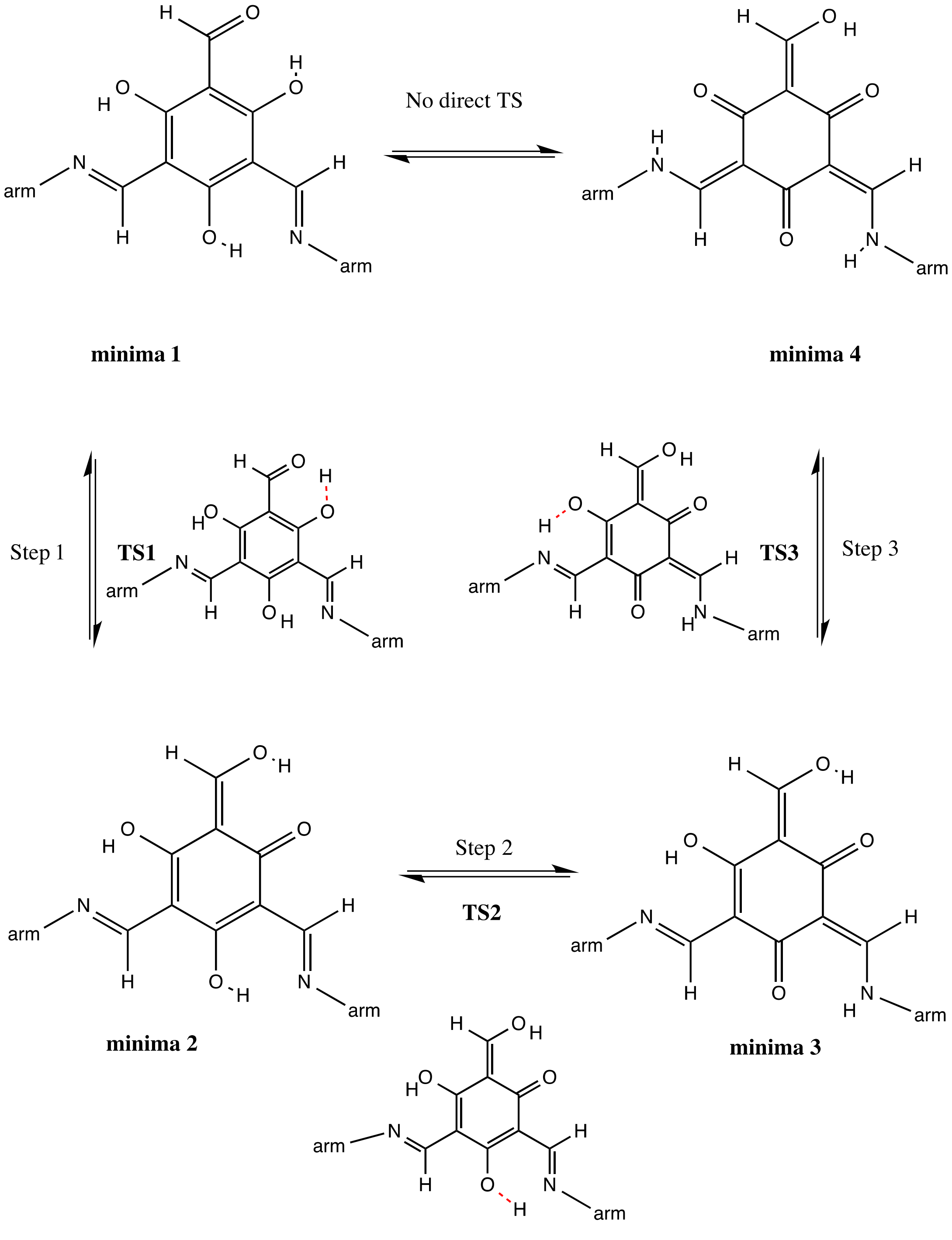

Figure S47. Reaction pathway diagram of the ***B**$_e$* to the ***B**$_k$* tautomerisation.

Reaction	**$\Delta_r E_{electronic}$ (kcal/mole)**
Step 1	5.3
Step 2	-1.6
Step 3	-2.2

Table S12. Electronic energy differences of different paths of reaction. B3LYP with 6-311G(d) basis set.

Reaction	**$\Delta_{activ} E_{electronic}$ (kcal/mole)**
Step 1	6.5
Step 2	5.9
Step 3	5.9

Table S13. Electronic energy barrier size of different paths of reaction. B3LYP with 6-311G(d) basis set.

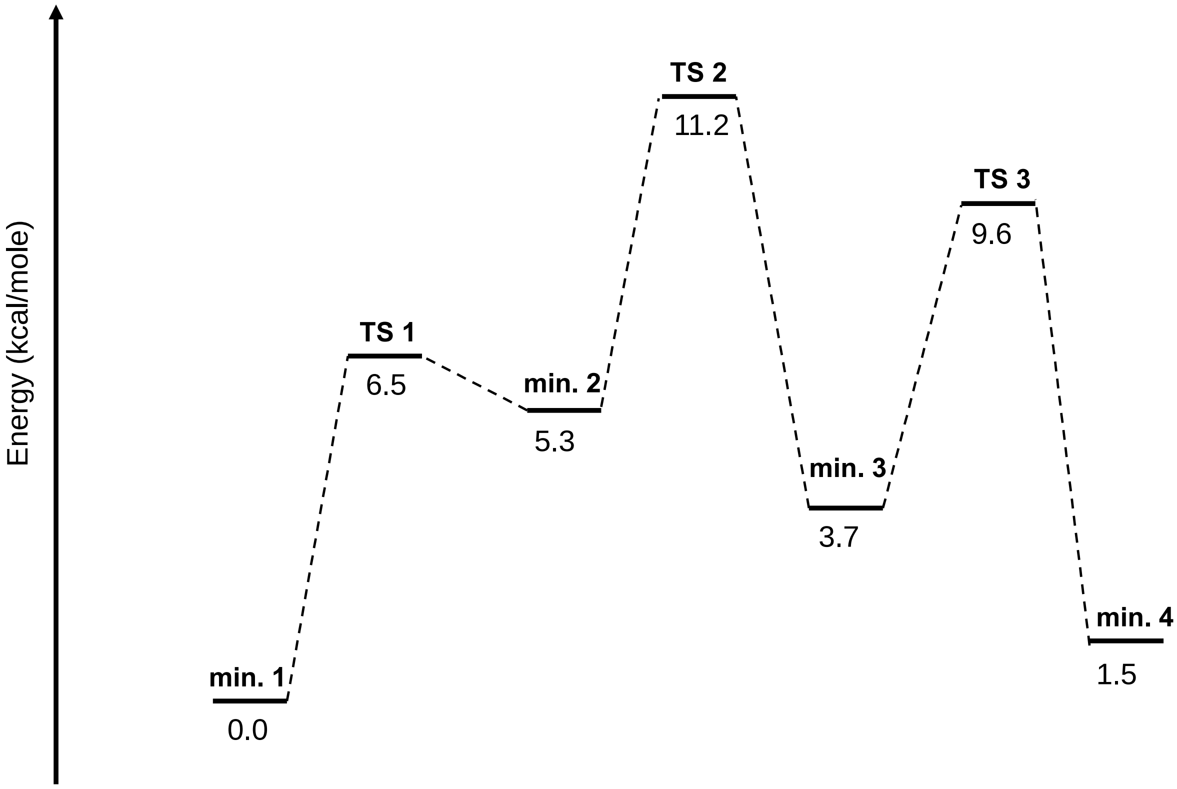

Figure S48. Reaction pathway diagram B_e form to B_k form showing energy differences between the tautomers and the barrier size between them. B3LYP with 6-311G(d) basis set at 298K; electronic energy in kcal/(mol).

11.4 Compound C – (C_e to C_k) reaction pathway – where arm is $NHCOC_5H_4N$

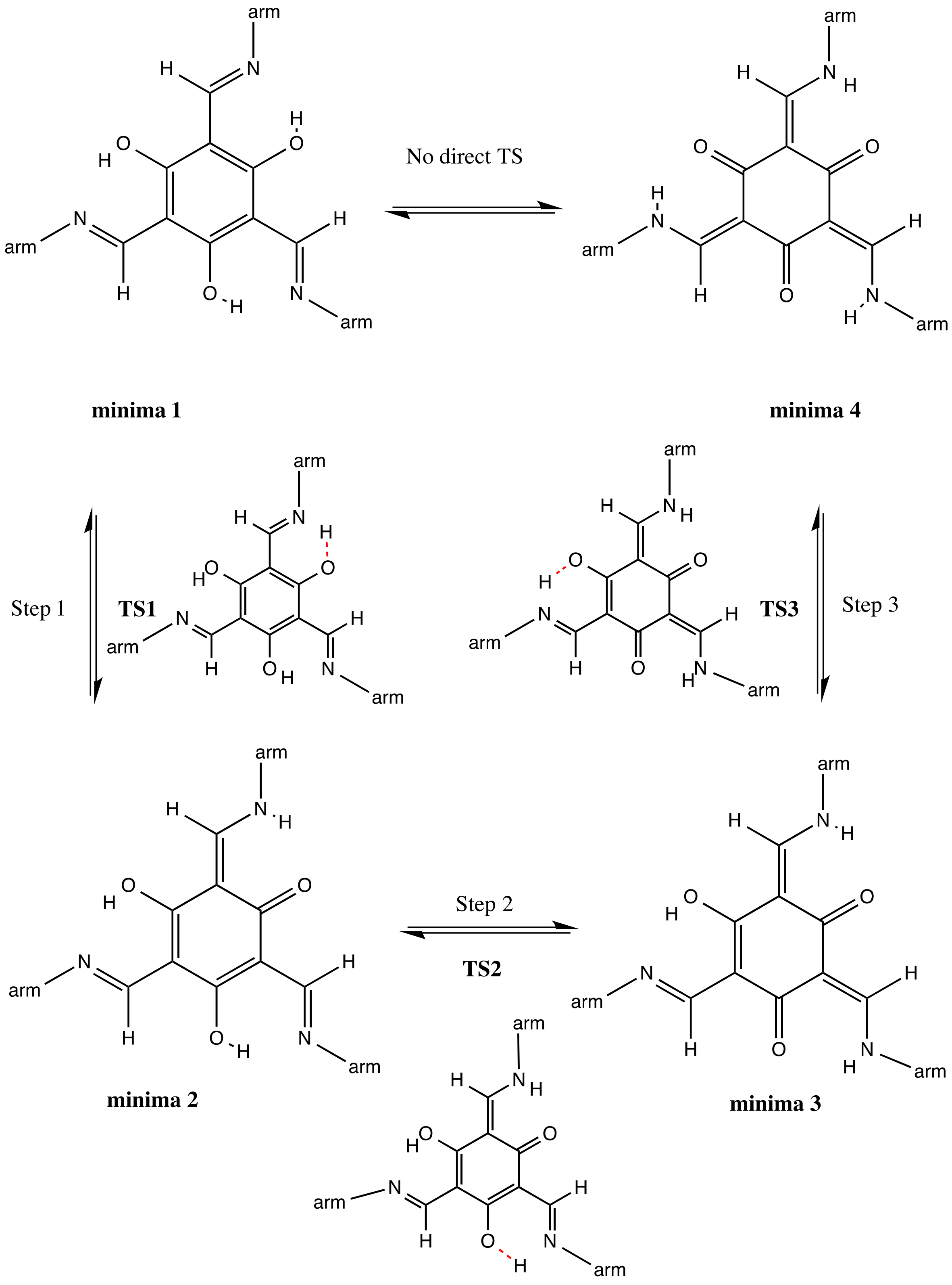

Figure S49. Reaction pathway diagram of the C_e C_3 to the C_k C_3 tautomerisation.

Reaction	$\Delta_r E_{electronic}$ (kcal/mole)
Step 1	4.7
Step 2	-3.4
Step 3	-1.9

Table S14. Electronic energy differences for different paths of reaction (where arm is $NHCOC_5H_4N$). B3LYP with 6-311G(d) basis set at 298K.

Reaction	$\Delta_{activ} E_{electronic}$ (kcal/mole)
Step 1	10.1
Step 2	4.2
Step 3	6.0

Table S15. Electronic energy barrier size for different paths of reaction (where arm is $NHCOC_5H_4N$). B3LYP with 6-311G(d) basis set at 298K.

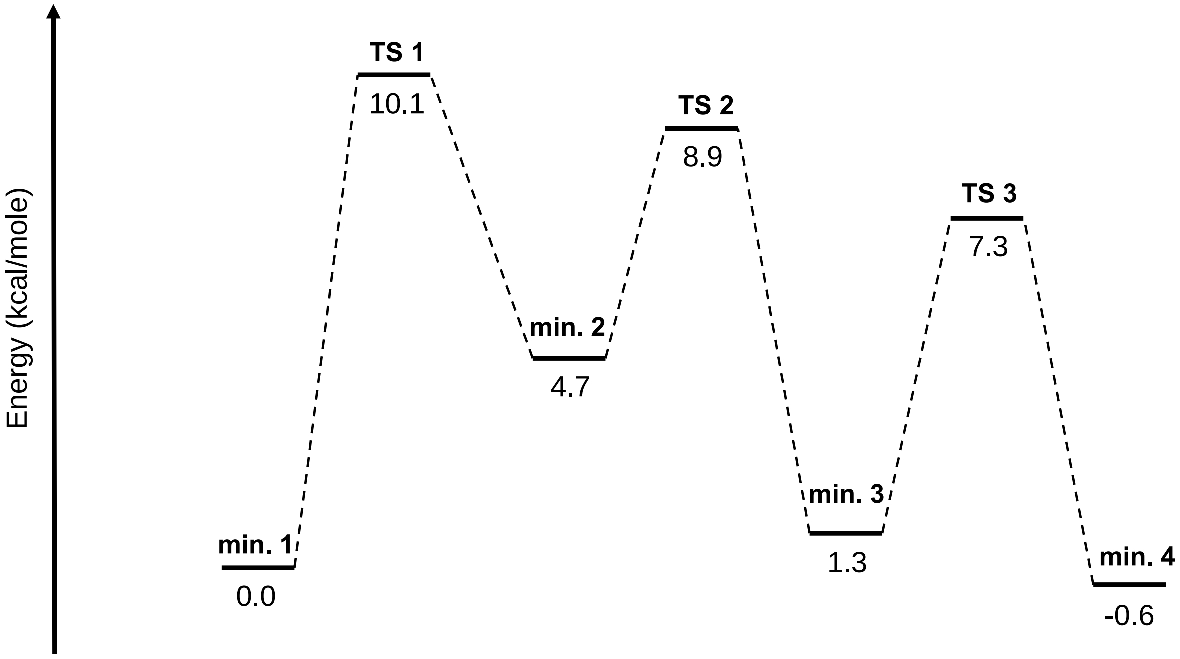

Figure S50. Reaction pathway diagram C_e form to C_k form showing energy differences between the tautomers and the barrier size between them. B3LYP with 6-311G(d) basis set at 298K; electronic energy in kcal/(mol).

This reaction pathway clearly shows the keto (**C_k**) to be slightly more thermodynamically stable than the enol form (**C_e**). The slight difference in stability helps to explain the ease at which **C_e** can convert to **C_k** and visa versa. There exists a significant kinetic barrier for the conversion between the two forms hinting at while at low pH the kinetically trapped **C_e** is found.

11.5 Computational prediction of the Supramolecular interactions

We investigated trimers of structure **B_e**, **C_e**, and **C_k** using B97D with a 6-311g(d) basis. We have previously used this level of theory to satisfactorily explain aggregated supramolecular structures in similar systems. We note that the dispersion correction is essential in this regard. The structures shown are optimised and confirmed as minima via analytical frequency calculation.

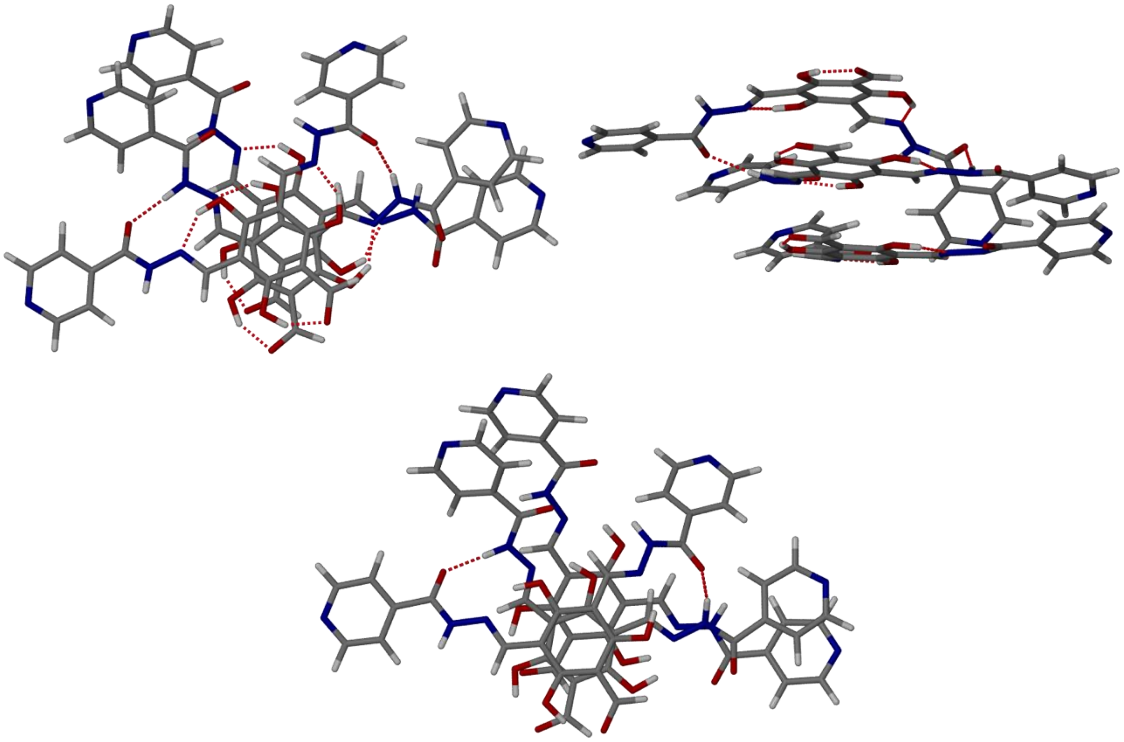

Figure S51. Various views of the calculated supramolecular arrangement of 3 molecules of compound **B_e** with dashed lines showing hydrogen bonding.

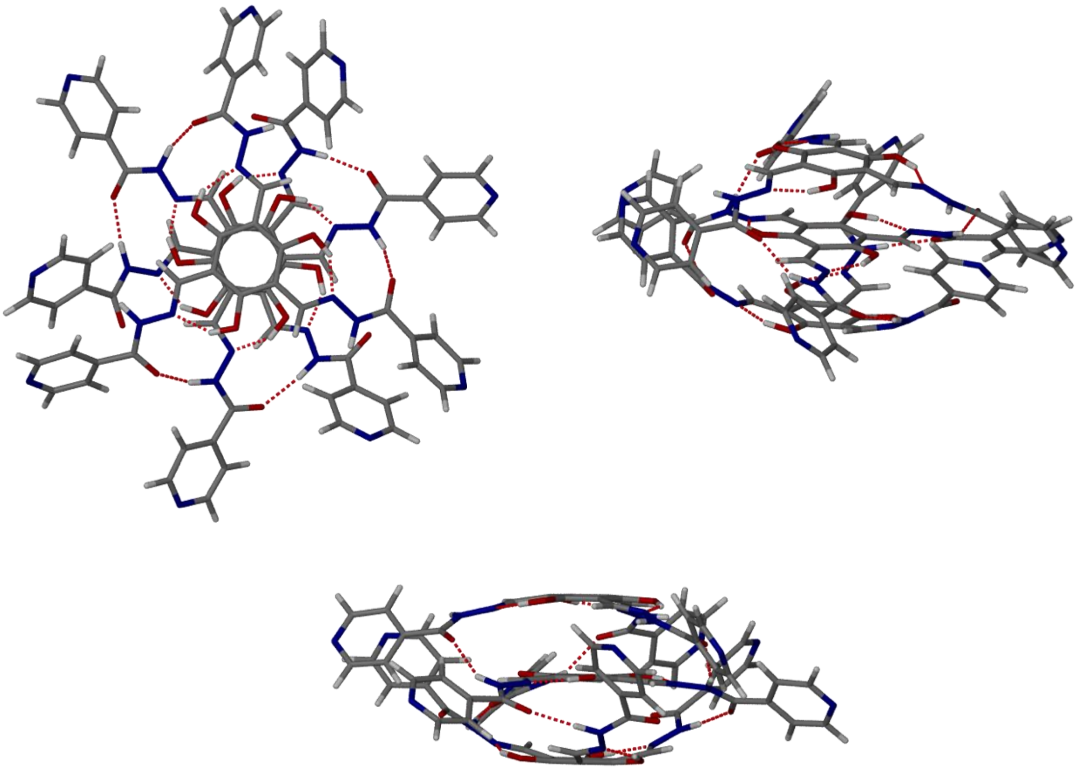

Figure S52. Various views of the calculated supramolecular arrangement of 3 molecules of compound **C$_e$** with dashed lines showing hydrogen bonding.

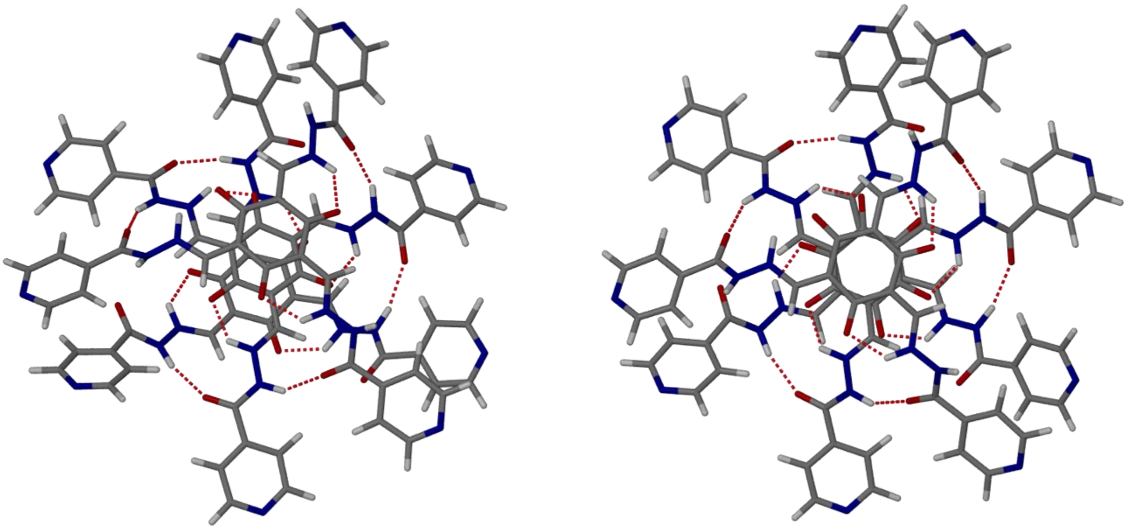

Figure S53. Various views of the calculated supramolecular arrangement of 3 molecules of compound **C$_k$** with dashed lines showing hydrogen bonding.

12.0 Powder X-ray Diffraction data for dried gel samples

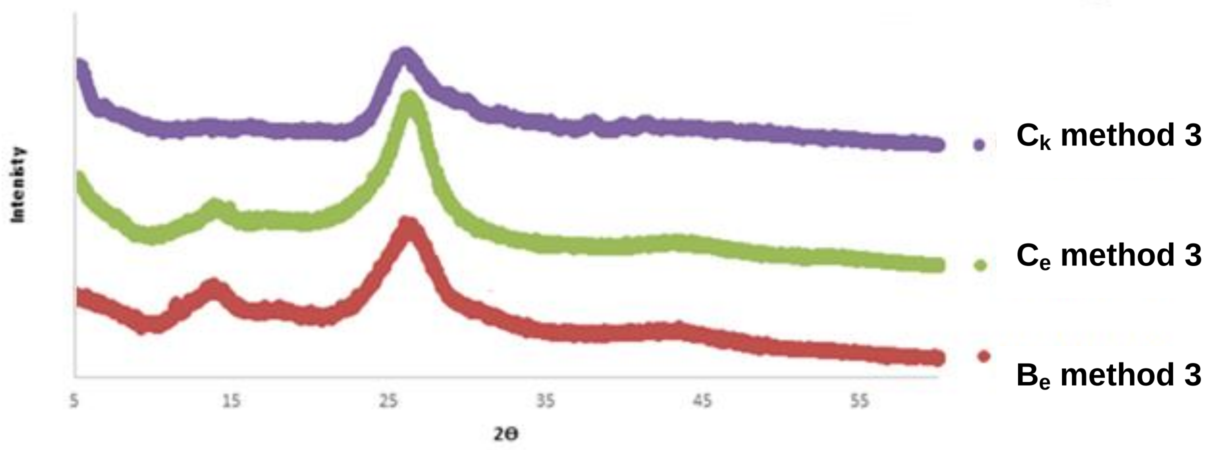

Figure S54. Powder X-Ray Diffraction patterns for each gel produced by each individual method.

Powder diffraction patterns were obtained from the prepared dried gel samples. The samples were transferred to the sample holder all of which should a similar characteristic broad reflection at approximately 26^o. This corresponded to the following *d* spacings:

$\mathbf{C_k}$ method 1 = 3.38 Å

$\mathbf{C_e}$ method 1 = 3.36 Å

$\mathbf{B_e}$ method 2 = 3.36 Å

Powder diffraction of dried samples show the samples have little crystalline order. The *d* spacings are indicative of the molecular stacking distance within the fibres of 3.34 – 3.39 Å, very similar to that known for benzene-1,3,5-triamide supramolecular polymers and gels.

13.0 Apparent *pK*$_a$ determination

The apparent *pK*$_a$ of **C$_e$** and **B$_e$** isolates could be determined in the following manner. The gel or synthesised **C$_e$** isolates (250 mg) were mixed with 25 ml water to create a suspension, to this suspension solid NaOH was added with stirring will the pH was constantly monitored until a pH of 10.2 had been achieved. Once the pH had stabilised at 10.2 aliquots of 0.1 M HCl (150 μL) were added with stirring. The pH was recorded after every aliquot. Data was plotted as acid addition against pH (Figs. S62 and S63) and the apparent *pK*$_a$ was taken to be a range over which the pH change plateaus^5.

13.1 Apparent *pK*$_a$ of C$_e$

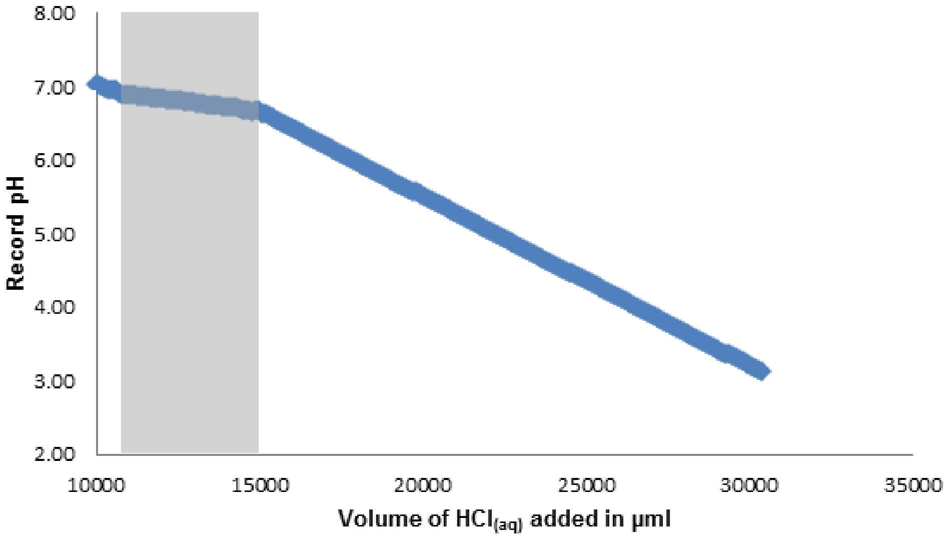

Figure S55. *pK*$_a$ determination of **C$_e$** showing and apparent *pK*$_a$ of 6.8 with a range of 6.9-6.7 as taken the be the observed plateau region shown in the shaded area. The graph at 10000 μL to highlight the plateau area which is often difficult to see.

13.2 Apparent *pK*$_a$ of B$_e$

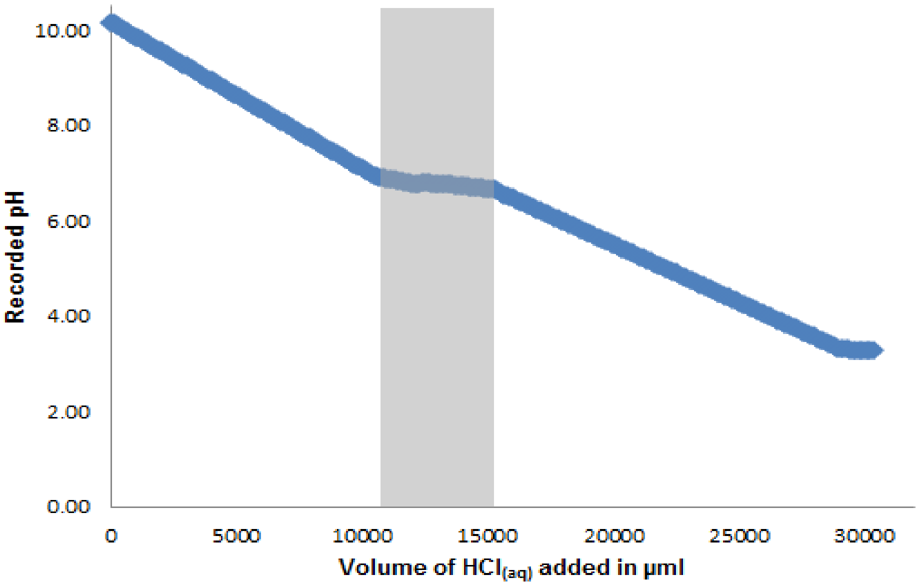

Figure S56. *pK*$_a$ determination of **B$_e$** isolate showing and apparent *pK*$_a$ of 6.6 with a range of 6.9-6.7 as taken to be the observed plateau region shown in the shaded area.

14.0 Gelation using ex situ prepared gelator

By synthesis and ultisation of the ex situ prepared gelator **C$_e$** it is possible to produce gels **C$_e$** and **C$_k$** through the subsequently described means.

14.1 Ex situ synthesis of C$_e$:

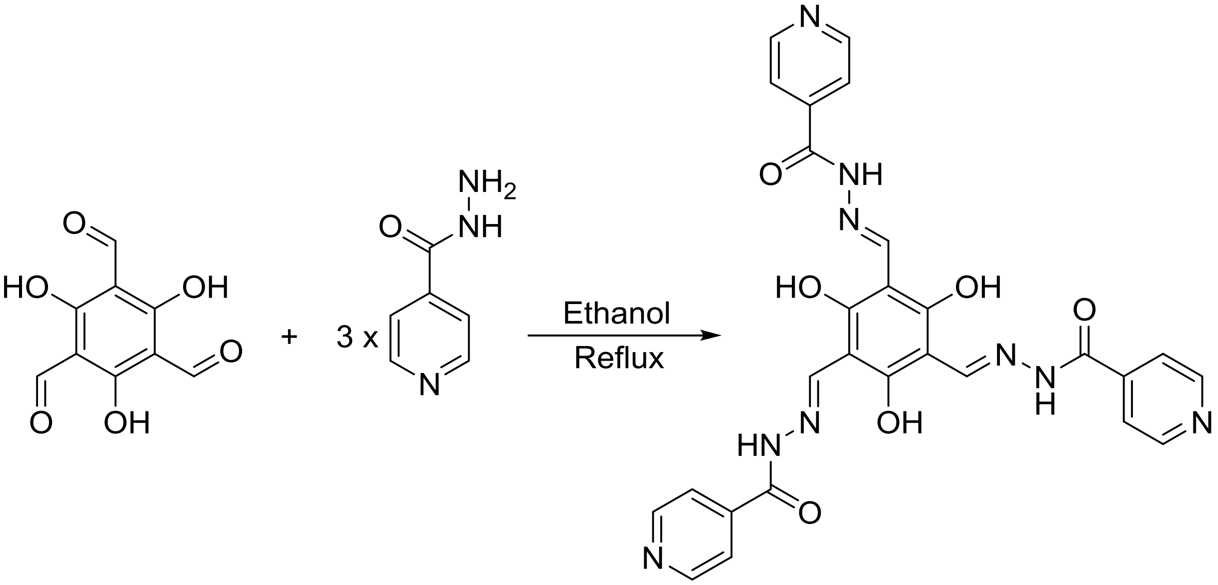

Figure S57. Reaction overview for the synthesis of **C$_e$** (N-[(E)-[2,4,6-trihydroxy-3,5-bis[(E)-(pyridine-4-carbonylhydrazono)methyl]phenyl]methyleneamino]pyridine-4-carboxamide).

To a mixture of 1,3,5-triformylphloroglucinol (***I$_e$***) (0.25 g, 1.19 mmol, 1 equiv.) and isonicotinc acid hydrazide (***II***) (0.50 g 3.69 mmol, 3.1 equiv.) ethanol (50 ml) was added. The resulting suspension was brought to reflux and the reaction was allowed to proceed for 4 hours to produce a bright yellow suspension. This was then allowed to cool to room temperature before being filtered to yield a yellow solid. This solid was then washed with water (4 × 50 ml) before being collected and dried in an oven overnight (80°C) to yield the final product ***C$_e$***.

14.1.1 Yield: 93 %, 0.63 g (M.W. 567.51 gmol^{-1})

14.1.2 ^{1}H NMR(d$_6$-DMSO, J/Hz, δ/ppm): 13.79 (broad s, 3H, Ar-OH), 12.47 (broad s, 3H, -NH-), 8.94 (s, 3H, -CHN), 8.79 (d, J = 5.03, 3H, Ar-H), 7.84 (d, J = 5.43, 3H, Ar-H)

14.1.3 ^{1}H NMR D_2O (d$_2$-D_2O, J/Hz, δ/ppm): 8.58 (d, J = 5.77, 6H, Ar-H), 8.48 (s, 3H, -CHN), 7.82 (d, J = 5.27, 6H, Ar-H)

14.1.4 ^{13}C NMR (d$_6$-DMSO, δ/ppm): 161.99 (3 × Ar-OH), 160.06 (3 × -NHCO-), 150.42 (6 × Ar-H), 146.16 (3 × -N=C-), 139.86 (3 × C, pyridyl), 121.38 (6 × Ar-H), 98.94 (3 × C, core)

14.1.5 IR (cm^{-1}): 2820, 1676, 1632, 1588, 1454, 1410, 1371, 1324, 1280, 1219, 1186, 1155, 1091, 1064, 997, 945, 892, 837, 781, 746, 682, 633, 557

14.1.6 MS: HRMS (ESI$^-$) calculated for [M-H]$^-$ 566.1542, $C_{21}H_{15}N_6O_6$ found: 566.1562

14.1.7 Melting point: Decomposes upon heating (>300 °C)

14.2 Gel C_e using ex situ prepared C_e:

A typical example of setting gel $\mathbf{C_e}$ using ex situ prepared $\mathbf{C_e}$ at 1 wt% is described. 0.1 g (0.16 mmol) of $\mathbf{C_e}$ was mixed with water (10 ml) to create a suspension. To this suspension NaOH (12 mg, 0.32 mmol) was added and the solution was well shaken until $\mathbf{C_e}$ had completely dissolved. Once dissolved **GdL** (85.51 mg, 0.48 mmol) was added to the solution which was shaken until the **GdL** had completely dissolved at which point the solution was allowed to stand. After 2 hours a red gel had formed. Gelation will occur over the optimum pH range 4-5.
Minimum gel concentration 0.2 wt%

14.3 Gel C_k using ex situ prepared C_e:

A typical example of setting gel $\mathbf{C_k}$ using ex situ prepared $\mathbf{C_e}$ 1 at 2 wt% is described. 0.2 g (0.32 mmol) of $\mathbf{C_e}$ was mixed with water (10 ml) to create a suspension. To this suspension NaOH (25 mg, 0.65 mmol) was added and the solution was well shaken until $\mathbf{C_e}$ had completely dissolved. At this point a further portion of NaOH (25 mg, 0.65 mmol) was added. This resulted in the formation of a yellow gel after approximately 4 hours. Gelation will occur over the optimum pH range 9.5-12.
Minimum gel concentration 0.6 wt%

14.4 Rheology of Gel C$_e$ set using ex situ prepared C$_e$:

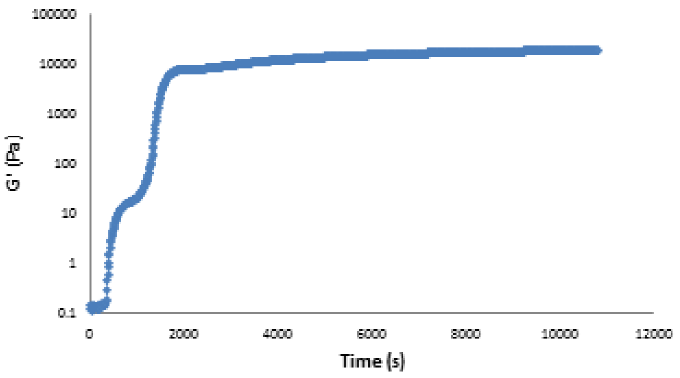

Figure S58. Time sweep rheometry of gel **C**$_e$ prepared using ex situ synthesised **C**$_e$. Storage modulus *G'* (Pa) (y-axis) plotted (log scale) against time (s) (x-axis).

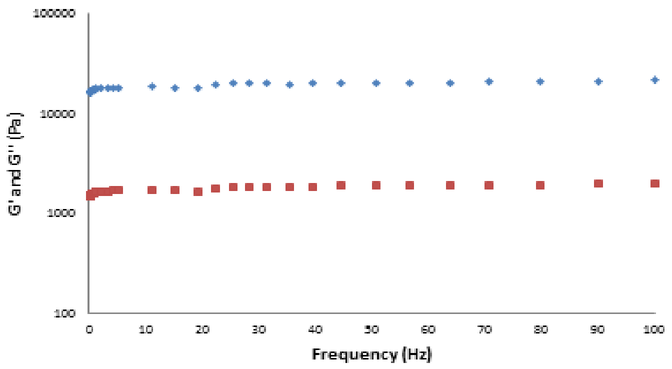

Figure S59. Frequency sweep rheometry of gel **C**$_e$ prepared using ex situ synthesised **C**$_e$. The storage modulus *G'* (Pa) (blue) and the loss modulus *G"* (Pa) (red) are shown as a log scale (y-axis) against the frequency (Hz) (x-axis).

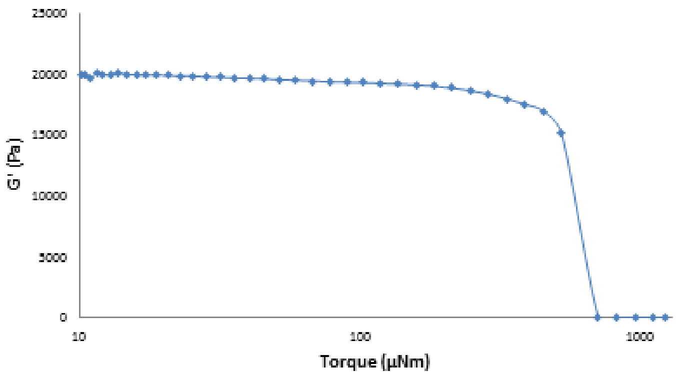

Figure S60. Amplitude sweep rheometry of gel **C**$_e$ prepared using ex situ synthesised **C**$_e$. The storage modulus *G′* (Pa) (y-axis) plotted against torque (μNm) (x-axis) shown in a log scale. A line between data points added to guide the eye.

It is worth noting the parity in the results for the **C**$_e$ gels prepared by both methods 2 and with ex situ synthesised **C**$_e$. Both sets of results are consistent in terms of the *G′* with respect to time in the time sweep. The values of *G′* and *G″* observed in the frequency sweep and the yield torque value obtained in the amplitude sweep experiments.

14.5 Chemical analysis of dried gel C_e set using ex situ prepared C_e:

14.5.1 1H NMR(d_6-DMSO, J/Hz, δ/ppm): 13.81 (broad s, 3H, Ar-OH), 12.48 (broad s, 3H, -NH), 8.95 (s, 3H, -CHN), 8.82 (s, 6H, Ar-H), 7.86 (s, 6H, Ar-H)

14.5.2 ^{13}C NMR (d_6-DMSO, δ/ppm): 161.78 ((1) 3 × Ar-OH), 160.01 ((2) 3 × -NHCO-), 150.83 ((3) 6 × Ar-H), 146.34 ((4) 3 × -N=C-), 140.01 ((5) 3 × C, pyridyl), 121.42 ((6) 6 × Ar-H), 98.99 ((7)3 × C, core)

14.5.3 IR: 2856, 1676, 1632, 1588, 1454, 1410, 1371, 1219, 1178, 1155, 1097, 1064, 997, 951, 896, 841, 781, 740, 688.

14.6.4 HRMS (ESI$^-$) calculated for $[M-H]^-$ 566.1542 $C_{27}H_{20}N_9O_6$ found 566.1523

14.7.5 Melting point**:** Decomposes upon heating (>300 °C)

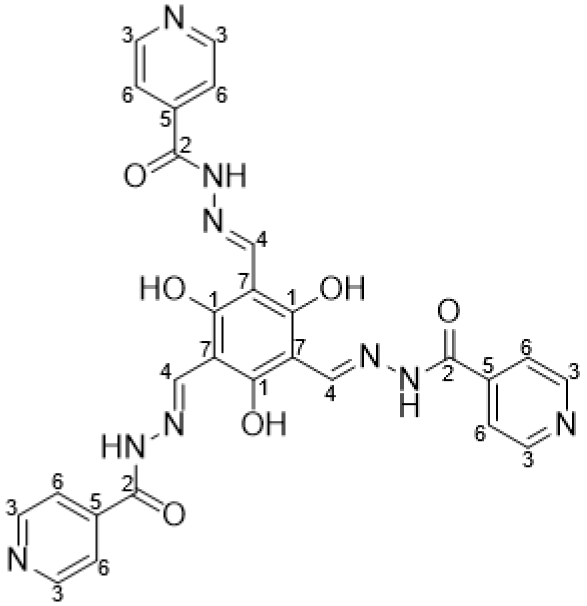

Figure S61. Chemical structure of dried product of gel C_e (N-[(E)-[2,4,6-trihydroxy-3,5-bis[(E)-(pyridine-4-carbonylhydrazono)methyl]phenyl]methyleneamino]pyridine-4-carboxamide) prepared using ex situ synthesised C_e with numerical labels relating the assignment of the ^{13}C NMR spectra.

The isolated products of the C_e gels prepared by both methods 2 and using ex situ prepared C_e are chemically identical.

14.6 Morphology of gel C_e prepared ex situ synthesised C_e determined by SEM

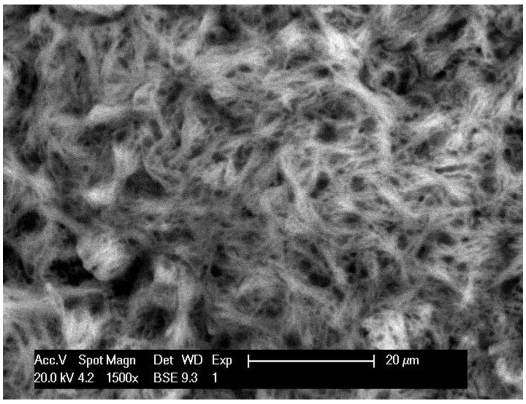

Figure S62. SEM images showing the fibrous nature of the gel **C_e** prepared using ex situ synthesised **C_e**.

14.7 Rheology of Gel $\mathbf{C_k}$ set using ex situ prepared $\mathbf{C_e}$:

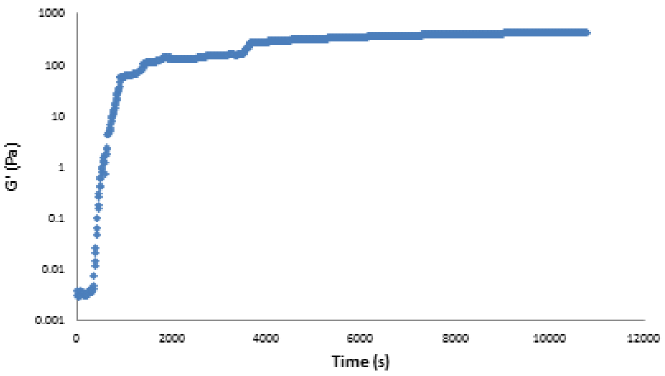

Figure S63. Time sweep rheometry of gel $\mathbf{C_k}$ prepared ex situ. Storage modulus *G'* (Pa) (y-axis) plotted (log scale) against time (s) (x-axis).

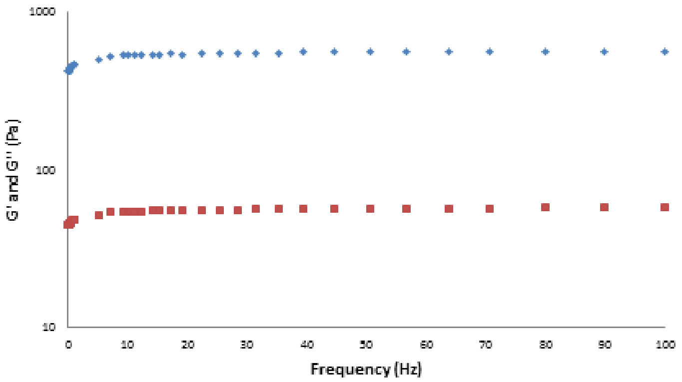

Figure S64. Frequency sweep rheometry of gel $\mathbf{C_k}$ prepared ex situ. The storage modulus *G'* (Pa) (blue) and the loss modulus *G"* (Pa) (red) are shown as a log scale (y-axis) against the frequency (Hz) (x-axis).

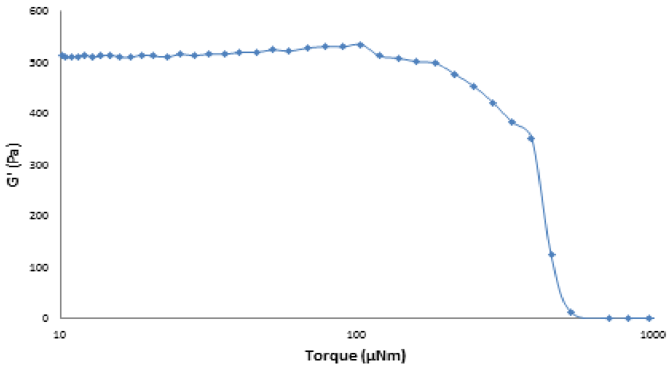

Figure S65. Amplitude sweep rheometry of gel $\mathbf{C_k}$ prepared ex situ. The storage modulus *G′*(Pa) (y-axis) plotted against torque (µNm) (x-axis) shown in a log scale. A line between data points added to guide the eye.

It is worth noting the parity in the results for the $\mathbf{C_k}$ gels produced by both methods 1 and with ex situ prepared $\mathbf{C_e}$. Both sets of results are consistent in terms of the G′with respect to time in the time sweep. The values of G′ and G″ observed in the frequency sweep and the yield torque value obtained in the amplitude sweep experiments.

14.8 Analysis of dried gel $\mathbf{C_k}$ prepared using ex situ synthesised $\mathbf{C_e}$:

14.8.1 ^{1}H NMR(d_6-DMSO, J/Hz, δ/ppm): 13.86 (dd, J = 12.99, 4.32, 3H, -CH-N$\underline{\text{H}}$-NH-), 13.72 (t, J = 13.15, 3H, -CH-N$\underline{\text{H}}$-NH-), 8.52 (s, 6H, Ar-H), 8.36 (dd, J = 13.00, 2.54, 3H, -CH-), 7.85 (m, 6H, Ar-H)

14.8.2 ^{13}C NMR (d_6-DMSO, δ/ppm): 183.43, 181.92, 181.92, 180.58 ((1)C=O); 162.52, 162.4, 162.35 ((2)C=O); 149.37 ((3) Ar-H); 147.21, 147.12 ((4) $\underline{\text{C}}$=CH); 145.28, 144.79, 144.69, 144.2 ((5) =CH-NH-); 121.88 ((6) Ar-H); 102.52, 102.35, 102.33 ((7) $\underline{\text{Ar}}$-CO-). For assignments see Fig. S31.

14.8.3 IR: 3188, 2162, 1623, 1589, 1428, 1276, 1147, 1057, 999, 878, 839, 750, 701, 688

14.8.4 Melting point: Decomposes upon heating (> 300^{o}C)

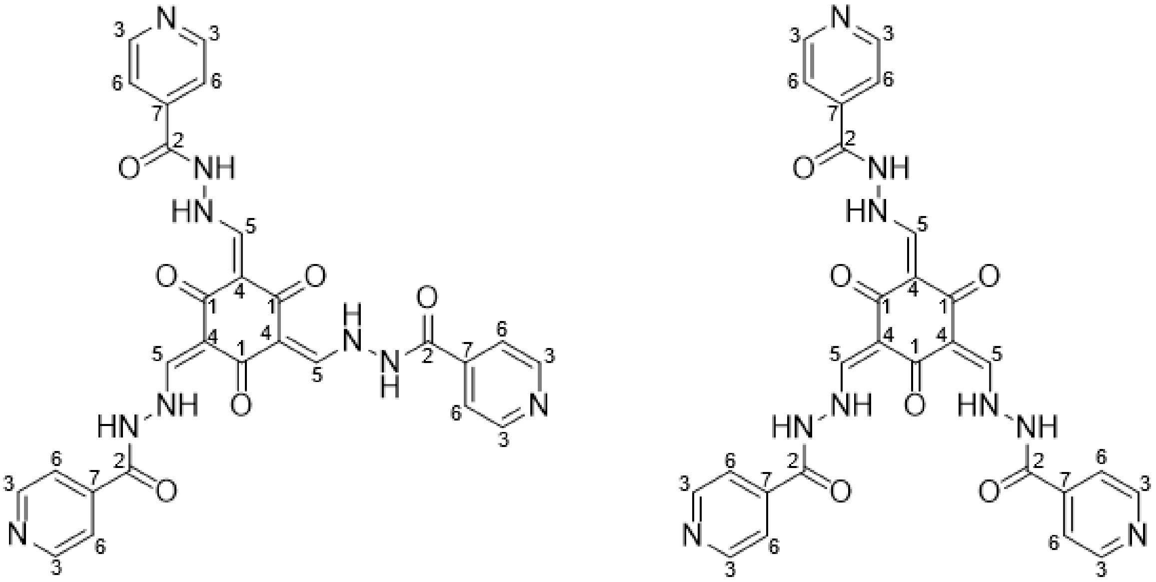

Figure S66. Chemical structure of dried product of gel $\mathbf{C_k}$ (N'-[[2,4,6-trioxo-3,5-bis[[2-(pyridine-4-carbonyl)hydrazino]methylene]cyclohexylidene]methyl]pyridine-4-carbohydrazide) prepared by using ex situ synthesised $\mathbf{C_e}$ showing the two structural conformations it adopts C_3 (right) and C_s (left) with numerical labels relating the assignment of the ^{13}C NMR spectra.

The isolated products the $\mathbf{C_k}$ gels prepared by both methods 1 and using ex situ prepared $\mathbf{C_e}$ are chemically identical.

14.9 Morphology of gel C_k prepared ex situ synthesised C_e determined by SEM

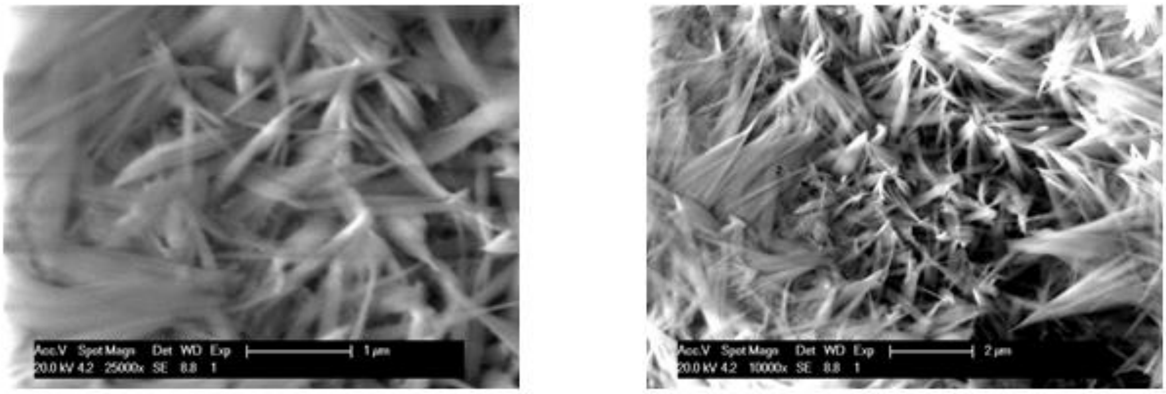

Figure S67. SEM images showing the fibrous nature of the gel $\mathbf{C_k}$ prepared using ex situ synthesised $\mathbf{C_e}$.

14.10 Ex situ preparation of gel B_e ex situ

From a sample of the gel $\mathbf{B_e}$ prepared by method 3 it is possible through drying of the gel compound to obtain an isolate of the gel $\mathbf{B_e}$. This isolated di-substituted species can be redissolved and used to set the gel $\mathbf{B_e}$ in the ex situ method outlined below

14.11 Gel B_e preparation ex situ (use of isolated B_e):

A typical example of setting gel $\mathbf{B_e}$ by method 5 at 1 wt% is described. A previously prepared sample of gel $\mathbf{B_e}$ prepared by method 2 had been dried by vacuum filtration and washed with water (5 × 100 ml) to produce a dull orange powder that was dried in the oven over night at 80 ^{o}C. This powder (0.1 g, 0.22 mmol) was mixed with water (10 ml) to create a suspension. To this suspension NaOH was added (3 mg, 0.08 mmol) once the solid had completely dissolved **GdL** (42.76 mg, 0.24 mmol) was added resulting in the formation of an orange gel after 1 hour. Gelation will occur over the optimum pH range 4-5.
Minimum gel concentration 0.3 wt%.

The dynamic character of the hydrazone bond does present some issues when using this methodology (which are also present in gelation method 1). Upon dissolving the compounds at pH 8 there is some rearrangement resulting in NMR and MS data showing the presence of small quantities of $\mathbf{\mathit{I}_e}$, ***II***, $\mathbf{A_e}$, $\mathbf{B_e}$ and $\mathbf{C_e}$ within the mixture. There is one dominant species in this mixture (> 90%), with the starting material being the significant majority species present in all cases studied. For example, if $\mathbf{B_e}$ is utilised then the majority of the species present is $\mathbf{B_e}$ and if $\mathbf{C_e}$ is the starting material then $\mathbf{C_e}$ is the significantly abundant species present.

14.12 Rheology gel B_e preparation using ex situ isolated B_e:

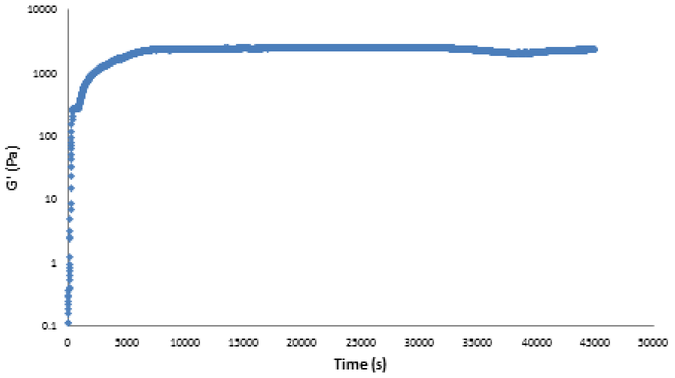

Figure S68. Time sweep rheometry of gel **B**$_e$ prepared using ex situ isolated **B**$_e$. Storage modulus *G'* (Pa) (y-axis) plotted (log scale) against time (s) (x-axis).

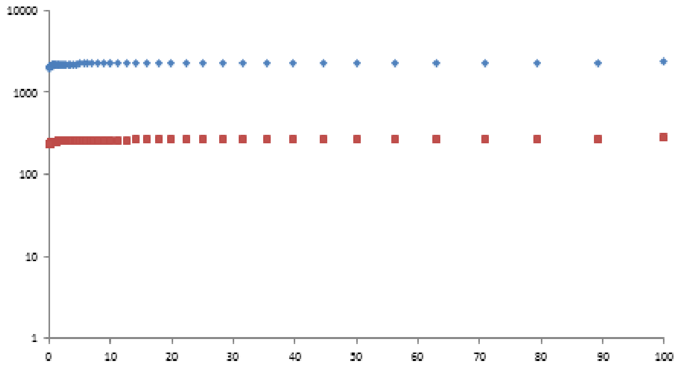

Figure S69. Frequency sweep rheometry of gel **B**$_e$ prepared using ex situ isolated **B**$_e$. The storage modulus *G'* (Pa) (blue) and the loss modulus *G"* (Pa) (red) are shown as a log scale (y-axis) against the frequency (Hz) (x-axis).

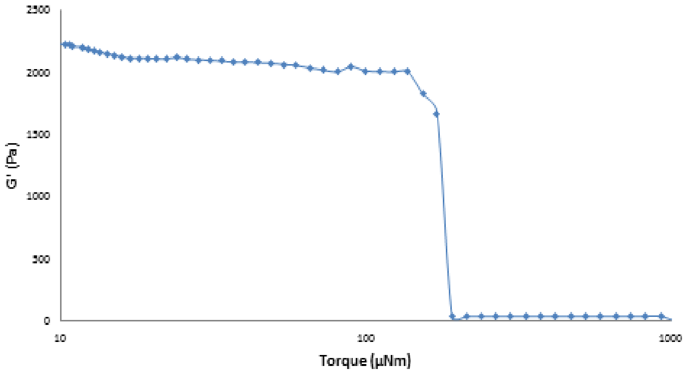

Figure S70. Amplitude sweep rheometry of gel **B**$_e$ prepared using ex situ isolated **B**$_e$. The storage modulus *G'* (Pa) (y-axis) plotted against torque (μNm) (x-axis) shown in a log scale. A line between data points added to guide the eye.

It is worth noting the parity in the results for the **B**$_e$ gels produced by both methods 3 and using ex situ isolated **B**$_e$. Both sets of results are consistent in terms of the G′ with respect to time in the time sweep. The values of G′ and G″ observed in the frequency sweep and the yield torque value obtained in the amplitude sweep experiments.

14.13 Analysis of gel B_e prepared using ex situ isolated B_e:

14.13.1 ^1H NMR(d_6-DMSO, J/Hz, δ/ppm): 13.73 (broad s, 3H, Ar-OH), 12.43 (broad s, 2H, -NH), 10.10 (s, 1H, -CHO), 8.80 (s, 2H, -CHN), 8.77 (d, 4H, Ar-H), 7.82 (d, 4H, Ar-H)

14.13.2 ^{13}C NMR (d_6-DMSO, δ/ppm): 192.21 ((1)-CHO), 167.7 ((2)Ar-OH), 166.73 ((3)2 × Ar-OH), 160.78 ((4) –NH-C=O), ((5) 150.61 (4 × Ar-H), 145.82 ((6) -N=C-), 139.73 ((7) C, pyridyl), 121.61 ((8)4 × Ar-H), 99.74 ((9) core C, imine) 99.01 ((10) core C, aldehyde)

14.13.3 IR: 3656, 2909, 2162, 1537, 1494, 1455, 1410, 1283, 1187, 1064, 998, 836, 790, 748, 681, 596

14.13.4 Melting point: Decomposes upon heating (>300 °C)

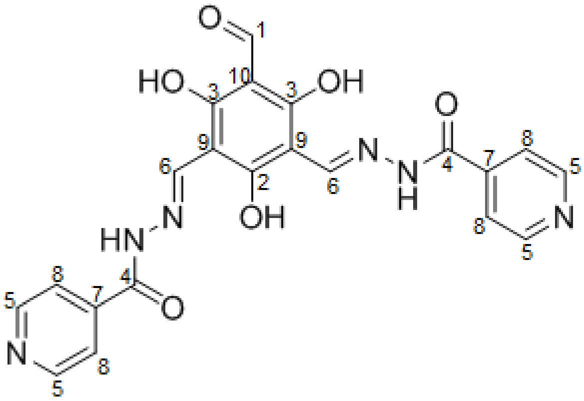

Figure S71. Chemical structure of dried product of gel $\mathbf{B_e}$ (N-[(E)-[3-formyl-2,4,6-trihydroxy-5-[(E)-(pyridine-4-carbonylhydrazono)methyl]phenyl]methyleneamino]pyridine-4-carboxamide) prepared by method 5 with numerical labels relating the assignment of the ^{13}C NMR spectra.

The isolated products of the $\mathbf{B_e}$ gels prepared by both methods 3 and with ex situ isolated $\mathbf{B_e}$ are chemically identical.

14.14 Morphology of gel B_e prepared using ex situ isolated B_e determined by SEM

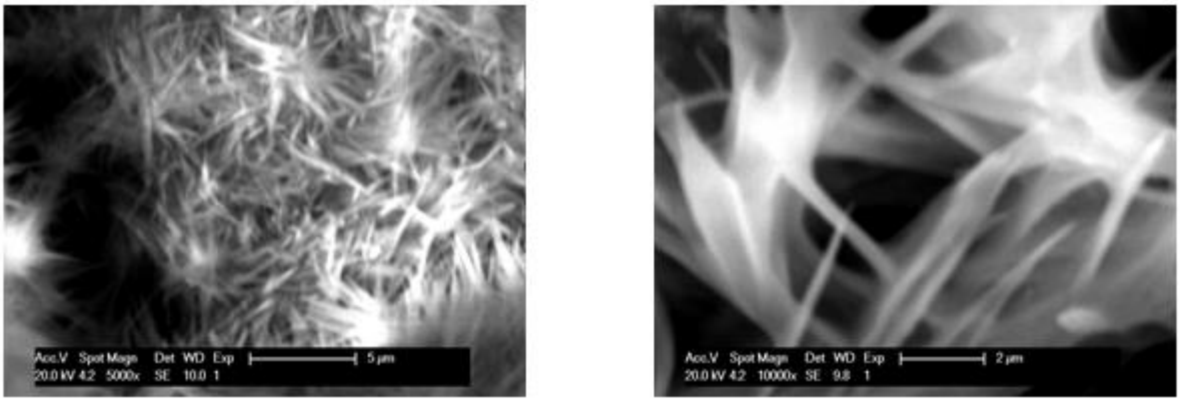

Figure S72. SEM images showing the fibrous nature of the gel $\mathbf{B_e}$ prepared using ex situ isolated $\mathbf{B_e}$.

14.15 Powder X-ray Diffraction data for dried gel samples

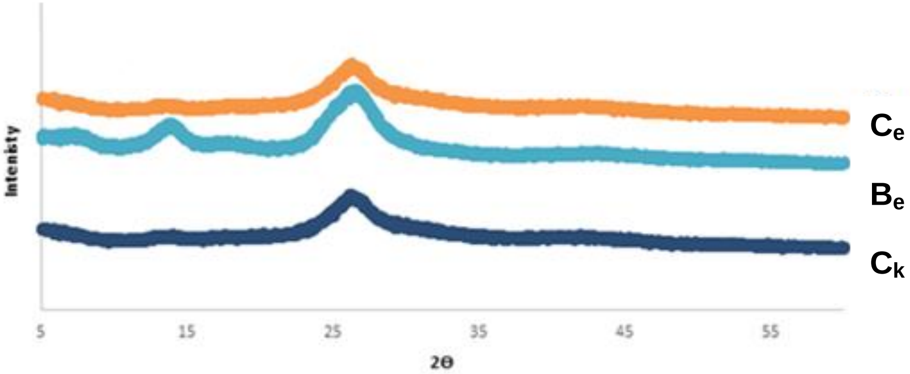

Figure S73. Powder X-Ray Diffraction patterns for each gel produced by each ex situ approach.

15.0 Avrami constant and fractal dimension determination.

The Avrami coefficient (n) could be determined by plotting ln(-ln(1-X)), where X = $(G'_t - G'_0)/(G'_\infty - G'_0)$ ($G'_t = G'$ at time t, $G'_0 = G'$ at time = 0, $G'_\infty = G'$ average of last 5 data points) against ln(t – t_0). The Avrami constant is the first part of the slope where the nucleation process begins.

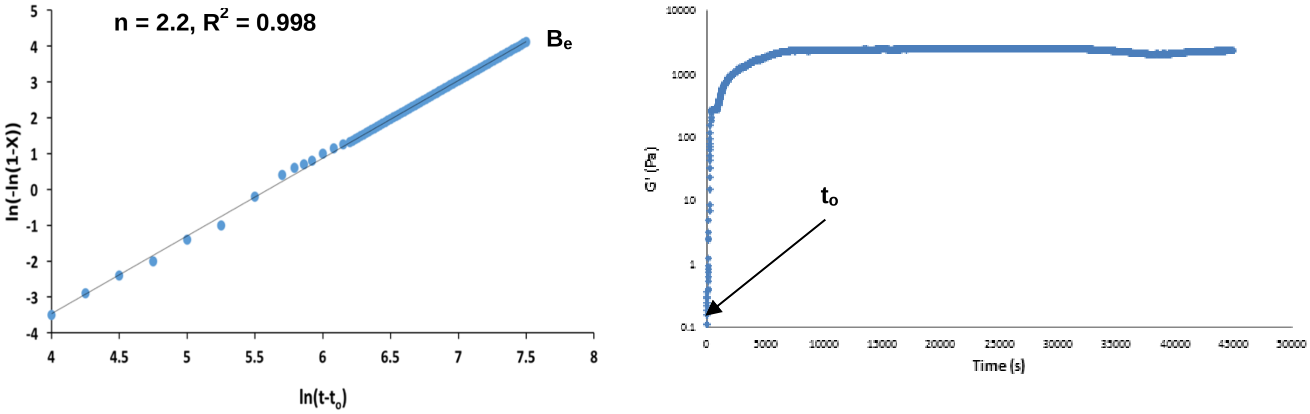

Figure S74. Time sweep rheology experiment (right) and the derived Avrami plot (left) of gel **B$_e$** (method 6).

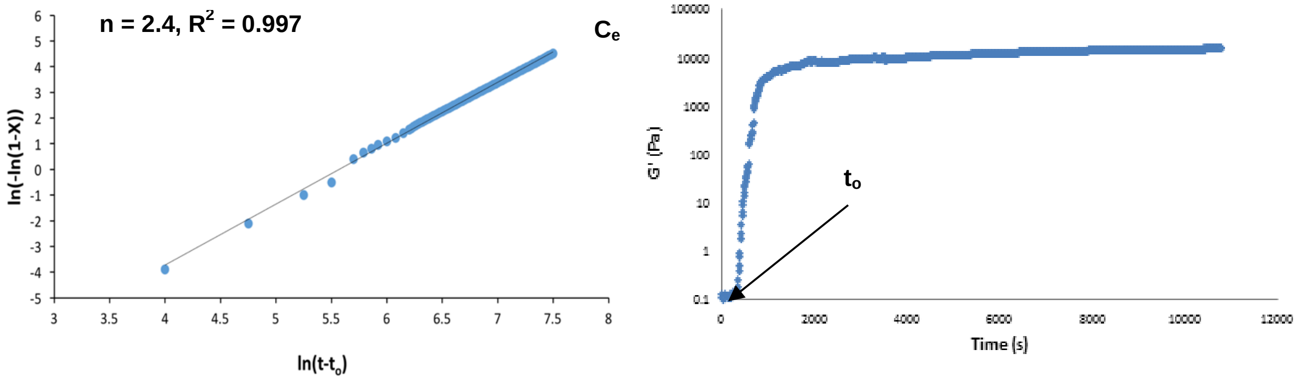

Figure S75. Time sweep rheology experiment (right) and the derived Avrami plot (left) of gel **C$_e$** (method 4).

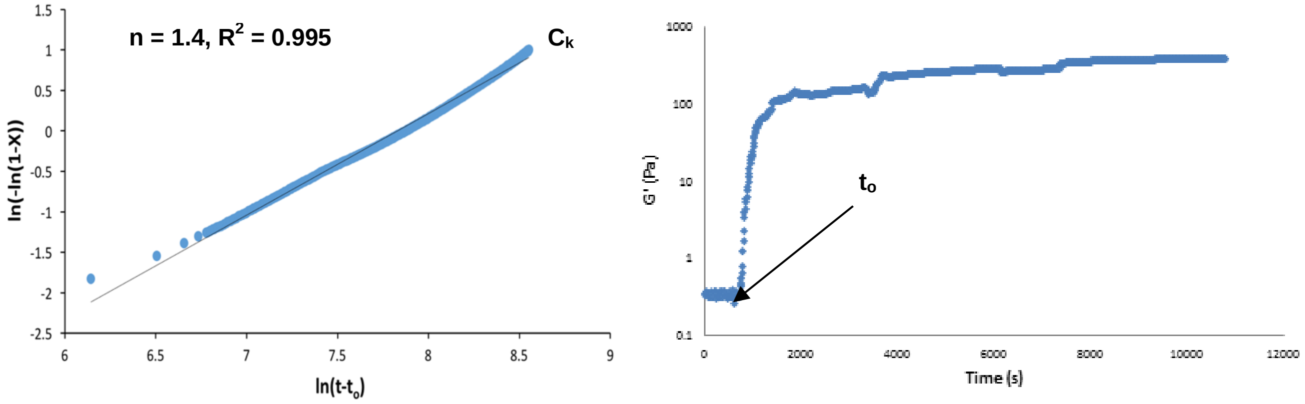

Figure S76. Time sweep rheology experiment (right) and the derived Avrami plot (left) of gel **C$_k$** (method 5).

Concentration study of gels **C$_e$** and **B$_e$** where used to study the fit of the gelation process with the cellular solid model which predicts a relation of $G' \propto [\mathrm{conc}]^2$, both gels show good correlation with this model.[6]

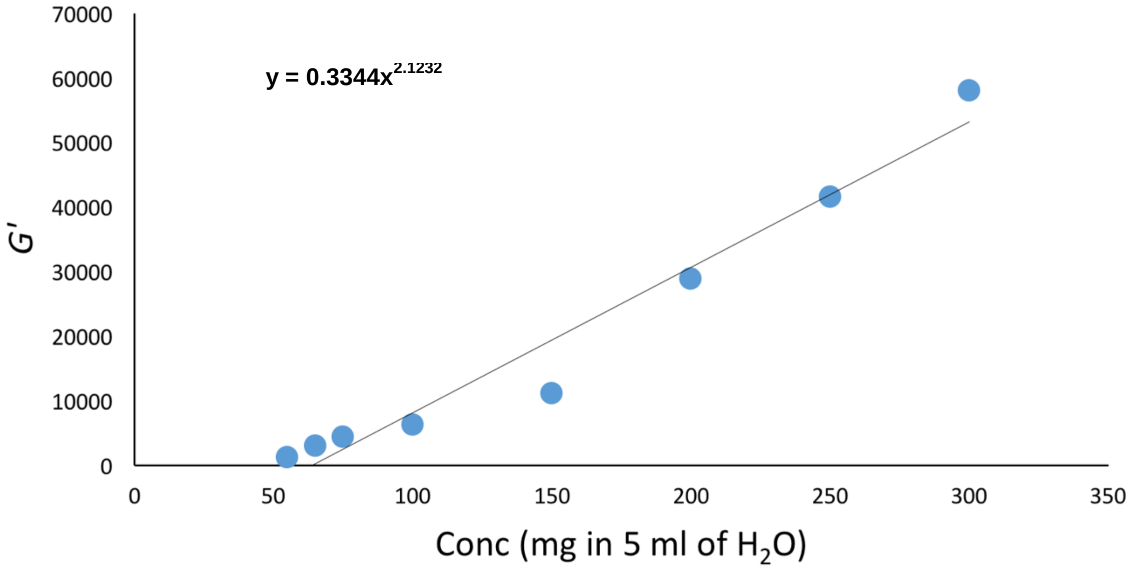

Figure S77. Gel **C$_e$** concentration study (prepared using ex situ synthesised **C$_e$**) showing $G' \propto [\mathrm{conc}]^{2.12}$.

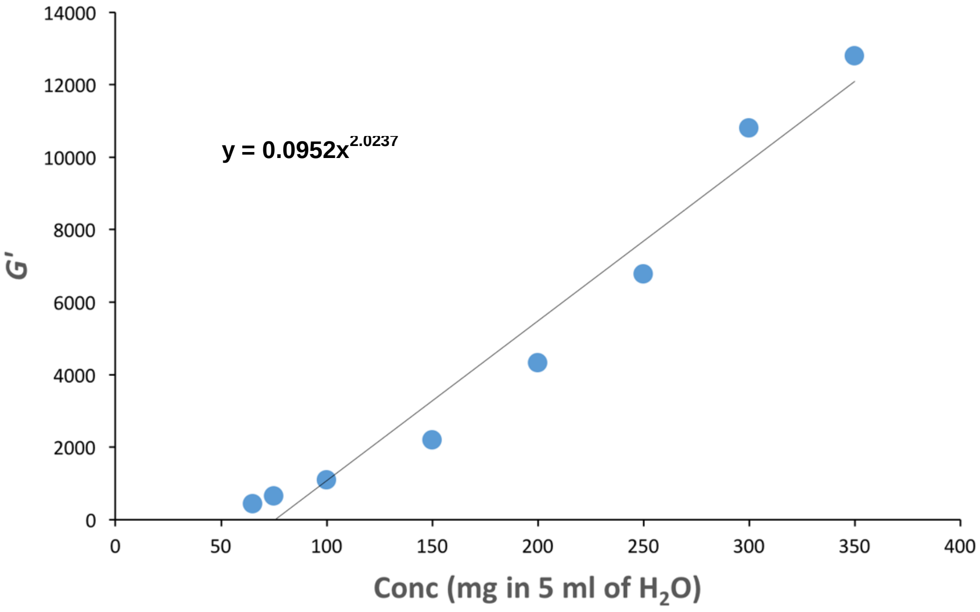

Figure S78. Gel **C$_e$** concentration study (prepared using using ex situ synthesised **C$_e$**) showing $G' \propto [\mathrm{conc}]^{2.02}$.

16.0 Thermodynamic Stabilities of gels B_e, C_e and C_k

Although the field generally consider gels to be kinetic states and not global thermodynamic minimum states, these gels have shown themselves to be thermodynamically stable well beyond the range of any practical experimental timescale.

Figure S79. Gel $\mathbf{B_e}$ prepared by method 3 (left) and gel $\mathbf{C_e}$ prepared by method 2 (right) photographed 380 days after preparation at the time of writing.

Figure S80. Gel $\mathbf{C_k}$ prepared by method 1 photographed 372 days after preparation at the time of writing.

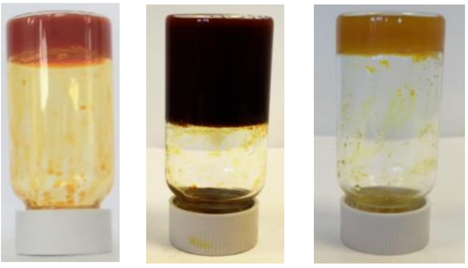

Figure S81. Gel $\mathbf{B_e}$ (left), Gel $\mathbf{C_e}$ (centre) and gel $\mathbf{C_k}$ (right). Photograph taken after gels had been heated to 90 ^{o}C in an oil and held at this elevated temperature for 2 hours.

17.0 Non-gelator compounds D_e and D_k

17.1 Synthesis of D_e:

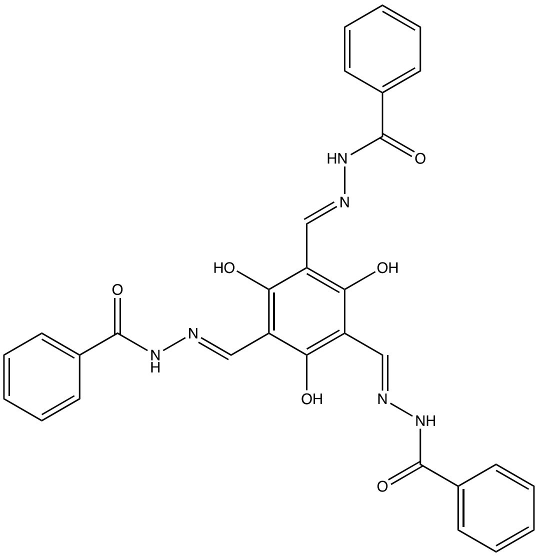

Figure S82. *N'*,*N'''*,*N'''''*-((1*E*,1'*E*,1''*E*)-(2,4,6-trihydroxybenzene-1,3,5-triyl)tris(methanylylidene))tri(benzohydrazide) (**D_e**).

To a mixture of 1,3,5-triformylphloroglucinol (0.25 g, 1.19 mmol, 1 equiv.) and isonicotinc acid hydrazide (0.50 g 3.69 mmol, 3.1 equiv.) ethanol (50 ml) was added. The resulting suspension was brought to reflux and the reaction was allowed to proceed for 4 hours to produce a bright yellow suspension. This was then allowed to cool to room temperature before being filtered to yield a yellow solid. This solid was then washed with water (4 × 50 ml) before being collected and dried in an oven overnight (80^{o}C) to yield the final product.

17.1.1 Yield: 89 %, 0.62 g (M.W. 564.18 gmol^{-1}).

17.1.2 ^{1}H NMR (d_6-DMSO, J/Hz, δ/ppm): 13.95 (s, 3H, Ar-OH), 12.29 (s, 3H, -NH-), 8.97 (s, 3H, -CHN), 7.97 (d, J = 7.10, 6H, Ar-H), 7.61 (m, 9H, Ar-H).

17.1.4 ^{13}C NMR (d_6-DMSO, δ/ppm): 162.88 (3 × Ar-OH), 162.20 (3 × -NHCO-), 145.57 (3 x N=CH-), 132.87 (3 x Ar-H), 132.56 (3 x Ar), 129.09 (6 x Ar-H), 128.01 (6 x Ar-H), 99.57 (3 x Ar).

17.1.5 IR (cm^{-1}): 3227, 3057, 1645, 1601, 1580, 1529, 1489, 1455, 1398, 1371, 1328, 1277, 1185, 1155, 1100, 1027, 1001, 958, 928, 900, 883, 815, 795, 776, 705, 686, 678, 620, 606, 595, 583, 571, 559.

17.1.6 MS HRMS (ESI$^-$): calculated for $[M-H]^-$ 563.1452, $C_{30}H_{23}N_6O_6$ found: 563.1443.

17.1.8 Melting point: Decomposes upon heating (>300 ^{o}C).

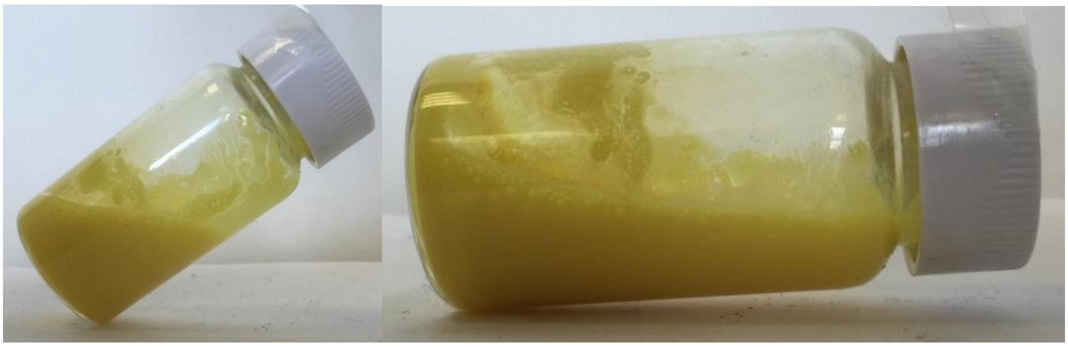

Figure S83. Photographs showing **D$_e$** after being dissolved at pH 8.5 and the addition of **GdL.** Note that a gel does not form when compared to the same procedure applied to the pyridyl appended **C$_e$**.

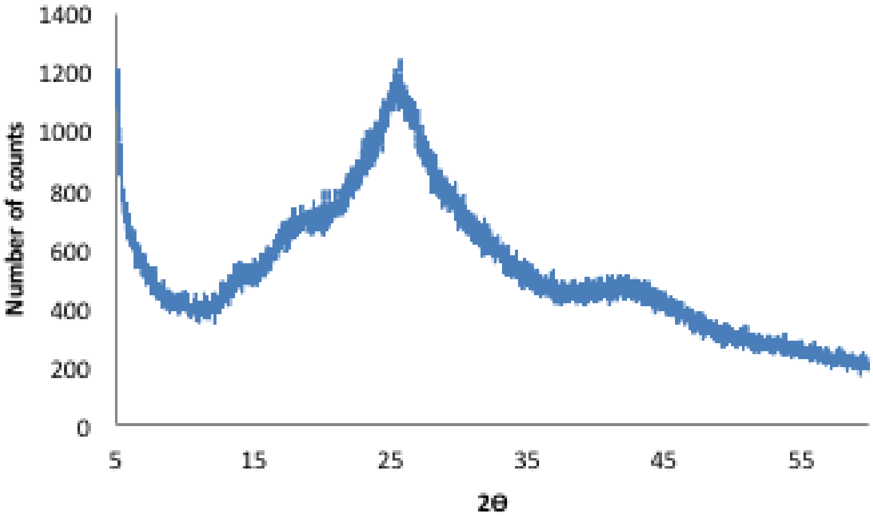

Figure S84. Powder X-Ray Diffraction pattern for **D$_e$** dissolved at pH 8 and precipitated with **GdL**. The peak at ~ 26 ° is typical of face to face π-π stacking for these molecules however the formation of a precipitate and not a gel implies the N of the pyridyl appended species **C$_e$** is essential for inter fibre cross-linking and gel formation.

^{1}H NMR for D$_e$ (d_6-DMSO, J/Hz, δ/ppm): 13.97 (s, 3H, Ar-OH), 12.24 (s, 3H, -NH-), 8.92 (s, 3H, -CHN), 7.96 (d, J = 7.07, 6H, Ar-H), 7.59 (m, 9H, Ar-H).

Figure S85. Photographs showing $\mathbf{D_k}$ after being dissolved at pH 8.5 and the pH subsequently raised to 10**.** Note that a gel does not form when compared to the same procedure applied to the pyridyl appended $\mathbf{C_k}$.

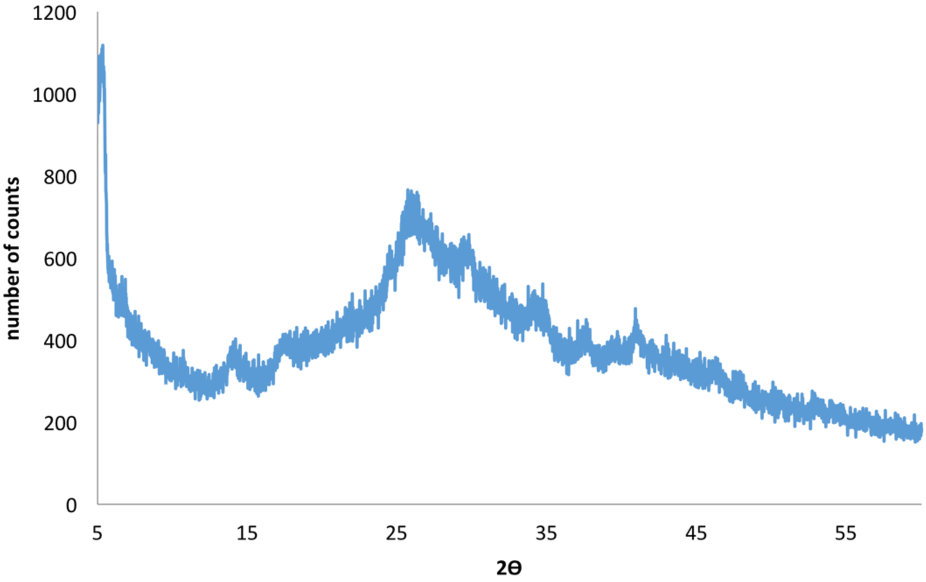

Figure S86. Powder X-Ray Diffraction patterns for $\mathbf{D_k}$ dissolved at pH 8 and precipitated with **NaOH**. The peak at ~ 26 ° is typical of face to face π-π stacking for these molecules however the formation of a precipitate and not a gel implies the N of the pyridyl appended species $\mathbf{C_k}$ is essential for inter fibre cross-linking and gel formation.

^{1}H NMR for $\mathbf{D_k}$ (d_6-DMSO, J/Hz, δ/ppm): 13.78 (dd, J = 12.23, 4.21, 3H, -CH-N<u>H</u>-NH-), 13.61 (t, J = 13.24, 3H, -CH-N<u>H</u>-NH-), 8.52 (s, 6H, Ar-H), 8.21 (dd, J = 13.10, 2.41, 3H, -CH-), 7.71 (m, 9H, Ar-H).

In both examples, i.e high pH and low pH precipitation $\mathbf{D_e}$ and $\mathbf{D_k}$ were characterised by PXRD and ^{1}H NMR. These compounds demonstrated the same pH controlled tautomerisation process as $\mathbf{C_e}$ and $\mathbf{C_k}$ but in both cases failed to form gels

18.0 Crystallography

Crystallographic data.

Crystal data for **C$_e$**.3DMSO: _chemical_formula_moiety $C_{27}H_{21}N_9O_6$,3(C_2H_6OS), M = 801.93, clear_pale_yellow needle, 0.210 × 0.010 × 0.005 mm^3, trigonal, space group $P31c$ (No. 159), $a = b$ = 18.241(2), c = 6.5002(16) Å, V = 1873.1(6) Å^3, Z = 2, D_c = 1.422 g/cm^3, F_{000} = 840, Oxford Diffraction SuperNova, Cu Kα radiation, λ = 1.54180 Å, T = 150K, $2\theta_{max}$ = 160.2°, 11882 reflections collected, 2410 unique (R_{int} = 0.089). Final $GooF$ = 0.9566, $R1$ = 0.0601, $wR2$ = 0.1528, R indices based on 1821 reflections with I I>2.0(I) (refinement on F^2), 167 parameters, 4 restraints. Lp and absorption corrections applied, μ = 2.370 mm^{-1}. Absolute structure parameter = -0.05(4) (Flack, H. D. *Acta Cryst*. **1983**, *A39*, 876-881).

Crystal data for **D$_e$**.MeOH: _chemical_formula_moiety $C_{30}H_{24}N_6O_6$,CH_4O, M = 596.60, clear_intense_orange block, 0.38 × 0.26 × 0.14 mm^3, triclinic, space group P-1 (No. 2), a = 13.8028(5), b = 15.1095(5), c = 15.4786(5) Å, α = 70.541(3), β = 66.375(3), γ = 88.032(3)°, V = 2770.19(19) Å^3, Z = 4, D_c = 1.430 g/cm^3, F_{000} = 1248, Oxford Diffraction SuperNova, Cu Kα radiation, λ = 1.54180 Å, T = 150K, $2\theta_{max}$ = 152.7°, 30191 reflections collected, 11480 unique (R_{int} = 0.025). Final $GooF$ = 0.9988, $R1$ = 0.0401, $wR2$ = 0.1068, R indices based on 10607 reflections with I I>2.0(I) (refinement on F^2), 835 parameters, 26 restraints. Lp and absorption corrections applied, μ = 0.862 mm^{-1}.

Description of the structures.

C$_e$.3DMSO

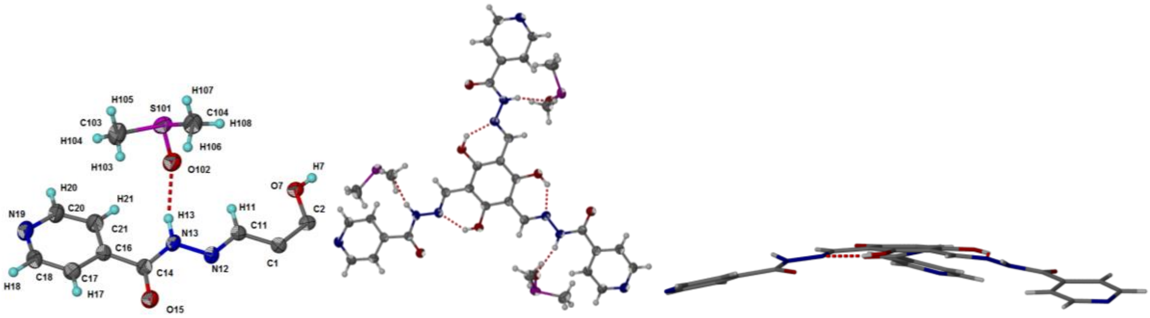

Figure S87. Asymmetric unit of the structure of **C$_e$** showing labels of atoms with atoms shown as ellipsoids at 50% probability. Complete molecule of **C$_e$** showing the hydrogen bonding between the OH groups and hydrazone groups as well as those between the DMSO molecules and **C$_e$**. Finally the flatness of the **C$_e$** molecules is highlighted with the right-hand image.

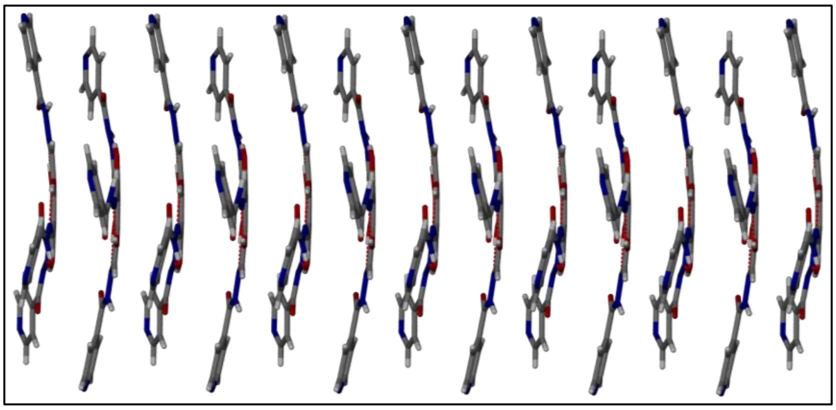

Figure S88. Stacking of **C$_e$** into one dimensional arrays (supramolecular polymers). π- π interactions between the pydridyl groups clearly seen as well as the concave:convex fit between the molecules allowing for a significant collection of weak supramolecular interactions (dispersion forces such as van der Waal's interactions) to form as described by Donald Cram's seminal work on supramolecular complexes. Structure viewed diagonal to the *c* axis.

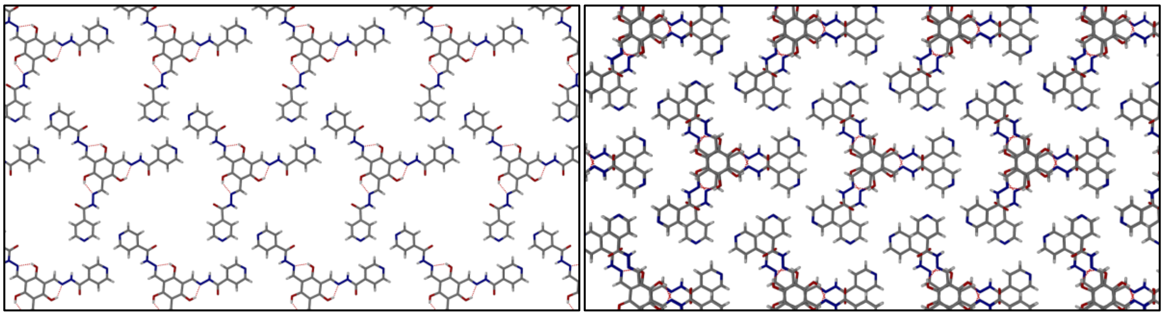

Figure S89. Packing of **C$_e$** in two-dimensional arrays that are related to each other through the *c* screw axis. DMSO molecules are not shown for clarity. Structure viewed down the *c* axis.

D$_e$.MeOH

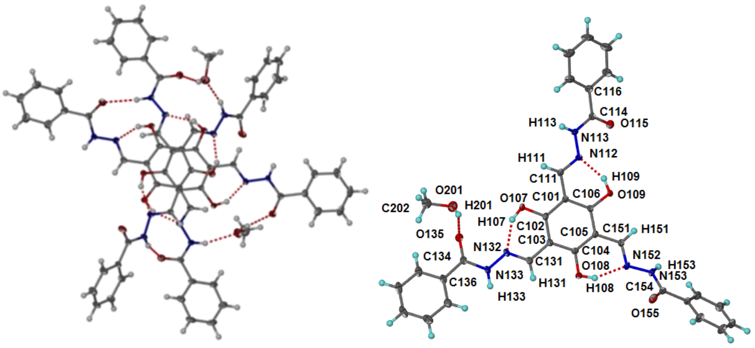

Figure S90. Asymmetric unit of the **D$_e$**.MeOH structure. Atoms shown as ellipsoids at 50% probability.

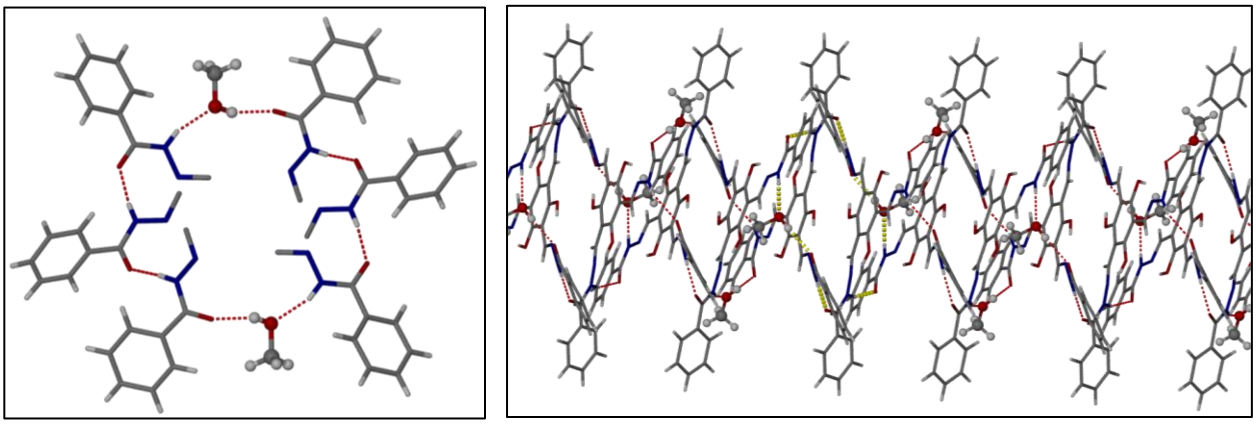

Figure S91. Stacking of **D$_e$** into one-dimensional columns through hydrogen bonding involving a discrete $R28_8^8$ hydrogen bonding patterns between four **D$_e$** molecules and two MeOH molecules (one shown with yellow hydrogen bonds to highlight ring hydrogen bond pattern). MeOH molecules show in ball-and-stick representation to highlight them.

Comparison of enol structures with published keto tautomers.

There are twelve published structures in the CSD for the keto tautomers of the family of compounds of interest to this publication. There are none of the enol tautomers. We therefore compared the two enol compounds structurally with these keto forms statistically. The bond distance between the carbon and oxygen (bond 1 in figure below) in the keto forms show a mean average of 1.252 Å (SD 0.034) while the included two structures have bond distances for $\mathbf{C_e}$ C2 . O7 . 1.347(5) Å and for $\mathbf{D_e}$ C2 . O7 . 1.3363(14) Å, C4 . O8 . 1.3432(14) Å, C6 . O9 . 1.3436(15) Å; C102 . O107 . 1.3430(14) Å, C106 . O109 . 1.3368(14) Å, C104 . O108 . 1.3462(14) Å. The bond distances for the six membered carbon rings (bond 4 below) are averaged as 1.449 Å (SD 0.019) for the keto forms and for $\mathbf{C_e}$ C1 . C2 . 1.409(6) Å and $\mathbf{D_e}$ C104 . C105 . 1.4016(16) Å, C101 . C102 . 1.4056(16) Å, C101 . C106 . 1.4119(16) Å, C102 . C103 . 1.4099(17) Å, C103 . C104 . 1.4067(16) Å, C105 . C106 . 1.4066(16) Å; C1 . C2 . 1.4069(17) Å, C1 . C6 . 1.4023(17) Å, C2 . C3 . 1.4135(16) Å, C3 . C4 . 1.4087(16) Å, C4 . C5 . 1.4070(17) Å, C5 . C6 . 1.4071(17). The bond distance between the carbon and nitrogen on the side arms (bond 2 below) are for the keto compounds averaging 1.377 Å (SD 0.02) and for $\mathbf{C_e}$ C11 . N12 . 1.292(6) Å and $\mathbf{D_e}$ C31 . N32 . 1.2837(16) Å, C51 . N52 . 1.2866(16) Å, C11 . N12 . 1.2856(17) Å; C131 . N132 . 1.2821(16) Å, C111 . N112 . 1.2845(16) Å, C151 . N152 . 1.2850(16) Å. The final bond distance to highlight is the carbon carbon bond between the five-membered ring and arm units (bond number 3 below). In the published keto structures they average 1.376 Å (SD 0.026) while in $\mathbf{C_e}$ they are C1 . C11 . 1.434(6) Å and $\mathbf{D_e}$ they are C1 . C11 . 1.4440(16) Å, C3 . C31 . 1.4519(17) Å, C5 . C51 . 1.4447(16) Å; C103 . C131 . 1.4499(16) Å, C105 . C151 . 1.4489(15) Å, C101 . C111 . 1.4492(16) Å. These bond distances clearly show our structures are indeed in the enol tautomer form.

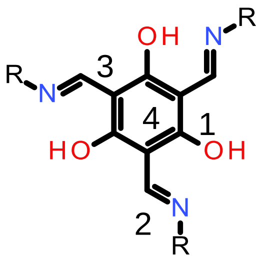

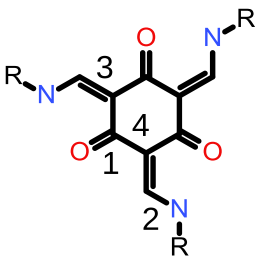

References

1. a) J. H. Chong, M. Sauer, B. O. Patrick, M. J. MacLachlan, *Org. Lett.* **2003**, *5*, 3823-3826 b) Y. Dai, T. J. Katz, *J. Org. Chem.* **1997**, *62*, 1274-1285
2. Gaussian 09, Revision **D.01**, M. J. Frisch, G. W. Trucks, H. B. Schlegel, G. E. Scuseria, M. A. Robb, J. R. Cheeseman, G. Scalmani, V. Barone, B. Mennucci, G. A. Petersson, H. Nakatsuji, M. Caricato, X. Li, H. P. Hratchian, A. F. Izmaylov, J. Bloino, G. Zheng, J. L. Sonnenberg, M. Hada, M. Ehara, K. Toyota, R. Fukuda, J. Hasegawa, M. Ishida, T. Nakajima, Y. Honda, O. Kitao, H. Nakai, T. Vreven, J. A. Montgomery, Jr., J. E. Peralta, F. Ogliaro, M. Bearpark, J. J. Heyd, E. Brothers, K. N. Kudin, V. N. Staroverov, R. Kobayashi, J. Normand, K. Raghavachari, A. Rendell, J. C. Burant, S. S. Iyengar, J. Tomasi, M. Cossi, N. Rega, J. M. Millam, M. Klene, J. E. Knox, J. B. Cross, V. Bakken, C. Adamo, J. Jaramillo, R. Gomperts, R. E. Stratmann, O. Yazyev, A. J. Austin, R. Cammi, C. Pomelli, J. W. Ochterski, R. L. Martin, K. Morokuma, V. G. Zakrzewski, G. A. Voth, P. Salvador, J. J. Dannenberg, S. Dapprich, A. D. Daniels, Ö. Farkas, J. B. Foresman, J. V. Ortiz, J. Cioslowski, and D. J. Fox, Gaussian, Inc., Wallingford CT, 2009.
3. A. V. Marenich, C. J. Cramer, and D. G. Truhlar, *J. Phys. Chem. B* **2009**, *113* 6378.
4. C. V. Yelamaggad, A. S. Achalkumar, D. S. Shankar Rao, S. K. Prasad, *J. Am. Chem. Soc.* **2004**, *126*, 6506-6507.
5. C Colguhoun, E. R. Draper, E. G. B. Eden, B. N. Cattoz, K. L. Morris, L. Chen, T. O. McDonald, A. E. Terry, P. C. Griffith, L. C. Serpell, D. J. Adams, *Nanoscale* **2010**, *6*, 13719-13725.
6. G. A. Buxton, N Clarke, *Phys. Rev. Lett.,* **2007**, **98**, 238103.

19.0 NMR and IR spectra

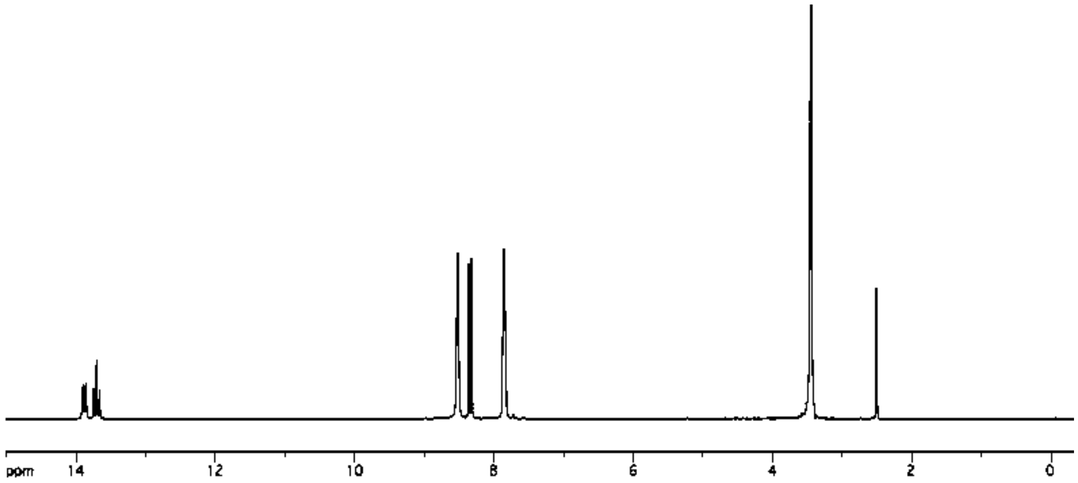

Figure S92. ^{1}H NMR spectra for C_k isolated from a gel produced using method 1.

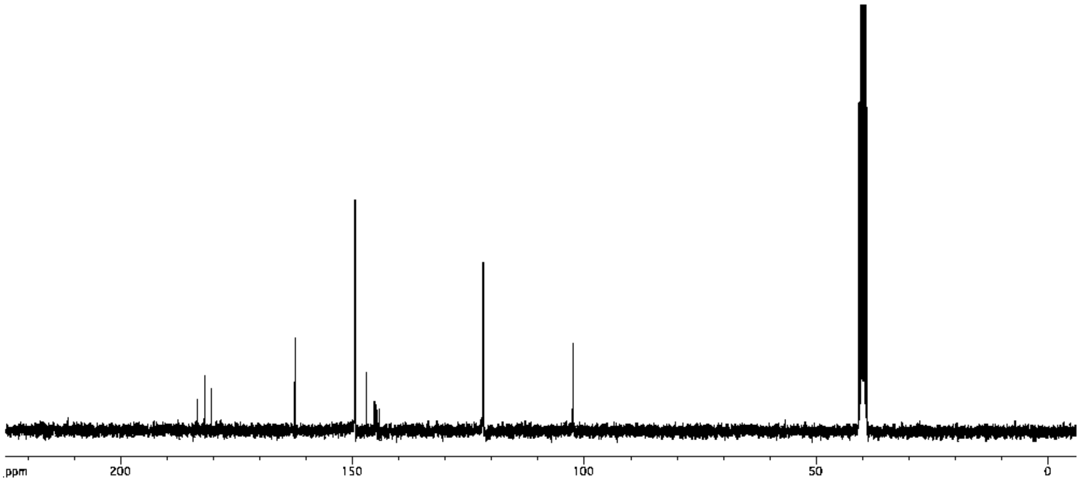

Figure S93. ^{13}C NMR spectra for C_k isolated from a gel produced using method 1.

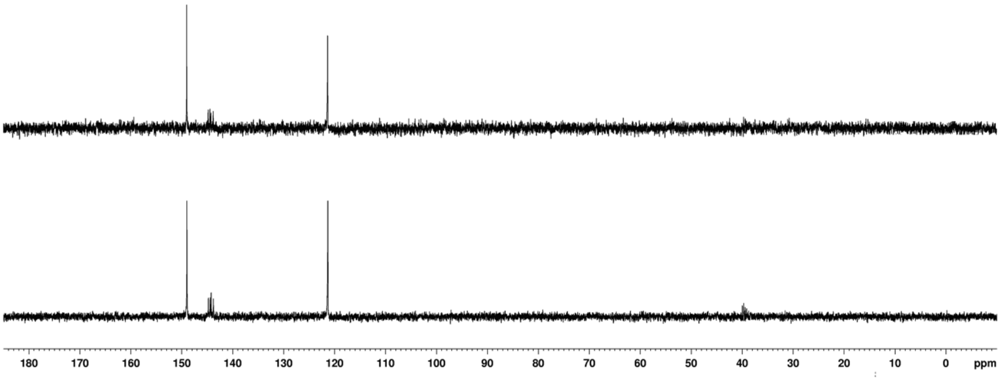

Figure S94. ^{13}C DEPT for C_k isolated from a gel produced using method 1.

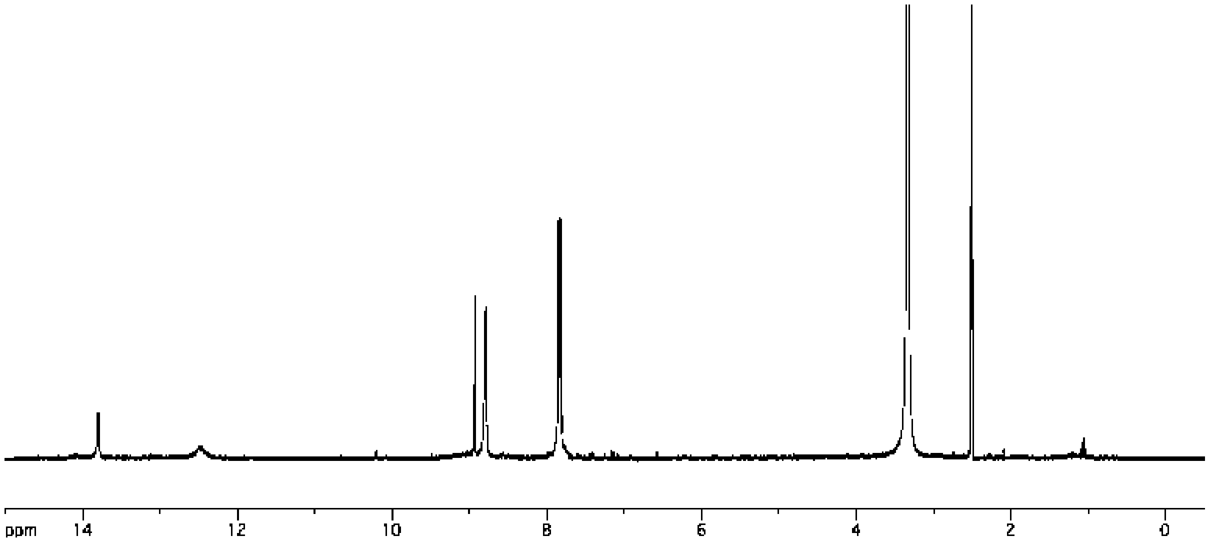

Figure S95. ^{1}H NMR spectra for C_e isolated from a gel produced using method 2.

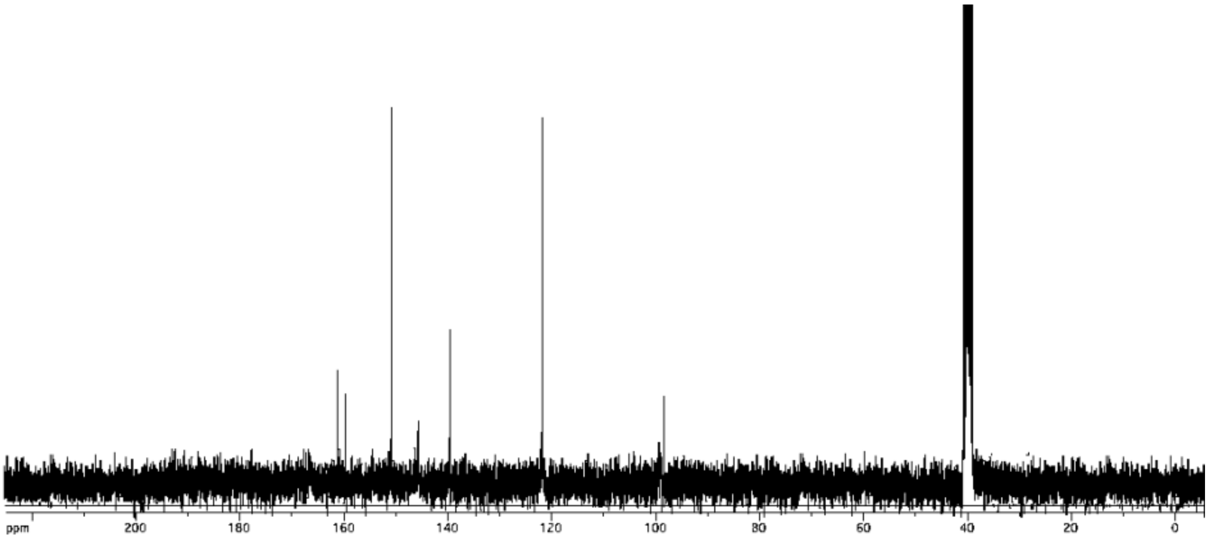

Figure S96. ^{13}C NMR spectra for C_e isolated from a gel produced using method 2.

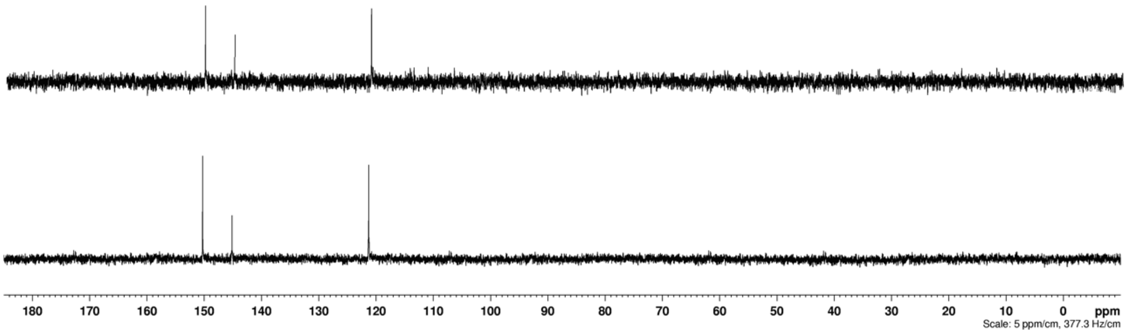

Figure S97. ^{13}C DEPT for C_e isolated from a gel produced using method 2.

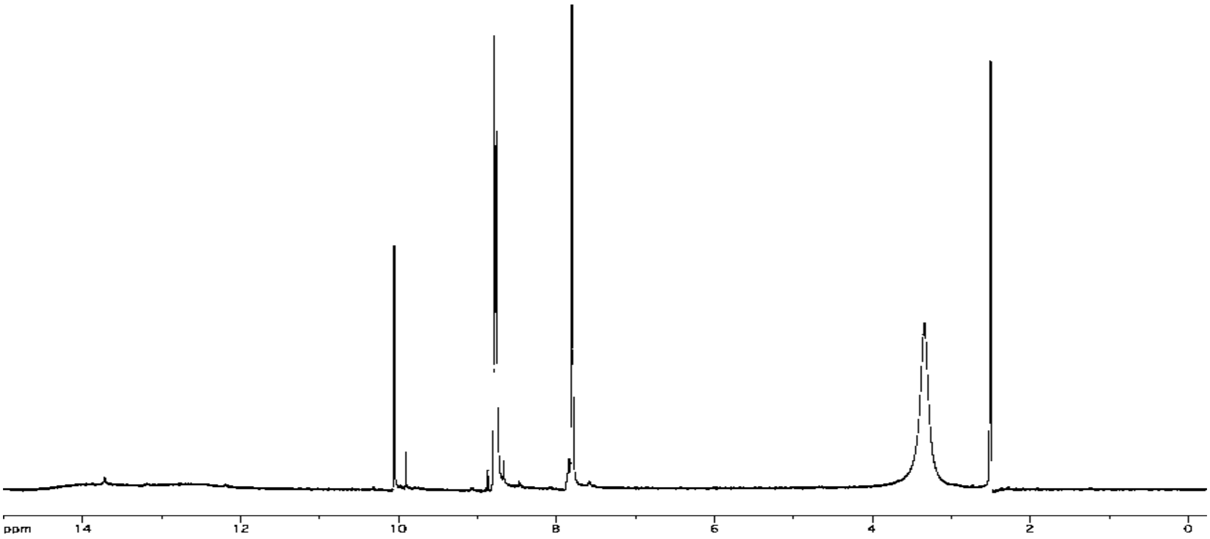

Figure S98. ^{1}H NMR spectra for B_e isolated from a gel produced using method 3.

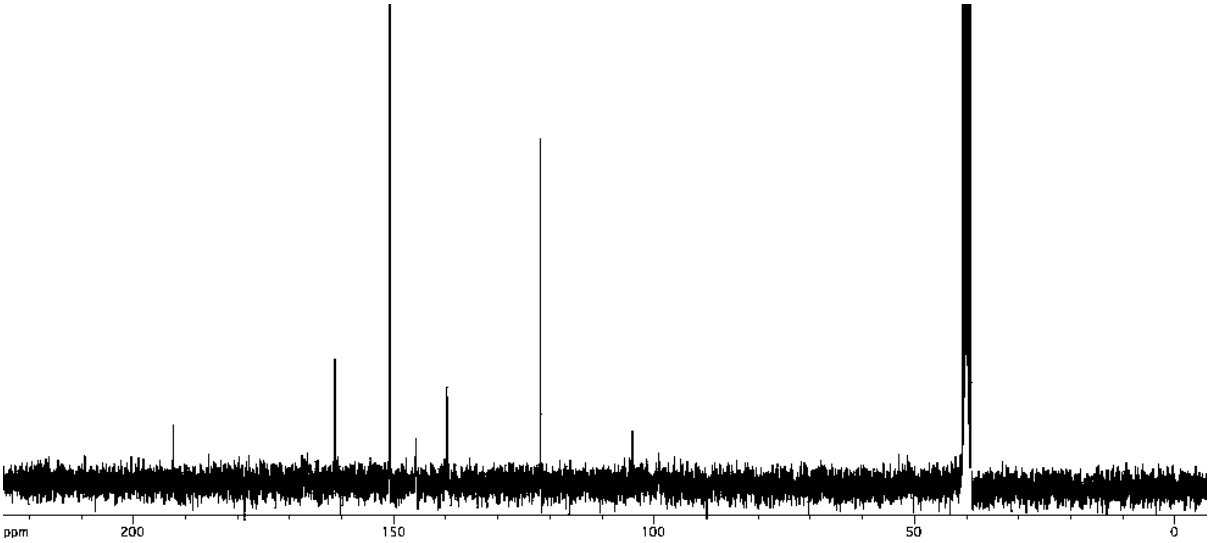

Figure S99. ^{13}C NMR spectra for B_e isolated from a gel produced using method 3.

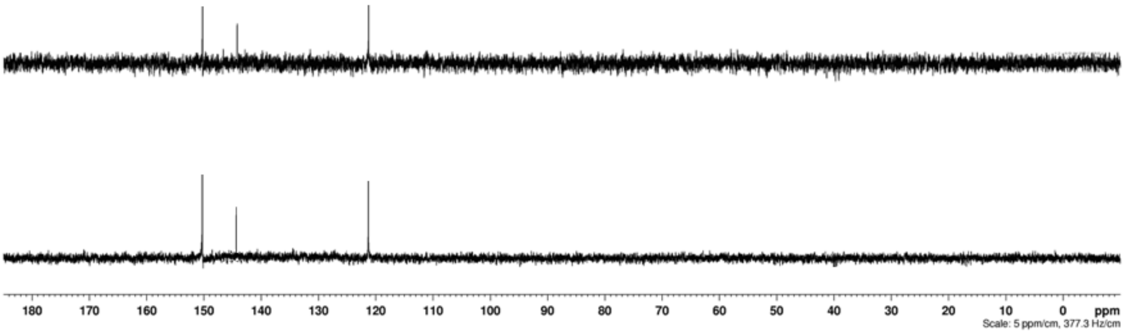

Figure S100. ^{13}C DEPT spectra for B_e isolated from a gel produced using method 3.

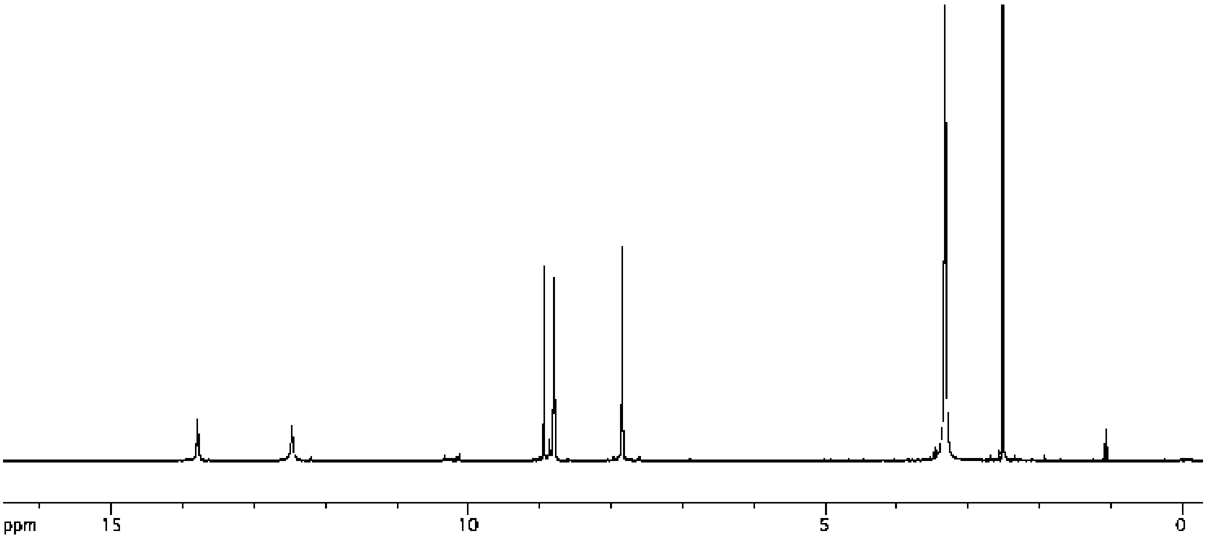

Figure S101. ^{1}H NMR spectra for $\mathbf{C_e}$ isolated from a gel formed using ex situ prepared $\mathbf{C_e}$.

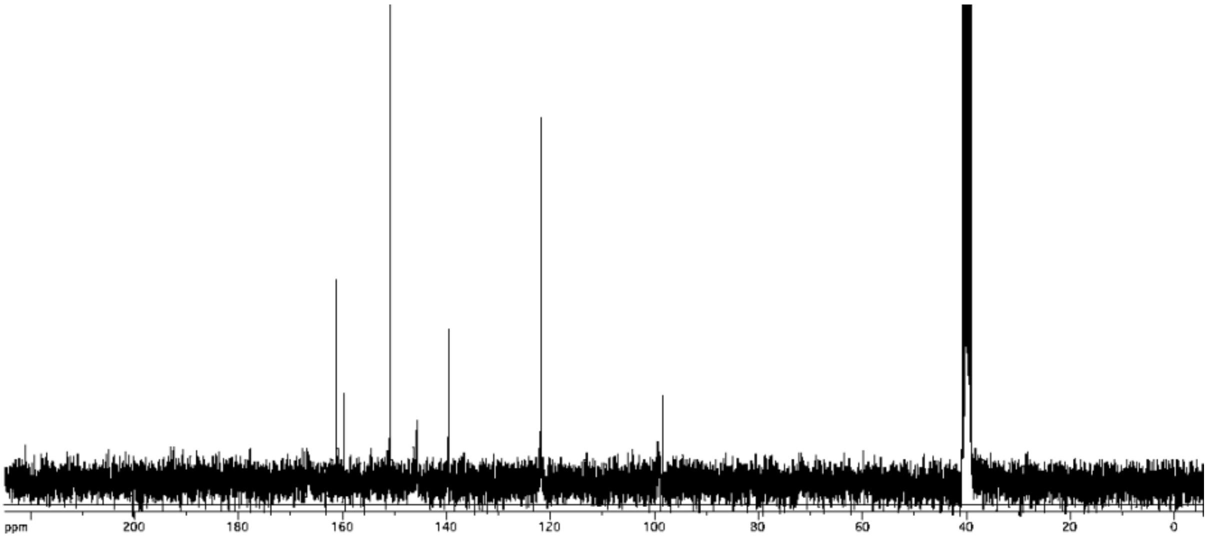

Figure S102. ^{13}C NMR spectra for $\mathbf{C_e}$ isolated from a gel formed using ex situ prepared $\mathbf{C_e}$.

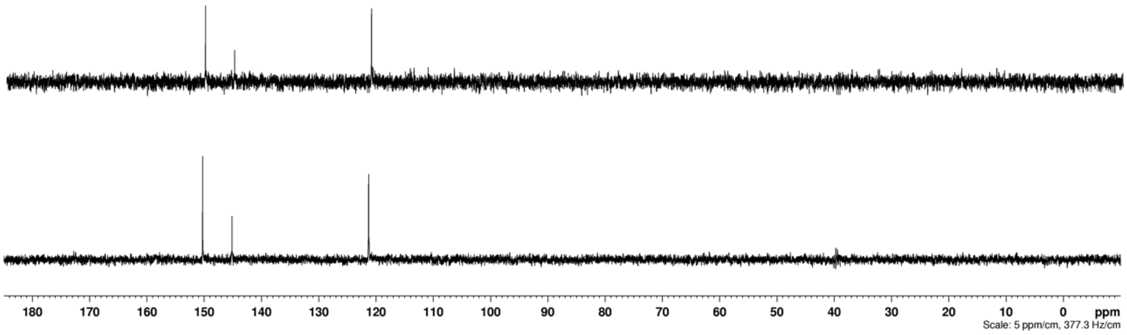

Figure S103. ^{13}C DEPT spectra for $\mathbf{C_e}$ isolated from a gel formed using ex situ prepared $\mathbf{C_e}$.

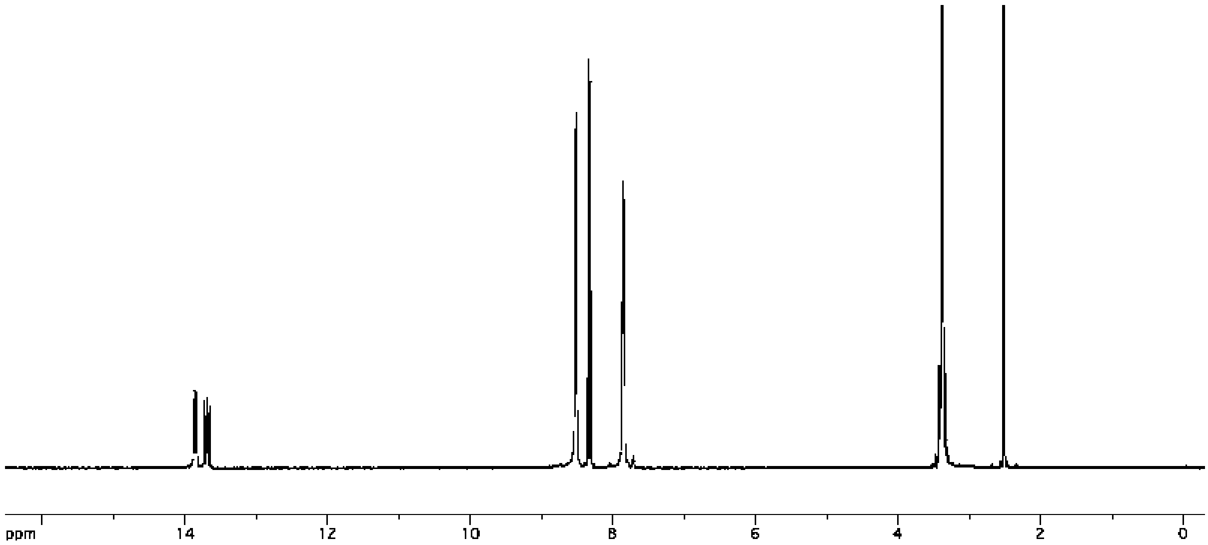

Figure S104. ^{1}H NMR spectra for $\mathbf{C_k}$ isolated from a gel formed using ex situ prepared $\mathbf{C_e}$.

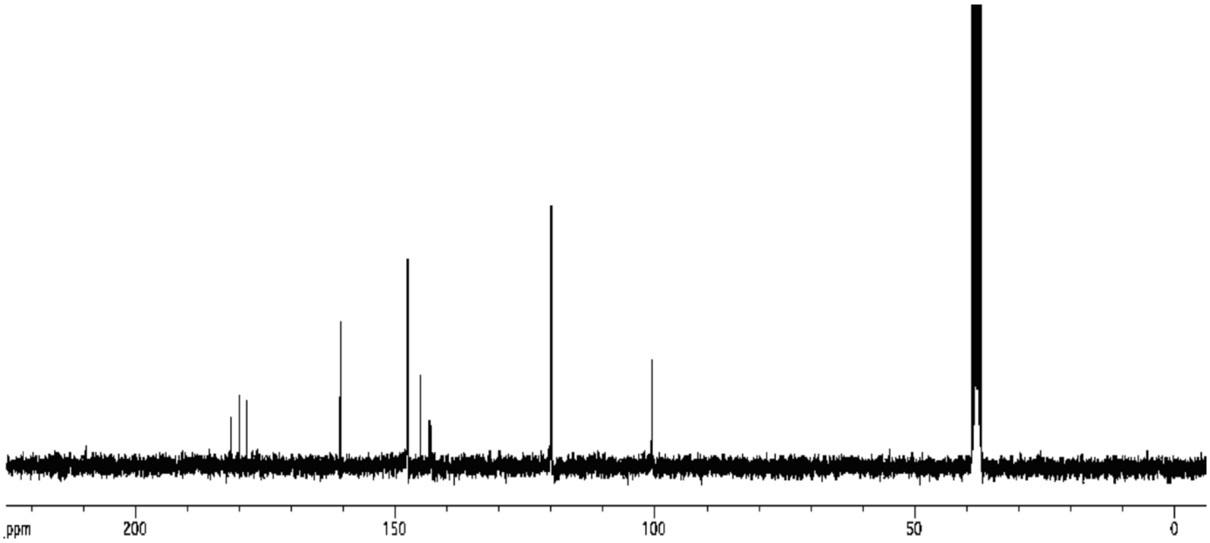

Figure S105. ^{13}C NMR spectra for $\mathbf{C_k}$ isolated from a gel formed using ex situ prepared $\mathbf{C_e}$.

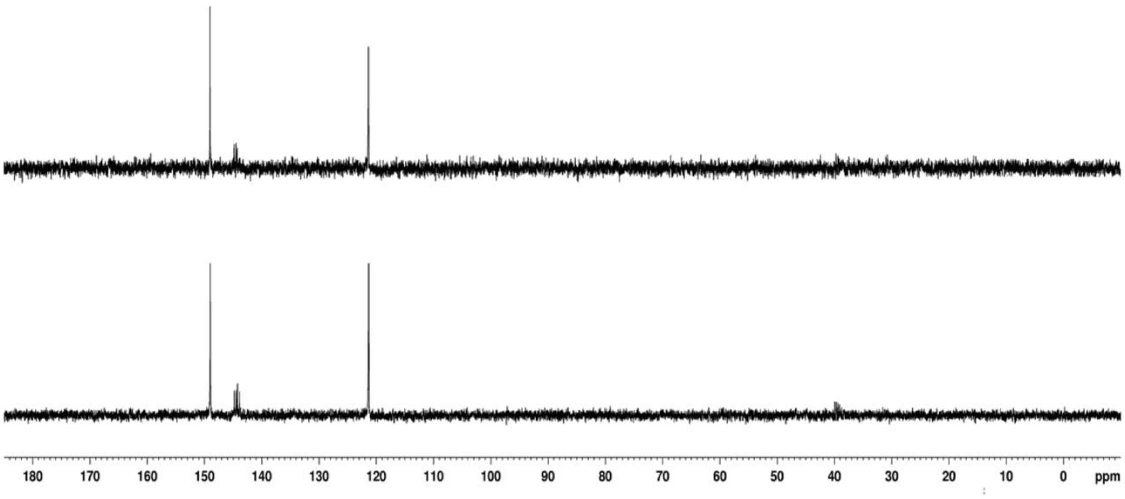

Figure S106. ^{13}C DEPT for $\mathbf{C_k}$ isolated from a gel formed using ex situ prepared $\mathbf{C_e}$.

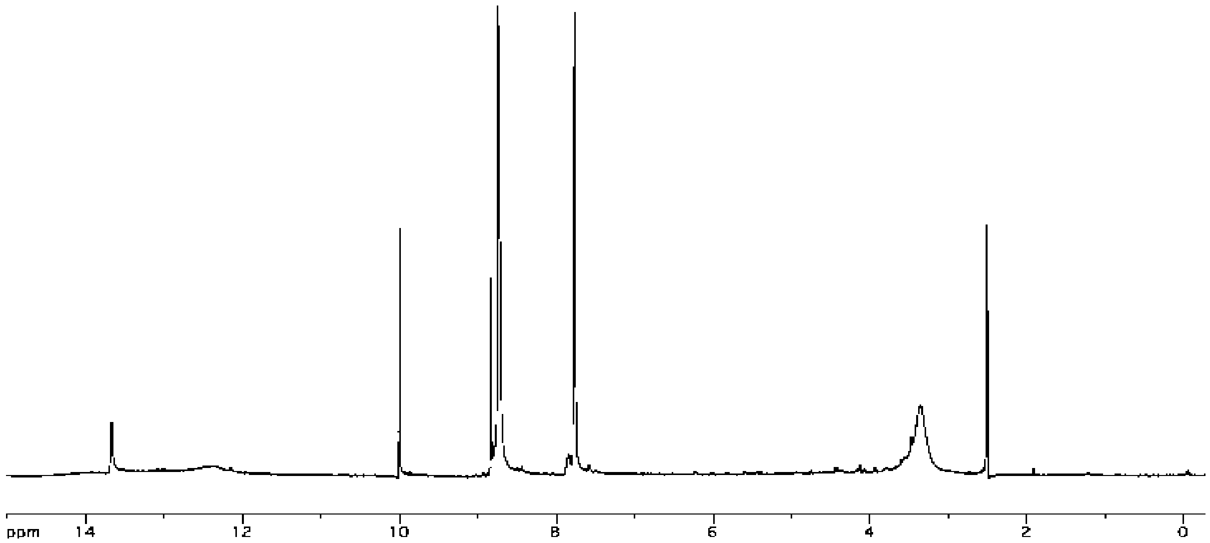

Figure S107. ^{1}H NMR spectra for $\mathbf{B_e}$ isolated from a gel produced using isolated ex situ $\mathbf{B_e}$.

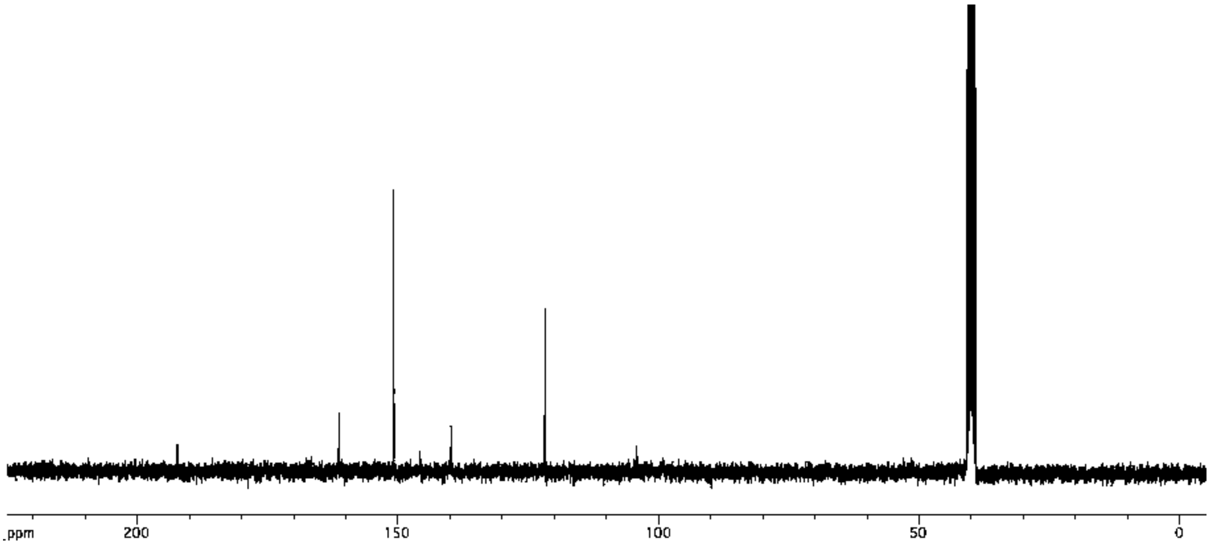

Figure S108. ^{13}C NMR spectra for $\mathbf{B_e}$ isolated from a gel produced using isolated ex situ $\mathbf{B_e}$.

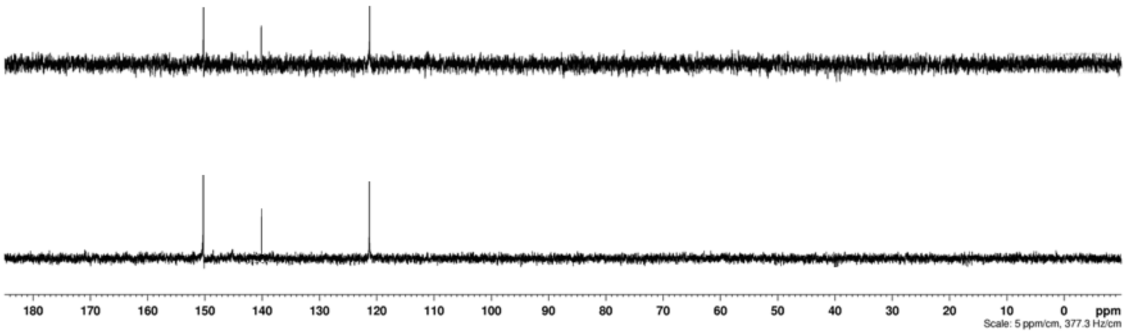

Figure S109. ^{13}C DEPT spectra for $\mathbf{B_e}$ isolated from a gel produced using isolated ex situ $\mathbf{B_e}$.

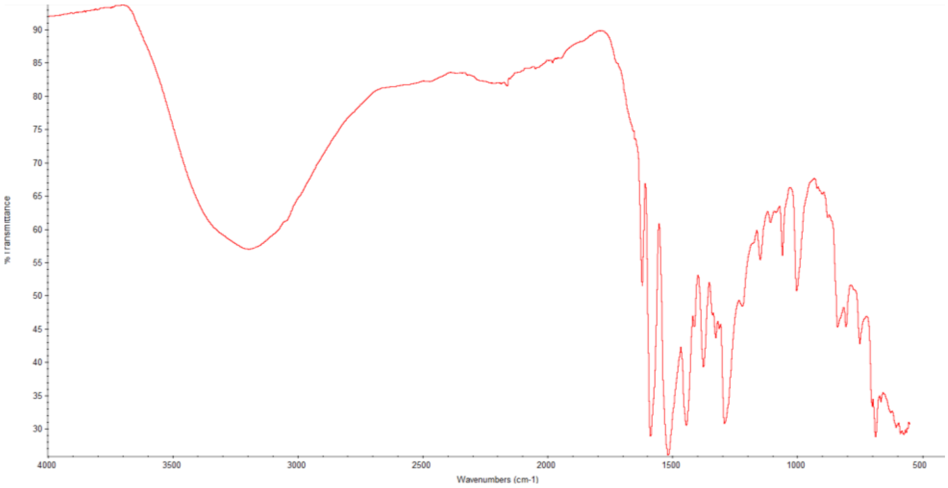

Figure S110. IR spectra for **C$_k$** prepared using ex situ produced **C$_e$**.

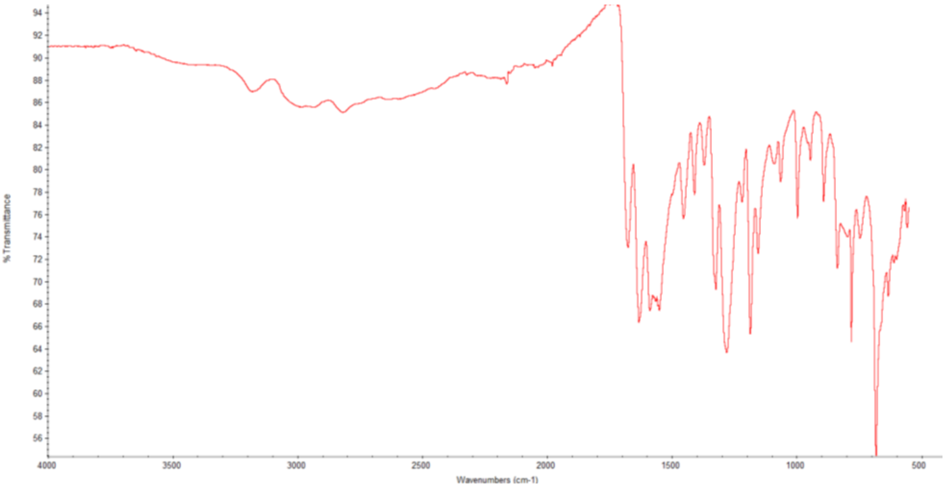

Figure S111. IR spectra for **C$_e$** prepared using ex situ produced **C$_e$**.

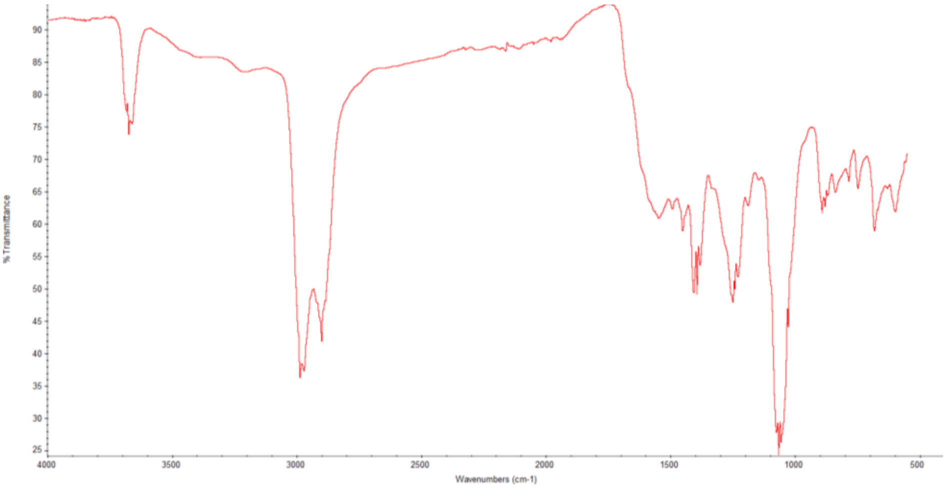

Figure S112. IR spectra for **B$_e$** prepared using ex situ isolated **B$_e$**.

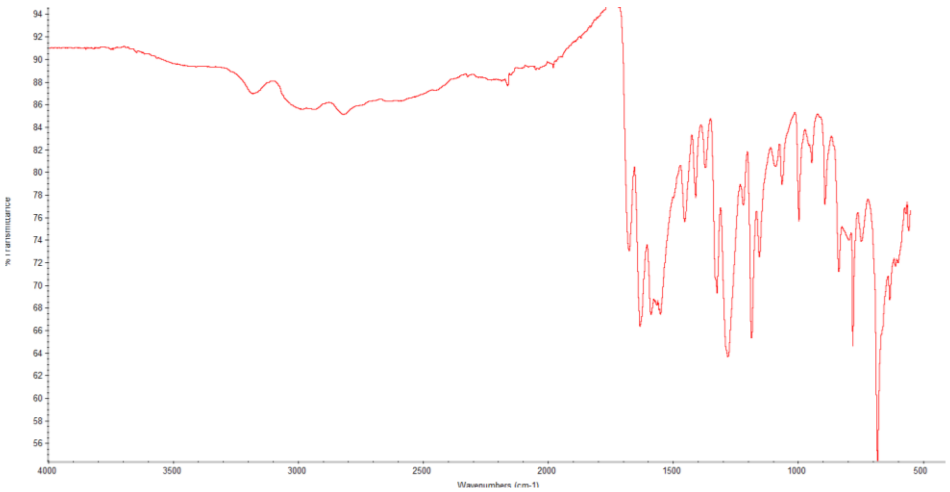

Figure S113. IR spectra Ce prepared using method 2.

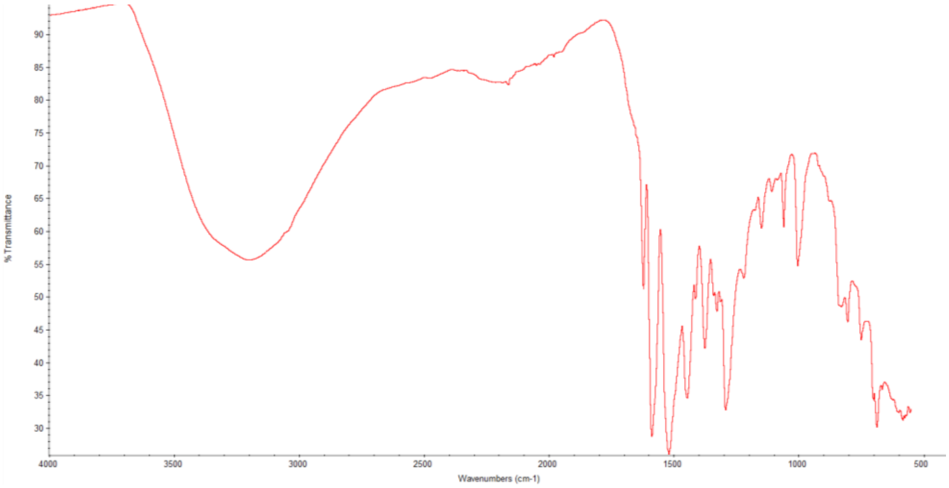

Figure S114. IR spectra **C**$_{k}$ prepared using method 1.

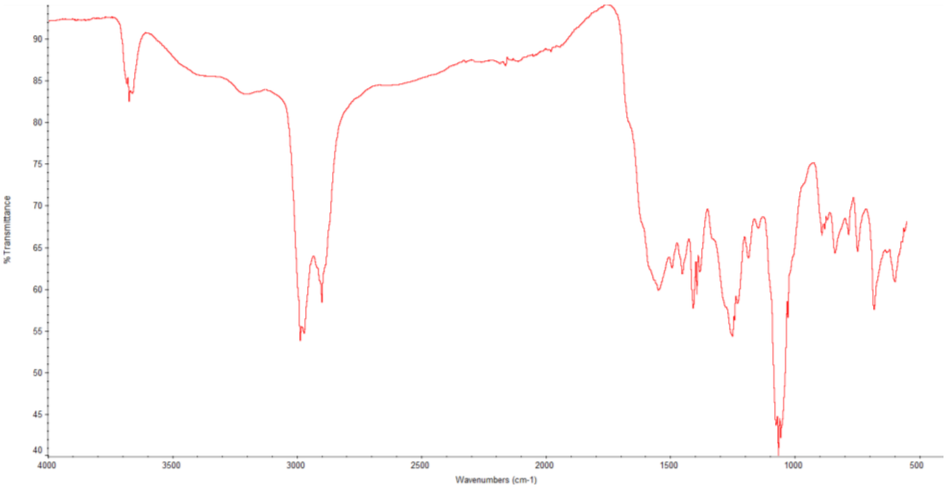

Figure S115. IR spectra **B**$_{e}$ prepared using method 3.